AWARD NUMBER: W81XWH-18-1-0082

TITLE: Design of a 3D Mammography System in the Age of Personalized Medicine

PRINCIPAL INVESTIGATOR: Raymond J. Acciavatti, Ph.D.

CONTRACTING ORGANIZATION: University of Pennsylvania
Philadelphia, PA 19104

REPORT DATE: April 2019

TYPE OF REPORT: Annual

PREPARED FOR: U.S. Army Medical Research and Materiel Command
Fort Detrick, Maryland 21702-5012

DISTRIBUTION STATEMENT: Approved for Public Release;
Distribution Unlimited

REPORT DOCUMENTATION PAGE

Form Approved
OMB No. 0704-0188

1. REPORT DATE
April 2019

2. REPORT TYPE
Annual

3. DATES COVERED
15 March 2018 – 14 March 2019

4. TITLE AND SUBTITLE

Design of a 3D Mammography System in the Age of Personalized Medicine

5a. CONTRACT NUMBER

5b. GRANT NUMBER
W81XWH-18-1-0082

5c. PROGRAM ELEMENT NUMBER

6. AUTHOR(S)

Raymond J. Acciavatti, Ph.D.

E-Mail: Raymond.Acciavatti@uphs.upenn.edu

5d. PROJECT NUMBER

5e. TASK NUMBER

5f. WORK UNIT NUMBER

7. PERFORMING ORGANIZATION NAME(S) AND ADDRESS(ES)

University of Pennsylvania
Philadelphia, PA 19104

8. PERFORMING ORGANIZATION REPORT NUMBER

9. SPONSORING / MONITORING AGENCY NAME(S) AND ADDRESS(ES)

U.S. Army Medical Research and Materiel Command
Fort Detrick, Maryland 21702-5012

10. SPONSOR/MONITOR'S ACRONYM(S)

11. SPONSOR/MONITOR'S REPORT NUMBER(S)

12. DISTRIBUTION / AVAILABILITY STATEMENT

Approved for Public Release; Distribution Unlimited

13. SUPPLEMENTARY NOTES

14. ABSTRACT

Many medical centers now offer 3D mammography for breast cancer screening. However, there continues to be a high recall rate after screening, so most women that are recalled are ultimately found to be cancer-free. Also, call-back studies such as magnification mammography continue to rely on conventional 2D techniques, and have not advanced in parallel with 3D screening mammography. We use virtual clinical trials (VCTs) with computational phantoms to evaluate new designs for screening and magnification mammography. To date, our VCTs with Defrise phantoms demonstrated the advantage of personalized scan motions, which are customized to each patient. These new designs offer improvements in the visualization of fibroglandular tissue, which can hide a tumor. Additionally, x-ray experiments were performed with high-resolution test patterns in magnification mammography. These experiments demonstrated the feasibility of introducing 3D imaging techniques into this study. Additionally, we made advancements to the underlying technology used in VCTs; e.g., the algorithm for inserting calcifications (lesions that can act as an early sign of cancer). Finally, we developed a detector model for use in VCTs; this model more accurately simulates how resolution changes over the detector area due to spatial variation in the incidence angle.

15. SUBJECT TERMS

Digital breast tomosynthesis (DBT), mammography, super-resolution, personalized medicine, Defrise phantom, image reconstruction, calcification, virtual clinical trial, magnification mammography.

16. SECURITY CLASSIFICATION OF:			17. LIMITATION OF ABSTRACT	18. NUMBER OF PAGES	19a. NAME OF RESPONSIBLE PERSON
a. REPORT	b. ABSTRACT	c. THIS PAGE			USAMRMC
Unclassified	Unclassified	Unclassified	Unclassified	93	19b. TELEPHONE NUMBER *(include area code)*

Standard Form 298 (Rev. 8-98)
Prescribed by ANSI Std. Z39.18

Table of Contents

1. INTRODUCTION

Many medical centers have adopted digital breast tomosynthesis (DBT) or "3D mammography" for breast cancer screening. Although the clinical implementation of DBT is relatively recent, this technology is based on a design that has been used in research applications for many years. DBT systems have not evolved nearly as rapidly as computed tomography (CT) scanners, which incorporate the latest trends in personalized medicine. In point-of-care CT, the motion of the x-ray tube is personalized around the clinical task and the unique anatomy of the individual.[1,2] This grant is focused on re-designing DBT systems around similar principles. We are exploring more complex motions for the x-ray tube and the detector as a strategy for improving the visualization of lesions (masses and calcifications), as well as dense, fibroglandular tissue. The new designs are customized to each patient based on a low-dose 2D scout image, which is used to gain an estimate of the breast size, shape, and internal composition prior to the 3D acquisition. The personalized designs are being tested with virtual clinical trials (VCTs) using computational breast phantoms.[3] VCTs allow new system designs to be developed in a rapid and cost-effective manner. Also, a wide range of different breast anatomies (size, shape, and internal compositions) can be simulated without requiring human subject recruitment.

2. KEYWORDS

Digital breast tomosynthesis (DBT), mammography, super-resolution, personalized medicine, Defrise phantom, image reconstruction, calcification, virtual clinical trial, magnification mammography.

3. ACCOMPLISHMENTS

3.A. What were the major goals of the project?

The Statement of Work is shown below, focusing on Year 1. Milestones achieved to date are summarized for each of the major tasks. More detail about these milestones is given in Section 3.B.

3.A.1. Specific Aim 1: Design a personalized image acquisition technique for screening mammography.

	Timeline (Months)
Major Task 1: Optimize super-resolution (SR) with simulations of high-frequency, sinusoidal test objects and calculations of the *r*-factor.	
Subtask 1: Develop a design for optimizing SR. Through our prototype system, we learned that SR can be optimized by introducing detector motion that varies the source-to-image distance (SID) during the scan. However, to minimize the need for a thick detector housing, we will investigate more complex combinations of x-ray tube and detector motion that can be used to optimize SR.	1-12
Milestone Achieved To Date: Mathematical model of SR (refer to document 1 of Section 9).	
Major Task 2: Simulate the reconstruction of glandular and adipose tissue with Defrise phantoms.	
Subtask 1: Prepare Defrise phantoms modeled in the shape of breasts.	1-3
Subtask 2: Simulate the image acquisition. First, a 2D scout image is acquired at low radiation dose. Second, the 3D scan parameters are determined based on estimates of the breast size, shape, and internal composition.	4-9
Subtask 3: Prepare reconstructions, and calculate the relative contrast at the septa between glandular and adipose tissue.	10-15
Milestone Achieve To Date: Database of Defrise phantoms and reconstructions, demonstrating that personalized scanning motions yield improvements in image quality (refer to document 2 of Section 9).	

Major Task 3: Develop a personalized acquisition geometry yielding a more accurate segmentation of the breast outline.	
Subtask 1: Prepare database of binary phantom masks (uniform phantoms with no internal composition). These will be used to calculate the breast outline (convex hull) in the reconstruction.	4-6
Subtask 2: Determine the motions of the x-ray tube and detector that yield the most accurate breast outline segmentation. These motions will be personalized to the breast size and shape based on a 2D scout image.	7-21
<u>Milestone Achieved to Date:</u> Database of 30 binary phantoms masks.	

3.A.2. Specific Aim 2: Design a 3D Magnification Mammography Call-Back Exam.

	Timeline (Months)
Major Task 4: Optimize super-resolution (SR).	
Subtask 1: Develop designs for the source and detector motion that optimize SR in magnification imaging. This will ensure the highest image quality in imaging calcifications (small, closely-spaced structures).	1-12
<u>Milestones Achieved to Date:</u> Mathematical model of SR (refer to document 1 of Section 9); Experimental data with high-resolution phantom using prototype next-generation tomosynthesis system (refer to document 3 of Section 9).	
Major Task 5: Perform a contrast-detail reader study.	
Subtask 1: Simulate a contrast-detail (C-D) array in a uniform background at different positions. The scan parameters for the 3D acquisition will be customized around the region containing the C-D array.	7-12
<u>Milestone Achieved to Date:</u> Development of calcification simulation and insertion method (refer to document 4 of Section 9).	

3.A.3. Specific Aim 3: Evaluate the new designs for screening and call-back imaging with a virtual clinical trial.

	Timeline (Months)
Major Task 6: Quantify breast density in anatomical phantoms.	
Subtask 1: Prepare anatomical phantoms with variable size, shape, and internal composition.	1-3
Subtask 2: Simulate x-ray images in personalized and non-personalized acquisition geometries.	4-6
Subtask 3: Calculate reconstructions. Model the differentiation between adipose and glandular tissue as a binary classification task with a receiver operating characteristic (ROC) curve.	7-12
<u>Milestone Achieved To Date:</u> Reconstructions demonstrating that ROC methods can be used to rank different acquisition geometries in terms of breast density visualization (document 2 of Section 9).	
Major Task 7: Perform a virtual clinical trial (VCT) with simulated lesions.	
Subtask 1: Prepare computational breast phantoms with lesions (masses and calcifications) of variable size, shape, and contrast.	1-6
Subtask 2: Design the VCT. Numerical observers will be trained on the statistics of images. Channelized Hotelling Observer parameters will be determined to match the performance of the observer on real and breast model images.	7-12
<u>Milestones Achieved To Date:</u> Simulations of breast phantoms and lesions (document 4 of Section 9); Publication of advanced detector model (documents 5 and 6 of Section 9).	

3.B. What was accomplished under these goals?

3.B.1. Specific Aim 1: Design a personalized image acquisition technique for screening mammography.

In our previous work, we demonstrated that clinical DBT systems support super-resolution (SR), or subpixel resolution relative to the detector. SR is a mechanism for improving the visibility of calcifications.[4] However, clinical DBT systems are not yet designed to maximize this effect. There are "blind spots" throughout the image at which SR is not achievable. We previously demonstrated that SR can be optimized by introducing detector motion along the source-to-image (SID) direction.[5] This design requires a thicker (bulkier) detector housing, which makes patient positioning more cumbersome. In our grant application, we proposed a different design strategy to optimize SR; specifically, by introducing x-ray tube motion in the SID direction. Since the source and detector move in combination, we expect less detector motion to be necessary to optimize SR, and hence the detector housing does not need to be as thick. In our grant application, we proposed to use the first year to advance our theoretical model, so that it includes a full three degrees of freedom in the motion of both the x-ray tube and detector. We have successfully developed this model and it is now capable of simulating arbitrary motions. The paper draft describing this model is included in Section 9 (document 1); we project that this draft will be submitted to a peer-reviewed journal.

In addition, we developed a "personalized" system design for DBT. As we projected in our proposal, we have shown that this design offers advantages in breast density visualization. We presented this research at the 2019 SPIE Medical Imaging Conference in San Diego, and the proceedings manuscript is included in Section 9 (document 2). In this work, four breast outlines with different sizes and shapes were simulated. The phantoms were given internal composition consisting of two tissue types (fibgroglandular and adipose) in an alternating ("Defrise") pattern. Each phantom was simulated in multiple acquisition geometries (441 in total) which varied in terms of the range of x-ray tube motion in two directions. To achieve the clearest separation between the two tissue types, we showed that the optimum acquisition geometry differs between phantoms, and therefore the motion of the x-ray tube needs to be personalized around the dimensions of the phantom. As discussed in our conference presentation, the dimensions of the phantom can be estimated using a low-dose 2D scout image prior to the 3D acquisition.

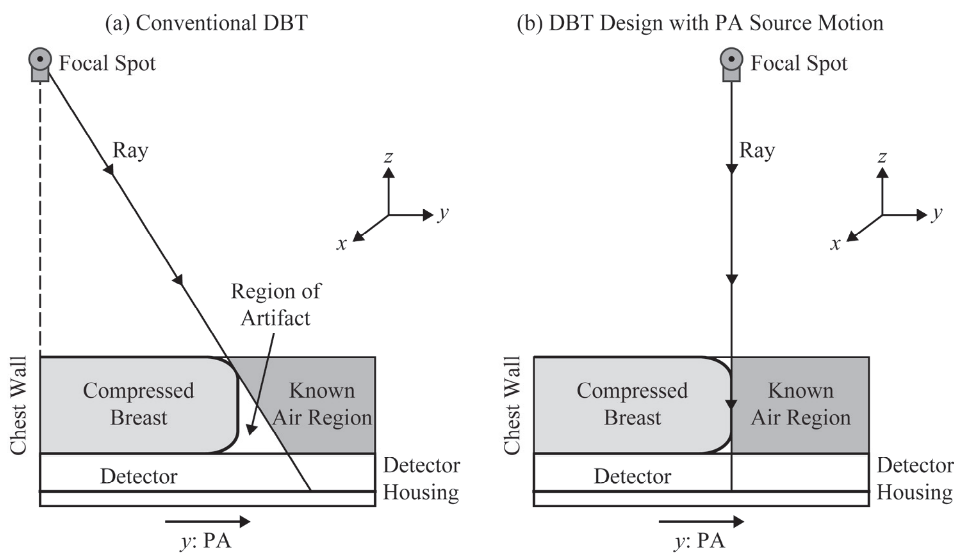

Figure 1. (a) In a conventional DBT system, the breast outline is overestimated due to geometric magnification. The overestimation artifact is pronounced in slices closest to the detector. (b) The new system design allows for an additional component of x-ray tube motion in the posteroanterior (PA) direction. This motion is not supported by clinical DBT systems. This design is analyzed as a strategy for improving the accuracy of the breast outline segmentation. This figure is adapted from the work of Acciavatti *et al*.[6]

In our grant application, we also indicated that we would analyze the task of segmenting the breast outline from the background. In clinical systems, the breast outline is overestimated in the posteroanterior (PA) direction. This concept can be understood from Figure 1. As we projected in our proposal, we have successfully developed a strategy for improving the accuracy of the breast outline segmentation through the use of x-ray tube motion in the PA direction. Figure 2 illustrates the breast outline segmentation for a phantom with 50 mm thickness and a chest wall-to-nipple distance of 97 mm. This slice in the reconstruction is 0.5 mm above the breast support. In the design with PA source motion (blue), the overestimation artifact is less pronounced than in the conventional design (red); hence, the breast outline is portrayed more accurately. In our grant application, we proposed the idea of creating a database of phantoms by the end of the first year, so that we could compute these overestimation artifacts in breasts with various sizes and shapes. We successfully created this database using the 3D breast model developed by Rodríguez-Ruiz *et al.*[7]. Our database currently includes 30 breast outlines with the dimensions summarized in Figure 3.

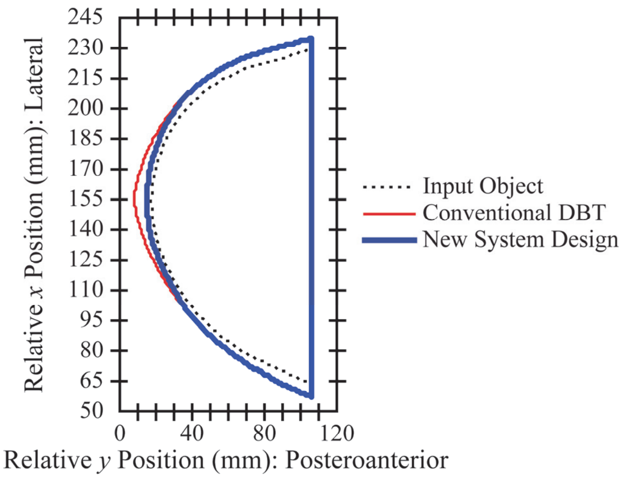

Figure 2. This slice in the reconstruction illustrates the overestimation artifact in the breast outline segmentation for a simulated phantom. As one would expect from Figure 1, the breast outline is overestimated in the PA direction. The artifact is less pronounced in our new design with PA source motion. This figure is adapted from the work of Acciavatti *et al.*[6]

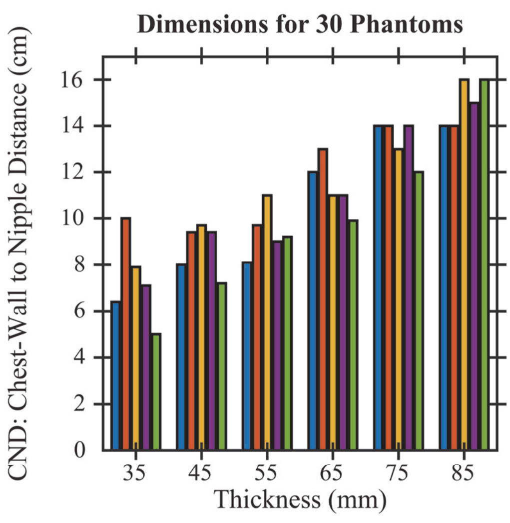

Figure 3. A database of 30 breast outlines was created using the model developed by Rodríguez-Ruiz *et al.*[7] Five random phantoms were created at a given thickness. The thicknesses ranged between 35 and 85 mm in 10 mm steps. To illustrate how the shapes of the phantoms differ at each thickness, the chest wall-to-nipple distance (CND) is shown.

3.B.2. Specific Aim 2: Design a 3D Magnification Mammography Call-Back Exam.

Patients with a suspicious finding in screening mammography are called-back for magnification mammography, a diagnostic study in which the breast is elevated closer to the x-ray tube. With this setup, small details appear bigger, making it easier for radiologists to characterize suspicious findings. While clinical magnification exams use 2D imaging techniques, we proposed the idea of 3D magnification mammography in our grant application. In our proposal, we indicated that we would develop a new system design that optimizes SR in 3D magnification mammography, as this would ensure the highest possible resolution in calcification imaging. To date, we have prepared a paper draft (document 3 in Section 9) describing experimental measurements of resolution in DBT. This paper draft includes 3D magnification mammography experiments. We plan to submit this draft to a journal. These experiments were done with our next-generation tomosynthesis (NGT) prototype system, which was built for research use in our lab.[8-12] Unlike a clinical DBT system, the NGT system is capable of 3D magnification imaging.

Our grant proposal also indicated that we would develop a theoretical model of SR for magnification imaging. In the model described in document 1 of Section 9, we allowed for the most general motions of the x-ray tube and detector. Consequently, in addition to being applicable to screening mammography, this model is also applicable to magnification mammography.

In our proposal, we indicated that we would perform "contrast-detail" experiments to evaluate calcification visibility in different system designs for magnification mammography. The purpose of these experiments is to analyze how the visibility of calcifications is dependent on their x-ray attenuation properties (contrast) and size (detail). To prepare for this study, our goal for the first year was to begin the simulation of calcifications. We met this goal by developing a more advanced calcification simulation method. This method is described in document 4 of Section 9. This document is an unpublished work that provides a description of our simulations.

3.B.3. Specific Aim 3: Evaluate the New Designs for Screening and Call-Back Imaging with a Virtual Clinical Trial

The purpose of this specific aim is to conduct VCTs to validate the new system designs for screening and magnification mammography. VCTs require a realistic simulation of the imaging system. In the first year of this grant, we published two papers in which we developed a more advanced detector model that can be used in VCTs (documents 5 and 6 in Section 9). Conventional detector models presume that the x rays are normally incident on the detector. Our model allows for an arbitrary incidence angle, and it quantifies the loss of spatial resolution due to obliquely-incident x rays. This model is important for evaluating new scanning motions, since the x rays may strike the detector at more oblique angles than in conventional system designs.

An additional goal for the first year of this grant was to demonstrate that receiver operating characteristic (ROC) methods can be used to rank different acquisition geometries in terms of breast density visualization. We successfully met this goal through the results that we published in our SPIE proceedings paper (document 2 in Section 9). In this paper, phantoms consisting of two tissue types (fibroglandular and adipose tissue) were simulated. The reconstruction was analyzed as a binary classification task with a threshold. By varying the threshold, we created ROC curves to quantify how well breast density is visualized. These results demonstrate that ROC curves can indeed be used to predict the best possible scanning motion for breast density visualization, as we projected in our proposal.

An additional goal for our first year was to create anthropomorphic phantoms with lesions, as these could be used to design VCT experiments being proposed in the latter years of this grant. We have met our goal of creating phantoms with lesions, and our progress is described in document 4 of Section 9.

3.C. What opportunities for training and professional development has the project provided?

- Throughout the first year of the grant, the PI (Raymond J. Acciavatti, Ph.D.) gained experience mentoring a student (Matthew Willardson) working toward a Master's Degree in the Bioengineering Department. This student worked on VCT software and lesion simulations.

- At the 2019 SPIE Medical Imaging Conference in San Diego, the PI obtained additional training through the class "SC1239: Virtual Clinical Trials: An In-depth Tutorial".

3.D. How were the results disseminated to communities of interest?

- Our work on VCTs received the "Live Demonstration" award at the 2019 SPIE Medical Imaging conference in San Diego, California. The demonstration was titled "OpenVCT – Open Source Simulation Platform for Designing and Performing Virtual Clinical Trials", and it was held on 2/19/2019.

3.E. What do you plan to do during the next reporting period to accomplish these goals?

3.E.1. Specific Aim 1: Design a personalized image acquisition technique for screening mammography.

First, our research over the next year will expand upon our work on SR. We are now capable of simulating arbitrary motions for the x-ray tube and detector. Over the next year, we will simulate many different acquisition geometries using our theoretical model. This will allow us to identify the most promising system design: one that optimizes SR but does not require a thick (bulky) detector housing.

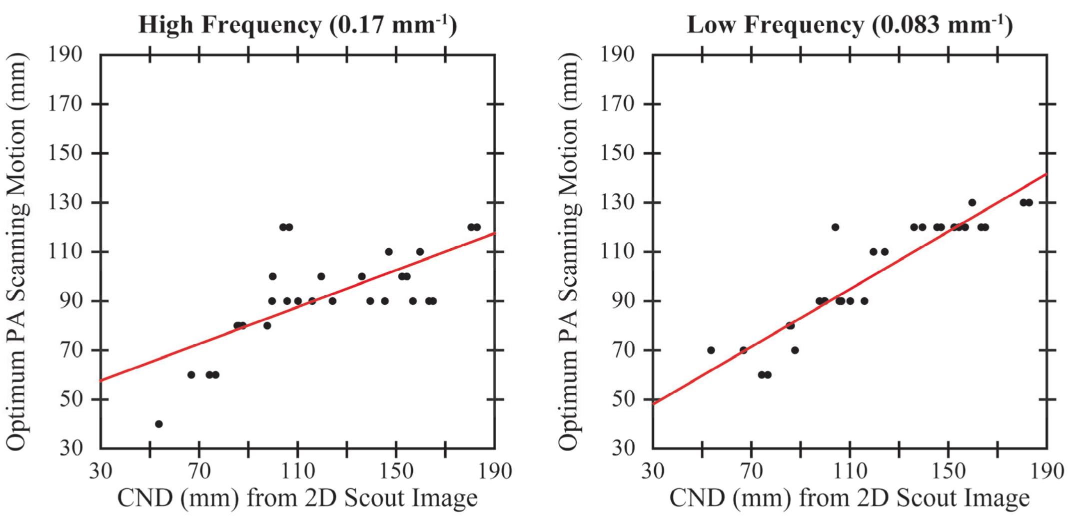

Figure 4. The best scanning motion for each phantom was calculated using the approach described in our SPIE proceedings manuscript (document 2 of Section 9). The fitted line shows how the optimum scanning motion can be determined based on the chest wall-to-nipple distance (CND) of the phantom. Hence, to optimize the appearance of fibroglandular tissue, the scanning motion needs to be customized around the dimensions of the object. These linear regression models are statistically significant ($p < 0.001$).

Second, our SPIE proceedings manuscript on personalized imaging will be expanded from four Defrise phantoms to 30 Defrise phantoms using the database of breast outlines that we described previously. We are striving to write a peer-reviewed paper describing these results. Our results-to-date are summarized in Figure 4. Two input frequencies (0.17 and 0.083 mm^{-1}) have been considered. Increasing the frequency corresponds to more complex parenchymal texture. In Figure 4, the best scanning motion is plotted as a function of the chest wall-to-nipple distance (CND); i.e., a measure of breast size that can be determined from a low-dose 2D scout image. As the CND increases, the x-ray tube needs to traverse a broader distance in the PA direction to optimize the reconstruction. The data were fit to a linear regression model, and the results are statistically significant ($p < 0.001$). These results demonstrate that the acquisition geometry is optimized by customizing the motion of the x-ray tube around the dimensions of the phantom.

Thirdly, the same group of 30 phantoms will be used in calculations of the breast outline segmentation. This work will be done in parallel with our research using Defrise phantoms. This will allow us to investigate whether the optimum scanning motion differs between the two tasks.

3.E.2. Specific Aim 2: Design a 3D Magnification Mammography Call-Back Exam.

For our future work, we will simulate many different scanning motions for the x-ray tube and detector, and use our theoretical model of SR to identify the most promising system design. We will investigate whether the design that optimizes SR differs between screening mammography (specific aim 1) and magnification mammography (specific aim 2).

Second, we will analyze reconstructions of "contrast-detail" calcification arrays to evaluate how well calcifications are portrayed in different system designs for magnification imaging. This work will also validate whether the use of SR in 3D magnification mammography offers an improvement over conventional 2D magnification mammography.

3.E.3. Specific Aim 3: Evaluate the New Designs for Screening and Call-Back Imaging with a Virtual Clinical Trial

Our development of new system designs is on-going in specific aim 1 (screening mammography) and specific aim 2 (magnification mammography). As we indicated in our grant proposal, VCTs will be conducted throughout the duration of the grant. VCTs will guide the design choices made in specific aims 1 and 2, and will ultimately be used to validate these designs in terms of lesion detection and characterization.

4. IMPACT

4.A. What was the impact on the development of the principal discipline(s) of the project?

Many medical centers now offer DBT for breast cancer screening exams. Although DBT offers advantages over 2D digital mammography, there continues to be a high recall rate after screening, so most women referred for additional testing are found to be cancer-free. Also, call-back imaging studies such as magnification mammography have not advanced in parallel with 3D screening mammography, and continue to rely on conventional 2D imaging techniques.

Our research has an impact on both screening and call-back imaging studies. First, in screening mammography, we developed a "personalized" system design that offers improvements in breast density visualization. Our design changes also allow for SR, or high-resolution imaging. Additionally, we demonstrated the experimental feasibility of achieving high resolution with 3D magnification mammography. Finally, our work has an impact on VCTs, as we developed a more advanced detector model that takes into account the resolution loss due to oblique x-ray incidence.

4.B. What was the impact on other disciplines?
Nothing to report.

4.C. What was the impact on technology transfer?
Nothing to report.

4.D. What was the impact on society beyond science and technology?
Nothing to report.

5. CHANGES / PROBLEMS

5.A. Changes in approach and reasons for change
Nothing to report.

5.B. Actual or anticipated problems or delays and actions or plans to resolve them
Nothing to report.

5.C. Changes that had a significant impact on expenditures
Nothing to report.

5.D. Significant changes in use or care of human subjects, vertebrate animals, biohazards, and/or select agents
Nothing to report.

5.E. Significant changes in use or care of human subjects
Nothing to report.

5.F. Significant changes in use or care of vertebrate animals
Nothing to report.

5.G. Significant changes in use of biohazards and/or select agents
Nothing to report.

6. PRODUCTS.

6.A. Publications, conference papers, and presentations

- **Journal publications**
    - Acciavatti RJ, Maidment ADA. Non-stationary model of oblique x-ray incidence in amorphous selenium detectors: I. Point spread function. Medical Physics. 2019; 46(2):494-504. This work has been published, and it includes an acknowledgement of funding support from DoD grant W81XWH-18-1-0082.
    - Acciavatti RJ, Maidment ADA. Nonstationary model of oblique x-ray incidence in amorphous selenium detectors: II. Transfer Functions. Medical Physics. 2019; 46(2); 505-16. This work has been published, and it includes an acknowledgement of funding support from DoD grant W81XWH-18-1-0082.

- **Books or other non-periodical, one-time publications**
    - Nothing to report.

- **Other publications, conference papers, and presentations**
    - Acciavatti RJ, Barufaldi B, Vent TL, Wileyto EP, Maidment ADA. Personalization of x-ray tube motion in digital breast tomosynthesis using virtual Defrise phantoms. In: Schmidt TG, Chen G-H, Bosmans H, editors; Physics of Medical Imaging; 2019; San Diego, CA: SPIE; 2019. p. 109480B-1 – 109480B-9. The PI (Raymond J. Acciavatti, Ph.D.) presented this work at the SPIE Medical Imaging conference on 2/17/19 in San Diego, CA. The proceedings manuscript and presentation both included an acknowledgement of funding support from DoD grant W81XWH-18-1-0082.

6.B. Website(s) or other Internet site(s)
The VCT software developed at the University of Pennsylvania can be accessed through the website https://sourceforge.net/projects/openvct/.

6.C. Technologies or techniques
Nothing to report.

6.D. Inventions, patent applications, and/or licenses
Nothing to report.

6.E. Other products
Nothing to report.

7. PARTICIPANTS AND OTHER COLLABORATING ORGANIZATIONS.

7.A. What individuals have worked on the project?

Name:	Raymond J. Acciavatti, Ph.D.
Project Role:	Principal Investigator (Research Associate)
Research Identifier:	ORCiD ID: 0000-0003-4822-3353
Nearest person month worked:	7
Contribution to project:	Lead investigator for all specific aims of the project. In the papers published to date, the PI is first author of two *Medical Physics* papers and one SPIE conference proceedings paper.
Funding Support:	

Name:	David Higginbotham
Project Role:	Software Developer
Research Identifier:	
Nearest person month worked:	2
Contribution to project:	VCT software development for x-ray projection simulation and breast phantom creation.
Funding Support:	

7.B. Has there been a change in the active other support of the PD/PI(s) or senior / key personnel since the last reporting period?
Nothing to report.

7.C. What other organizations were involved as partners?
Nothing to report.

8. SPECIAL REPORTING REQUIREMENTS.

8.A. Collaborative Awards
Nothing to report.

8.B. Quad Charts
Nothing to report.

REFERENCES

1. Xu J, Sisniega A, Zbijewski W, et al. Modeling and design of a cone-beam CT head scanner using task-based imaging performance optimization. *Physics in Medicine and Biology.* 2016;61:3180-3207.

2. Gang GJ, Stayman JW, Ehtiati T, Siewerdsen JH. Task-driven image acquisition and reconstruction in cone-beam CT. *Physics in Medicine and Biology.* 2015;60:3129-3150.

3. Barufaldi B, Higginbotham D, Bakic PR, Maidment ADA. OpenVCT: A GPU-Accelerated Virtual Clinical Trial Pipeline for Mammography and Digital Breast Tomosynthesis. Paper presented at: SPIE Medical Imaging2018; Houston, TX.

4. Acciavatti RJ, Maidment ADA. Observation of super-resolution in digital breast tomosynthesis. *Medical Physics.* 2012;39(12):7518-7539.

5. Acciavatti RJ, Wileyto EP, Maidment ADA. Modeling Acquisition Geometries with Improved Super-Resolution in Digital Breast Tomosynthesis. Paper presented at: SPIE Medical Imaging2016; San Diego, CA.

6. Acciavatti RJ, Rodriguez-Ruiz A, Vent TL, et al. Analysis of Volume Overestimation Artifacts in the Breast Outline Segmentation in Tomosynthesis. Paper presented at: SPIE Medical Imaging2018; Houston, TX.

7. Rodriguez-Ruiz A, Agasthya GA, Sechopoulos I. The compressed breast during mammography and breast tomosynthesis: in vivo shape characterization and modeling. *Physics in Medicine and Biology.* 2017;62:6920-6937.

8. Maidment AD, Acciavatti R, Vent T, et al. SSC14-03: Construction of a Prototype Digital Breast Tomosynthesis System with Superior Spatial Resolution. Paper presented at: RSNA2016; Chicago, IL.

9. Maidment TD, Vent TL, Ferris WS, Wurtele DE, Acciavatti RJ, Maidment ADA. Comparing the Imaging Performance of Computed Super Resolution and Magnification Tomosynthesis. Paper presented at: SPIE Medical Imaging2017; Orlando, FL.

10. Ferris WS, Vent TL, Maidment TD, Acciavatti RJ, Wurtele DE, Maidment ADA. Geometric Calibration for a Next-Generation Digital Breast Tomosynthesis System. Paper presented at: SPIE Medical Imaging2017; Orlando, FL.

11. Choi CJ, Vent TL, Acciavatti RJ, Maidment ADA. Geometric Calibration for a Next-Generation Digital Breast Tomosynthesis System Using Virtual Line Segments. Paper presented at: SPIE Medical Imaging2018; Houston, TX.

12. Eben JE, Vent TL, Choi CJ, et al. Development of a Next Generation Tomosynthesis System. Paper presented at: SPIE Medical Imaging2018; Houston, TX.

9. APPENDICES

1. Acciavatti RJ, Wileyto EP, Maidment ADA. Super-Resolution in Digital Breast Tomosynthesis: I. Anisotropies in the Conventional Design. This paper is being prepared for submission to a journal. The paper indicates that funding support was provided by the DoD (30 pages).

2. Acciavatti RJ, Barufaldi B, Vent TL, Wileyto EP, Maidment ADA. Personalization of x-ray tube motion in digital breast tomosynthesis using virtual Defrise phantoms. In: Schmidt TG, Chen G-H, Bosmans H, editors; Physics of Medical Imaging; 2019; San Diego, CA: SPIE; 2019. p. 109480B-1 – 109480B-9. The PI (Raymond Acciavatti) presented this work at the SPIE Medical Imaging conference on 2/17/19 in San Diego, CA. This work includes an acknowledgement of funding support from the DoD (9 pages).

3. Vent TL, Acciavatti RJ, Maidment ADA. Development and Evaluation of a Spatial Resolution Metric for Digital Breast Tomosynthesis. This paper is being prepared for submission to a journal. The paper indicates that funding support was provided by the DoD (9 pages).

4. This document is an unpublished work showing the details of progress made in lesion simulations in VCTs (7 pages).

5. Acciavatti RJ, Maidment ADA. Non-stationary model of oblique x-ray incidence in amorphous selenium detectors: I. Point spread function. Medical Physics. 2019; 46(2):494-504. This publication includes an acknowledgement of funding support from the DoD (11 pages).

6. Acciavatti RJ, Maidment ADA. Nonstationary model of oblique x-ray incidence in amorphous selenium detectors: II. Transfer Functions. Medical Physics. 2019; 46(2); 505-16. This publication includes an acknowledgement of funding support from the DoD (12 pages).

7. Award Chart summarizing progress made in Year 1 of the grant (1 page).

Super-Resolution in Digital Breast Tomosynthesis: I. Anisotropies in the Conventional Design

Raymond J. Acciavatti, E. Paul Wileyto, and Andrew D. A. Maidment

Department of Radiology
Perelman School of Medicine at the University of Pennsylvania
Philadelphia, Pennsylvania

Abbreviated Title: Super-Resolution in DBT: I. Anisotropies

Contact Information:
Raymond J. Acciavatti, Ph.D.
Perelman School of Medicine at the University of Pennsylvania
Department of Radiology
1 Silverstein Building
3400 Spruce Street
Philadelphia, PA 19104-4206, USA
Voice: 215-746-8759
Fax: 215-746-8764
Email: Raymond.Acciavatti@uphs.upenn.edu

ABSTRACT

Purpose: Our previous work investigated the potential for super-resolution (SR) in digital breast tomosynthesis (DBT). We demonstrated that SR is feasible in DBT, but that it is not uniformly achieved throughout the reconstruction. To expand upon that work, this paper develops a method for quantifying the proportion of the reconstruction volume in which SR is not achievable.

Methods: From first principles, the reconstruction of a sinusoidal test object was calculated. To investigate SR, the frequency was larger than the alias frequency of the detector. The Fourier transform of the reconstruction was also calculated; it includes a peak at a low frequency due to aliasing and a separate peak at the input frequency. The ratio of the amplitudes of these two respective peaks (termed r-factor) determines whether SR is achieved. To analyze how uniformly SR is achieved throughout a volume-of-interest (VOI), the r-factor was calculated at 1,000 randomly-sampled points. We calculated the proportion of points in the VOI for which SR is not achievable ($r \geq 1$), and determined a 95% confidence interval for this proportion with 200 bootstrapped simulations. To validate the presence of the anisotropies, a bar pattern phantom was imaged with a clinical DBT system. The phantom was tilted at an angle relative to the plane of the breast support, and the reconstruction plane was aligned with the oblique plane of the phantom. This setup allows for visualization of the anisotropies along the direction perpendicular to the breast support; *i.e.*, the z direction.

Results: A system was simulated with a source-to-image distance of 650.0 mm, 0.085 mm detector pixelation, 180.0 mm of source motion, and 15 projections. The test frequency (8.0 mm^{-1}) was oriented along the direction of source motion. The proportion of points for which the r-factor exceeds unity was calculated; the 95% confidence interval ranges between 7.2% and 10.9%. SR is not achievable in this proportion of the VOI. The z direction was then analyzed to illustrate the anisotropies. With theoretical modeling, the anisotropies were found to be spaced in regular increments along this direction. The anisotropies can be minimized by using a narrower range of source motion or by increasing the number of projections. Additionally, the theoretical model was validated experimentally with a bar pattern phantom. The anisotropies were observed at positions predicted by the model.

Conclusions: Although SR is achievable in DBT, there are anisotropies throughout the reconstruction. This paper develops a method for quantifying the proportion of the reconstruction volume in which there are anisotropies. We show that the anisotropies can be minimized by reducing the range of source motion or by increasing the number of projections; however, it is not possible to eliminate the anisotropies entirely in the conventional design for DBT systems.

Key words: Digital Breast Tomosynthesis, Super-Resolution, Image Reconstruction, Fourier Transform, Anisotropy.

1. INTRODUCTION

In digital breast tomosynthesis (DBT), a 3D image is created from various x-ray projections acquired over a small range of angles. Many medical centers have upgraded their breast cancer screening practices from 2D digital mammography (DM) to 3D/2D imaging in combination. Depending on the medical center, the 2D image can either be a DM image or a synthetic mammogram[1-8] that is created by processing the 3D image.

Although 3D imaging offers advantages[9-12], it has been shown that the benefits of 3D imaging are limited to non-calcification findings.[13] Our previous work investigated super-resolution (SR) as a mechanism for improving calcification visibility in DBT.[14, 15] SR is a term describing how the reconstruction can resolve high frequencies exceeding the alias frequency of the detector. A necessary condition for achieving SR is that the reconstruction is performed using a matrix with finer pixelation than the detector.

By simulating a high-frequency sinusoidal test object, our previous work showed that SR is feasible in DBT.[14, 16, 17] However, the existence of SR is dependent on the positioning of this object and on the orientation of the frequency.[14, 15, 18, 19] To expand upon that work, there needs to be an analysis of how much of the reconstruction volume consists of anisotropies; this is quantified in this paper as a proportion of the total volume. In addition, this paper uses a bar pattern phantom to illustrate the anisotropies in a clinical DBT system.

In computed tomography (CT), one strategy for improving the resolution is to increase the number of projections. This paper investigates whether a similar principle can be applied to DBT. For a CT scan with source rotation over a full 360° arc, the minimum number of projections (N_{min}) that is needed to resolve a given input frequency (ν_{M}) is

$$N_{\mathrm{min}} = \frac{4\pi R \nu_{\mathrm{M}}}{1 - \sin\left(\dfrac{\psi}{2}\right)}, \tag{1}$$

where ψ is the full fan angle and R is the radius over which the frequency ν_M can be resolved without aliasing.[20-22] To maximize the range of frequencies that can be visualized, N_{min} needs to be increased, and hence the spacing between source positions needs to be reduced. This idea can be extended to DBT by either reducing the range of source motion or by increasing the number of projections.

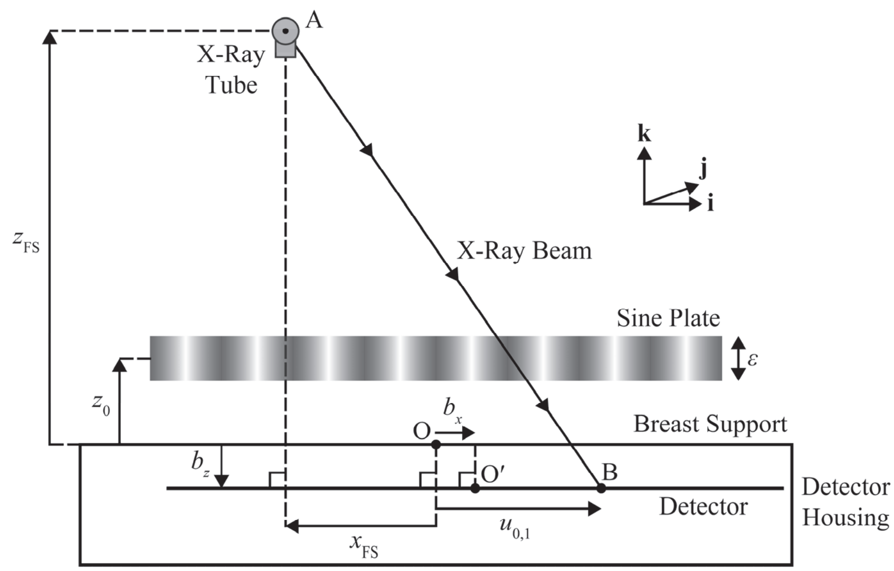

Figure 1. A cross section through the input object is shown in the plane of the chest wall. The origin (O) is the midpoint of the breast support. The primed origin (O′) is the corresponding midpoint of the detector. For the purpose of this figure, we assume that the source and point O′ are not displaced relative to this plane; the potential for source and detector motion in the y direction is considered in Figure 2.

2. METHODS

2.A. Test Object

The reconstruction of a sinusoidal test object is now calculated from first principles. This derivation is more general than the one presented in our previous work[14] in that we model the potential for arbitrary translations of the source and detector in all three directions during the scan. This paper focuses on the conventional acquisition geometry, which can be recovered as a special case. In Part 2, these equations are used to evaluate different acquisition geometries designed to optimize SR.

Figure 1 shows that the input object (a "*sine plate*") is a rectangular prism (thickness ε) whose attenuation coefficient varies sinusoidally

$$\mu_{\mathrm{obj}} = C_{\mathrm{obj}} \cdot \cos\left(2\pi f_0 \left[\left(x - x_0\right)\cos\alpha + (y - y_0)\sin\alpha \right]\right) \cdot \mathrm{rect}\left(\frac{z - z_0}{\varepsilon}\right), \tag{2}$$

where C_{obj} is the amplitude of the waveform and f_0 is the input frequency. As shown, the origin (O) is the coordinate corresponding to the midpoint of the chest wall side of the breast support. The mid-thickness of the object is positioned at the height z_0 relative to the origin. The coordinate $\left(x_0, y_0, z_0\right)$ denotes the centroid of the object at which $\mu_{\mathrm{obj}} = C_{\mathrm{obj}}$. Also, the rectangle function is defined by the equation

$$\mathrm{rect}(u) \equiv \begin{cases} 1, & |u| \leq 1/2 \\ 0, & |u| > 1/2 \end{cases}. \tag{3}$$

We model frequency along an arbitrary polar angle (α), as shown in Figure 2. This parameter is needed in Part 2 in which we analyze the effect of changing the orientation of the input frequency. For the purpose of this paper, only the 0° polar angle is considered; this corresponds to the left-right direction in a cranial-caudal view.

The position vector describing the most general coordinate of the focal spot (point A) relative to the origin (point O) is

$$\overrightarrow{\mathrm{OA}} = x_{\mathrm{FS}}\mathbf{i} + y_{\mathrm{FS}}\mathbf{j} + z_{\mathrm{FS}}\mathbf{k}, \tag{4}$$

where the subscript "FS" denotes "focal spot". In addition, the most general detector position can be modeled by the vector

$$\overrightarrow{\mathrm{OO'}} = b_x\mathbf{i} + b_y\mathbf{j} + b_z\mathbf{k}, \tag{5}$$

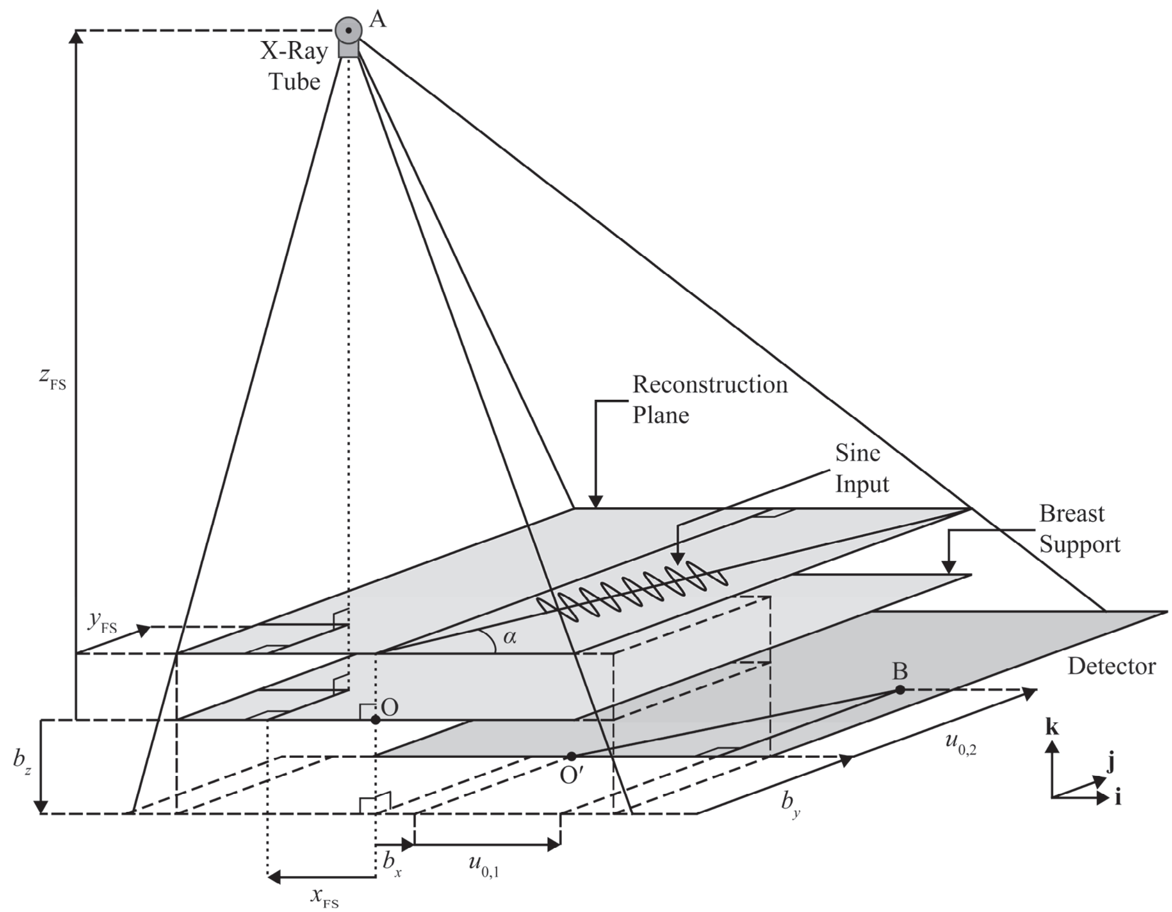

Figure 2. There are three degrees of freedom in the positioning of the focal spot (point A) and detector origin (point O′) relative to the origin (point O). The detector is assumed to be parallel with the breast support.

where O′ denotes the primed origin (the midpoint of the chest wall side of the detector). We assume that the detector is parallel with the breast support; the potential for detector rotation during the scan is not modeled in this paper.

Using Eqs. (4)-(5), a position vector can be calculated from the focal spot at A to an arbitrary detector coordinate $\left(u_{0,1}, u_{0,2}\right)$ at point B. Since

$$\overrightarrow{\mathrm{O'B}} = u_{0,1}\mathbf{i} + u_{0,2}\mathbf{j}\,, \tag{6}$$

it follows that

$$\overrightarrow{\mathrm{AB}} = \overrightarrow{\mathrm{AO}} + \overrightarrow{\mathrm{OO'}} + \overrightarrow{\mathrm{O'B}} \tag{7}$$

$$= -\overrightarrow{\mathrm{OA}} + \overrightarrow{\mathrm{OO'}} + \overrightarrow{\mathrm{O'B}} \tag{8}$$

$$= \xi_1 \mathbf{i} + \xi_2 \mathbf{j} + \xi_3 \mathbf{k}\,, \tag{9}$$

where

$$\xi_1 \equiv b_x + u_{0,1} - x_{\mathrm{FS}} \tag{10}$$

$$\xi_2 \equiv b_y + u_{0,2} - y_{\mathrm{FS}} \tag{11}$$

$$\xi_3 \equiv b_z - z_{\mathrm{FS}}\,. \tag{12}$$

These equations are used in Section 2.B. to determine the line integral of the ray through the object, and thus to calculate the signal for each projection image.

2.B. Calculation of X-Ray Signal

The line integral through the test object can be determined based on the equation of the ray from the focal spot at A to the detector at B.

$$\begin{pmatrix} x \\ y \\ z \end{pmatrix} = w \begin{pmatrix} \xi_1 \\ \xi_2 \\ \xi_3 \end{pmatrix} + \begin{pmatrix} x_{\mathrm{FS}} \\ y_{\mathrm{FS}} \\ z_{\mathrm{FS}} \end{pmatrix} \tag{13}$$

In Eq. (13), w is a free parameter ranging from zero at point A to unity at point B. The values of z at the entrance (“entr”) and exit surfaces of the test object are $z_0 + \varepsilon / 2$ and $z_0 - \varepsilon / 2$, respectively. The values of w at these two surfaces are

$$w_{\mathrm{entr}} = \frac{z_0 + \varepsilon / 2 - z_{\mathrm{FS}}}{\xi_3} \tag{14}$$

$$w_{\mathrm{exit}} = \frac{z_0 - \varepsilon / 2 - z_{\mathrm{FS}}}{\xi_3}\,. \tag{15}$$

The line integral of this ray along the path length ($\mathcal{L}$) through the object is thus

$$\mathcal{A}\mu_{\mathrm{obj}} = \int_{\mathcal{L}} \mu_{\mathrm{obj}} \cdot ds\,, \tag{16}$$

where the differential length (ds) along the ray is given by the expression

$$ds = \sqrt{\left(\frac{dx}{dw}\right)^2 + \left(\frac{dy}{dw}\right)^2 + \left(\frac{dz}{dw}\right)^2}\,dw \tag{17}$$

$$= \sqrt{\xi_1^2 + \xi_2^2 + \xi_3^2}\,dw\,. \tag{18}$$

Substituting Eqs. (2), (13), and (18) into Eq. (16) yields

$$\mathcal{A}\mu_{\mathrm{obj}} = \kappa_1 \cdot \int_{w_{\mathrm{entr}}}^{w_{\mathrm{exit}}} \cos\left[2\pi f_0\left(\xi_1 \cos\alpha + \xi_2 \sin\alpha\right) w + \kappa_2\right] dw \tag{19}$$

$$= \frac{\kappa_1 \cdot \left(\sin\left[2\pi f_0\left(\xi_1 \cos\alpha + \xi_2 \sin\alpha\right) w_{\mathrm{exit}} + \kappa_2\right] - \sin\left[2\pi f_0\left(\xi_1 \cos\alpha + \xi_2 \sin\alpha\right) w_{\mathrm{entr}} + \kappa_2\right]\right)}{2\pi f_0\left(\xi_1 \cos\alpha + \xi_2 \sin\alpha\right)}, \tag{20}$$

where

$$\kappa_1 = C_{\mathrm{obj}} \cdot \sqrt{\xi_1^2 + \xi_2^2 + \xi_3^2} \tag{21}$$

$$\kappa_2 = 2\pi f_0\left[\left(x_{\mathrm{FS}} - x_0\right)\cos\alpha + \left(y_{\mathrm{FS}} - y_0\right)\sin\alpha\right]. \tag{22}$$

By using a sum-to-product trigonometric identity described in our previous work[14], it can be shown that Eq. (20) can be simplified further.

$$\mathcal{A}\mu_{\mathrm{obj}} = \frac{-\varepsilon\kappa_1}{\xi_3} \cdot \cos\left[\frac{2\pi f_0}{\xi_3}\left(\xi_1 \cos\alpha + \xi_2 \sin\alpha\right)\left(z_0 - z_{\mathrm{FS}}\right) + \kappa_2\right] \cdot \operatorname{sinc}\left[\frac{\varepsilon f_0}{\xi_3}\left(\xi_1 \cos\alpha + \xi_2 \sin\alpha\right)\right] \tag{23}$$

To calculate the digitized signal, this expression can be integrated over the area of a detector element (del)

$$\mathcal{D}\mu_{\mathrm{obj}}(m_x, m_y) = \int_{(m_y-1)a_y}^{m_y a_y} \int_{(m_x-1793)a_x}^{(m_x-1792)a_x} \mathcal{A}\mu_{\mathrm{obj}} \frac{du_{0,1}}{a_x} \frac{du_{0,2}}{a_y} \tag{24}$$

$$\approx \frac{1}{J_{\mathrm{del},2}} \sum_{j_{\mathrm{del},2}=1}^{J_{\mathrm{del},2}} \left[\frac{1}{J_{\mathrm{del},1}} \sum_{j_{\mathrm{del},1}=1}^{J_{\mathrm{del},1}} \mathcal{A}\mu_{\mathrm{obj}}\Big|_{u_{0,1}=a_x\left(\frac{j_{\mathrm{del},1}-1/2}{J_{\mathrm{del},1}}+m_x-1793\right)} \right]_{u_{0,2}=a_y\left(\frac{j_{\mathrm{del},2}-1/2}{J_{\mathrm{del},2}}+m_y-1\right)}, \tag{25}$$

where a_x and a_y are the del dimensions, and m_x and m_y are integer indices used to number the dels. In a system with square dels, the subscripts can be removed ($a_x = a_y = a$). In Eq. (25), the del indices are numbered in such a way as to model the AXS-2430 detector (Analogic Canada Corporation, Montreal, Quebec), which is described in more detail in Section 3.B. The index m_x ranges between 1 and 3584. The index m_y ranges between 1 and 2816. Eq. (25) illustrates how a middle sum can be used to evaluate the integral; the number of samples in each direction is given by $J_{\text{del},1}$ and $J_{\text{del},2}$.

2.C. Reconstruction

The reconstruction is now calculated using simple backprojection (SBP). To determine the SBP reconstruction at the point (x, y, z), it is first necessary to identify the del that is intercepted by the ray between the points $(x_{\text{FS}}, y_{\text{FS}}, z_{\text{FS}})$ and (x, y, z). This ray strikes the detector position with coordinates

$$u_{\text{SBP},1} = \frac{x(z_{\text{FS}} - b_z) + z(b_x - x_{\text{FS}}) + b_z x_{\text{FS}} - b_x z_{\text{FS}}}{z_{\text{FS}} - z} \tag{26}$$

$$u_{\text{SBP},2} = \frac{y(z_{\text{FS}} - b_z) + z(b_y - y_{\text{FS}}) + b_z y_{\text{FS}} - b_y z_{\text{FS}}}{z_{\text{FS}} - z}. \tag{27}$$

Eqs. (26)-(27) can be derived by using a computer algebra system (Maple 15, Maplesoft, Waterloo, Ontario) to solve Eqs. (10)-(13) for $u_{0,1}$ and $u_{0,2}$. This detector position corresponds to the del with indices

$$m_{\text{SBP},x} = \left\lfloor \frac{u_{\text{SBP},1}}{a_x} \right\rfloor + 1793 \tag{28}$$

$$m_{\text{SBP},y} = \left\lfloor \frac{u_{\text{SBP},2}}{a_y} \right\rfloor + 1, \tag{29}$$

where $\lfloor \; \rfloor$ denotes the floor function, which is defined as follows.

$$\lfloor \nu_1 \rfloor \equiv \max\left\{\nu_2 \in \mathbb{Z} : \nu_2 \leq \nu_1\right\} \tag{30}$$

Averaging the backprojected signal for all N projections at the point (x, y, z) yields the SBP reconstruction.

$$\mu_{\mathrm{SBP}} = \frac{1}{N}\sum_n \mathcal{D}\mu_{\mathrm{obj}}\left(m_{\mathrm{SBP},x}, m_{\mathrm{SBP},y}\right) \tag{31}$$

This formula assumes that the reconstruction is prepared on an infinitesimally fine (*i.e.*, non-pixelated) grid. Signal can be measured along the polar angle α (the direction of the input frequency) using a coordinate transformation.

$$\begin{pmatrix} x \\ y \\ z \end{pmatrix} = \begin{pmatrix} x_0 \\ y_0 \\ z_0 \end{pmatrix} + \begin{pmatrix} \cos\alpha & -\sin\alpha & 0 \\ \sin\alpha & \cos\alpha & 0 \\ 0 & 0 & 1 \end{pmatrix}\begin{pmatrix} x'' \\ y'' \\ z'' \end{pmatrix} \tag{32}$$

In Section 3, Eq. (32) is used to measure signal along the x'' direction.

2.D. Fourier Space

To determine whether the test object is resolved in the reconstruction, the one-dimensional (1D) Fourier transform[23] of μ_{SBP} is now calculated. Although the Fourier transform is defined with infinite integration limits, we restrict the limits to a finite interval for the purpose of this calculation. This allows us to analyze how SR varies locally, and thus to demonstrate spatial anisotropies in SR. A middle sum is used to evaluate this integral

$$\mathcal{F}_1\mu_{\mathrm{SBP}} \approx \int_{x''_{\min}}^{x''_{\max}} \mu_{\mathrm{SBP}} e^{-2\pi i f_x'' x''} dx'' \tag{33}$$

$$\approx \left(\frac{x''_{\max} - x''_{\min}}{J_{\mathrm{FT}}}\right) \sum_{j_{\mathrm{FT}}=1}^{J_{\mathrm{FT}}} \mu_{\mathrm{SBP}} e^{-2\pi i f_x'' x''} \Big|_{x''=x''_{\min}+(x''_{\max}-x''_{\min})\left(\frac{j_{\mathrm{FT}}-1/2}{J_{\mathrm{FT}}}\right)}, \tag{34}$$

where $x''_{\min}$ and $x''_{\max}$ are the integration limits and J_{FT} is the number of samples. Assuming that the frequency is measured along the x'' direction, the Fourier transform should peak at the frequencies $f_x'' = \pm f_0$ and should be zero elsewhere. The existence of a major peak at another frequency indicates that the input object is not properly resolved.

Table 1. The simulation parameters for the test object and acquisition geometry are summarized below.

Parameter	Value
Polar angle (α)	0°
Thickness (ε)	0.50 mm
Del size (a)	0.085 mm
Detector O′ (b_x, b_y, b_z)	$(0, 0, -25.0)$ in mm
Frequency (f_0)	8.0 mm^{-1}
Del sampling [Eq. (25)]: $J_{\text{del},1}$	5
Del sampling [Eq. (25)]: $J_{\text{del},2}$	5
Fourier sampling [Eq. (34)]: J_{FT}	1,000
Number of projections (N)	15
Range of source motion (Q_x)	180.0 mm
Fourier interval [Eq. (34)]: $x''_{\min}$	–3.125 mm
Fourier interval [Eq. (34)]: $x''_{\max}$	3.125 mm
PA Motion of source (y_{FS})	0 mm
Source-to-support distance (z_{FS})	625.0 mm

3. RESULTS

3.A. Acquisition Geometry

We simulate the "next-generation tomosynthesis" (NGT) system, which was built for research use at the University of Pennsylvania.[24-28] Table 1 shows the acquisition parameters for this simulation. Although the NGT system is capable of source motion in both the x and y directions, we focus only on the conventional acquisition geometry for the purpose of this paper. Hence, we only model source motion along the x direction

$$x_{\mathrm{FS}} = \frac{(2n-N-1)Q_x}{2(N-1)}, \tag{35}$$

where Q_x is the range of source motion in the x direction and n is the projection number (*i.e.*, $1 \le n \le N$). The detector is stationary during the scan.

In the NGT system, the z-coordinate of the source is constant in all possible scan trajectories. This differs from a clinical system in which the source rotates in the plane of the chest wall, yielding motion in both the x and z directions.

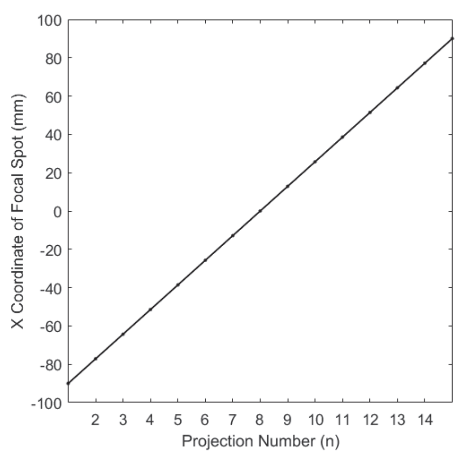

Figure 3. In this simulation, the x-coordinate of the source varies between –90.0 and 90.0 mm during the scan.

3.B. Sinusoidal Test Object

The NGT system was built with the AXS-2430 detector. The active area of this detector is 304.64 mm × 239.36 mm. The del size (a) is 0.085 mm; hence, the alias frequency is 5.88 mm^{-1} (*i.e.*, $0.5a^{-1}$). For analysis of SR, a test frequency of 8.0 mm^{-1} is chosen, since this frequency is higher than the alias frequency of the detector.

As shown in Table 1, the thickness of the test object is less than 1.0 mm. This is chosen to simulate the typical diameter of a calcification in DBT. Similar to previous work[14], we assume that $C_{\text{obj}} = \varepsilon^{-1} = 2.0\ \text{mm}^{-1}$, so that the line integral through μ_{obj} is normalized at normal incidence. The centroid of the object is positioned with x_0 and y_0 coordinates of 0 and 40.0 mm, respectively.

Figure 4 shows the effect of changing the z_0 coordinate of the object. The reconstructions are prepared assuming that $y'' = z'' = 0$ [Eq. (32)]; hence, the central position in these plots is matched to the coordinate (x_0, y_0, z_0). The plots are created using MATLAB® R2016a (MathWorks®, Natick, MA). At the depth $z_0 = 10.0$ mm [Figure 4(a)], the sine wave is clearly resolved. However, at the depth $z_0 = 11.5$ mm [Figure 4(b)], the signal is step-like in appearance. The width of each step matches the del size (0.085 mm). The appearance of Figure 4(b) is similar to a single projection image, which was calculated in our previous work.[14]

The 1D Fourier transforms of these reconstructions are calculated in Figure 4(c)-(d) using Eq. (34). We simulate 50 cycles of this frequency and 20 points per cycle; hence, $J_{\text{FT}} = 1{,}000$ (Table 1). To achieve SR, the frequency of the major peak must match the input frequency (8.0 mm^{-1}). This result is seen at the depth $z_0 = 10.0$ mm [Figure 4(c)] but not at the depth $z_0 = 11.5$ mm [Figure 4(d)].

Using the Fourier transform, our previous work proposed the r-factor as a metric to quantify SR.[14] The r-factor is the ratio of the amplitude of the highest peak less than the alias frequency

($5.88\ mm^{-1}$) to the amplitude at the input frequency. These amplitudes are illustrated in Figure 4(d) with the labels A_1 and A_2.

$$r = \frac{A_1}{A_2} \tag{36}$$

SR is achieved provided that $r < 1$, but aliasing is present provided that $r \geq 1$. At the depth z_0 = 10.0 mm [Figure 4(c)], A_1 is 0.0146 mm and A_2 is 0.517 mm, yielding r = 0.0283 and hence SR. By contrast, at the depth z_0 = 11.5 mm [Figure 6(d)], A_1 is 0.929 mm and A_2 is 0.530 mm, yielding r = 1.75 and hence aliasing.

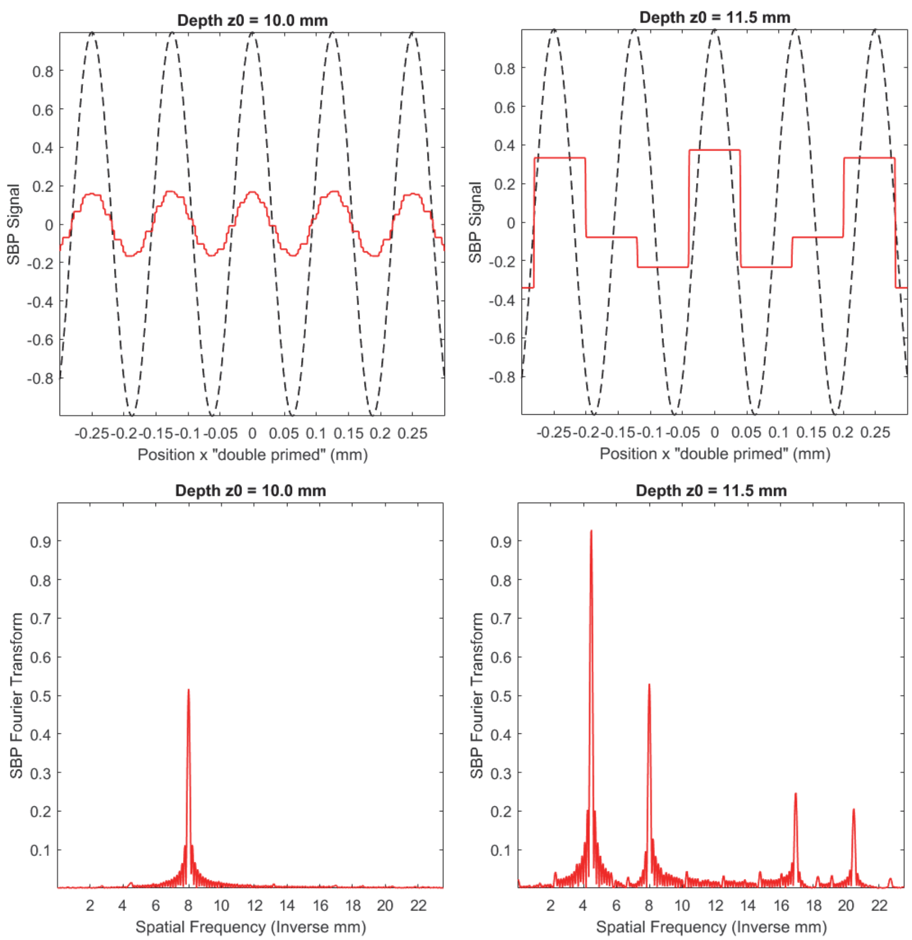

Figure 4. (a) SR is achieved at the depth z_0 = 10.0 mm. (b) The same test pattern is aliased at the depth z_0 = 11.5 mm. (c) The Fourier transform at the depth z_0 = 10.0 mm has a major peak at the input frequency ($8.0\ mm^{-1}$), indicating that the object is resolved. (d) The Fourier transform at the depth z_0 = 11.5 mm has a major peak at a lower frequency ($4.48\ mm^{-1}$). This result illustrates how the feasibility of SR is dependent on depth (z_0).

3.C. Quantification of the Anisotropies

The results presented in Section 3.B. suggest that there is variation in the quality of SR throughout the 3D image. One way to quantify this variation is to determine the *r*-factor at every point in a volume-of-interest (VOI), and calculate a histogram. This approach would require a long computation time due to the large number of points in the VOI. An alternate approach that is considered in Figure 5(a) is to calculate the histogram by randomly sampling points.

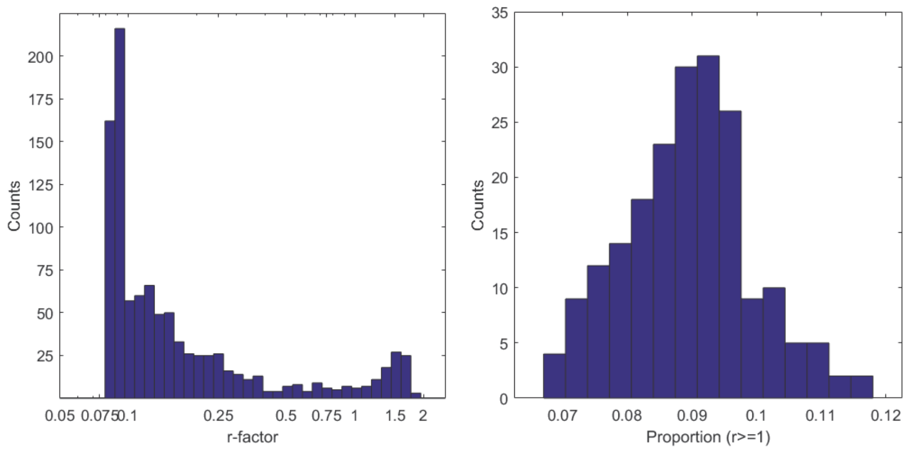

Figure 5. (a) The *r*-factor was calculated at 1,000 random points in a VOI, and the results are plotted as a histogram. SR is not achievable at the points for which $r \geq 1$; *i.e.*, 9.6% of the VOI. (b) In 200 bootstrapped simulations, we calculated the proportion of points for which $r \geq 1$. The middle 95% of this histogram varies between 7.2% and 10.9%.

For the purpose of Figure 5(a), the VOI is a rectangular prism with dimensions $200.0 \times 100.0 \times 50.0$ (in mm) and 0.020 mm spacing between points in each direction. The VOI is centered on the point $(0, 50.0, 25.0)$ (in mm). Figure 5(a) shows the histogram of *r*-factor values for 1,000 randomly-sampled points. SR is not achievable at the points for which the *r*-factor exceeds unity; namely, 96 points out of 1,000 (9.6% of the VOI).

The method for calculating a confidence interval for this proportion is illustrated in Figure 5(b). We calculated the proportion of points for which the *r*-factor exceeds unity in 200 bootstrapped simulations; these values are plotted as a histogram. The 95% confidence interval is determined from the middle 95% of the histogram; it varies between 7.2% and 10.9%.

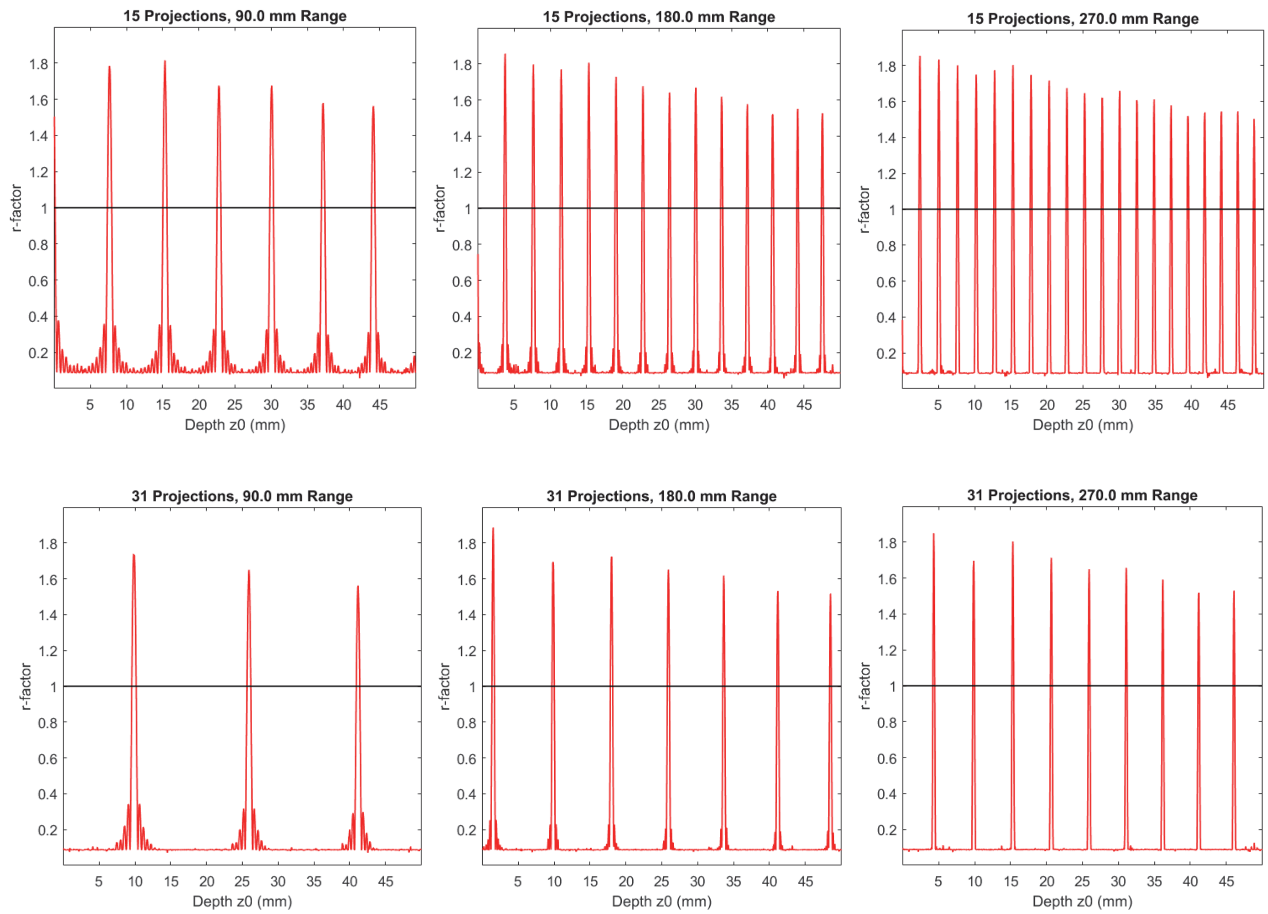

Figure 6. The r-factor is plotted as a function of depth (z_0), assuming $x_0 = 0$ and $y_0 = 40.0$ mm. The peaks correspond to depths at which SR is not achievable. The number of peaks can be minimized either by reducing the range of source motion (Q_x) or by increasing the number of projections (N).

3.D. Effect of Scan Range and Number of Projections

To illustrate the anisotropies, the r-factor is plotted along the z direction in Figure 6. Other than varying the z_0 coordinate of the test object, all other parameters are the same as those given in Table 1, assuming $x_0 = 0$ and $y_0 = 40.0$ mm. There are peaks at the positions for which SR is not achievable ($r \geq 1$).

Similar plots were shown in our previous work.[14] However, our previous work did not analyze how the anisotropies are dependent on the acquisition parameters. Figure 6 illustrates that the number of anisotropies can be minimized either by reducing the range of source motion (Q_x) or by increasing the number of projections (N). These two approaches are similar in that they both reduce the spacing between source positions.

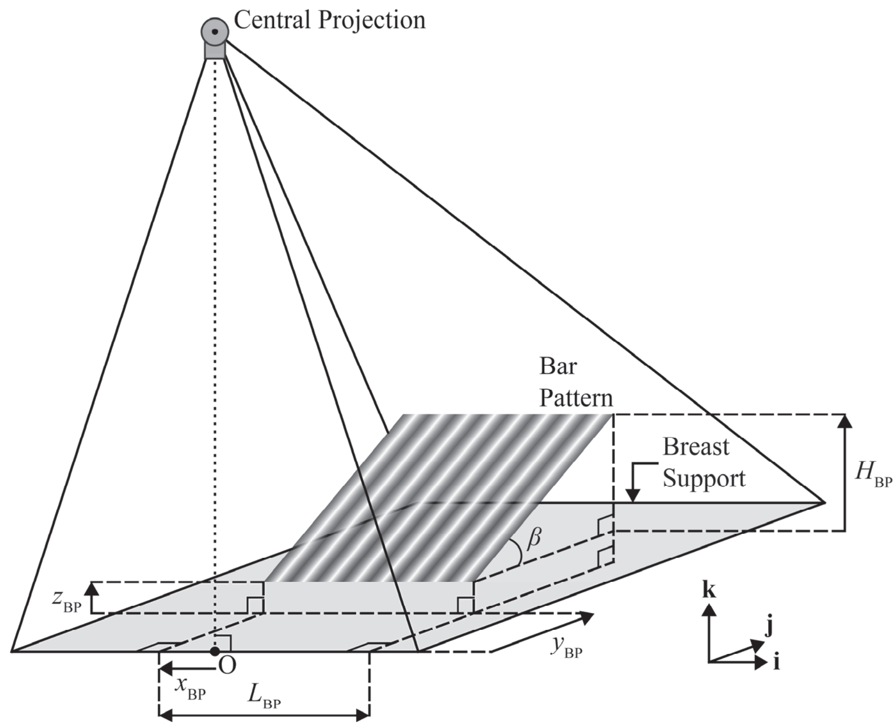

Figure 7. In x-ray experiments, the plane of a bar pattern (BP) phantom was oriented at an angle (β) relative to the breast support. The test frequency was oriented along the x direction ($\alpha = 0^o$), similar to the simulations. This setup was used to illustrate the anisotropies in SR along the z direction; *i.e.*, between the coordinates z_{BP} and $z_{BP} + H_{BP}$.

3.E. Experimental Validation

Our previous work demonstrated the existence of SR experimentally with a clinical DBT system (Selenia Dimensions, Hologic Inc., Bedford, MA).[14] To follow-up on these experiments, we now analyze the anisotropies in the same system. It should be noted that this system differs from the one considered in the simulations.

To visualize the anisotropies in the z direction, a bar pattern (BP) phantom was oriented at an angle (β), as shown in Figure 7. This setup allows for visualization of all the anisotropies between the coordinates z_{BP} and $z_{BP} + H_{BP}$. The input frequency is oriented along the x direction ($\alpha = 0°$), similar to the simulations, regardless of the value of β.

With this setup, we acquired images of the BP phantom described in our previous work[14] using a W/Al target-filter combination at 30 kV and 25 mAs. The reconstruction was prepared with Piccolo™ (Real Time Tomography, LLC, Villanova, PA).[29] This software has a feature that allows the user to align the reconstruction plane with the oblique plane of the phantom.

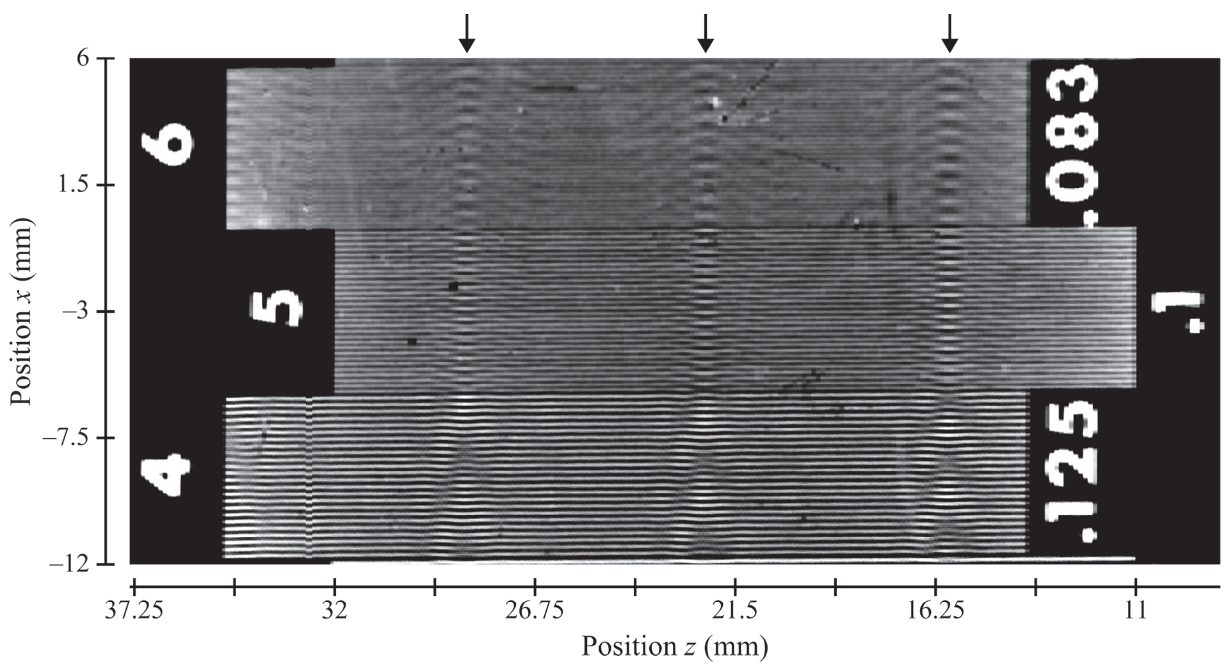

Figure 8. At the arrows, there are aliasing artifacts corresponding to the positions at which SR cannot be achieved.

Figure 8 shows the reconstruction of three test frequencies: 4.0, 5.0, and 6.0 line pairs per millimeter (lp/mm). These frequencies exceed the alias frequency (3.57 lp/mm) for a 0.140 mm detector. The reconstruction was prepared with 0.022 mm pixelation; this is smaller than the del size, allowing for SR.

Table 2. For one of the test frequencies (5.0 lp/mm), we used the reconstruction software to determine the values of the parameters shown in Figure 7.

Parameter	Value
β	47°
H_{BP}	21 mm
L_{BP}	6.0 mm
x_{BP}	–6.0 mm
y_{BP}	57 mm
z_{BP}	11 mm

The parameters shown in Figure 7, which describe the positioning of the phantom, can be determined with Piccolo™. These values are summarized in Table 2 for one of the test frequencies (5.0 lp/mm).

As one would expect from Section 3.D., SR is not achieved at all depths (z_0). There are aliasing artifacts indicated by the arrows in Figure 8. Figure 9 shows the signal through one artifact (the middle artifact out of the three) at the frequency 5.0 lp/mm. The peaks and troughs do not match those of the reference frequency; this demonstrates the presence of aliasing.

In the z direction, there are 6.34 and 6.49 mm spacing between the centroids of adjacent aliasing artifacts in Figure 8. Based on calculations for a rotating detector described in our previous work[14, 19], it can be shown that these spacings are predicted correctly to within absolute errors of 0.07 and 0.06 mm, respectively.

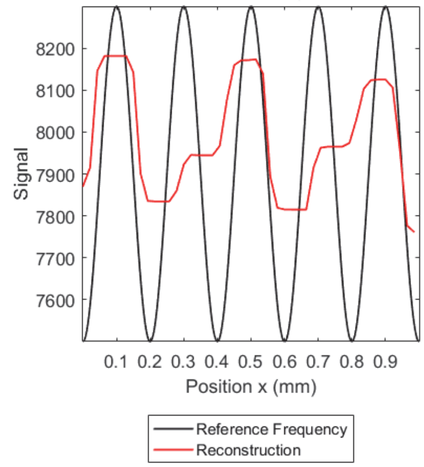

Figure 9. This plot shows the signal through one of the aliasing artifacts in Figure 8 (the middle artifact of the three denoted by arrows). The peaks and troughs do not match the reference frequency (5.0 lp/mm).

4. DISCUSSION

Our previous work demonstrated that SR is achievable in DBT, but that there are anisotropies throughout the reconstruction.[14] This paper develops a method for quantifying the relative abundance of the anisotropies. We used the *r*-factor to calculate the proportion of points in a VOI for which SR is not achievable ($r \geq 1$). With bootstrapped random sampling, it was demonstrated that the 95% confidence interval for this proportion varies between 7.2% and 10.9%.

We also analyzed whether the anisotropies can be minimized by varying the parameters in the acquisition geometry. There are fewer anisotropies in a system with a narrow range of source motion (Q_x). Previous work has shown that a narrow scan range gives rise to greater conspicuity and sensitivity in calcification imaging.[30]

Additionally, we investigated the effect of increasing the number of projections (N). This strategy also reduces the number of anisotropies. Analogy can be drawn to CT; according to Eq. (1), there is a gain in spatial resolution by increasing the number of projections. It should be emphasized that, although we can simulate an arbitrarily large number of projections, there are practical limits that need to be weighed in terms of scan time and radiation dose. Also, increasing the number of projections may result in greater electronic noise[31], which was not modeled in this paper but should be the subject of a future analysis.

The existence of the anisotropies was validated with a BP phantom using a clinical DBT system. The anisotropies were found at positions predicted from theoretical modeling.[14, 19] Although the Selenia Dimensions system was used to illustrate the anisotropies, similar results are expected in other DBT systems. The coordinates of the anisotropies are dependent on the acquisition geometry.

In this paper, the resolution at each point in the 3D image is determined using SBP reconstruction. One of the limitations of this paper is that there was no analysis of how filtering impacts SR. Since filtering places a different relative weight on each frequency in Fourier space, future work should determine whether the filter can be optimized to minimize the *r*-factor.

One assumption made in the theoretical model is that there are no sources of blurring in the x-ray converter, and hence the point spread function (PSF) is a delta function. Previous work demonstrated that this assumption is valid at normal incidence for amorphous-selenium (*a*-Se) detectors.[32] The AXS-2430 detector used in the simulations is an example of an *a*-Se detector, as is the Selenia Dimensions detector used experimentally (Section 3.E.). In an *a*-Se detector, the PSF is blurred at positions for which there is increasing obliquity in the incidence angle[33-35]; for example, near the edge of the detector opposite the chest wall. To model the blurring due to non-normal incidence in future work, the signal in the x-ray converter should be convolved with the PSF.

In the simulations (Sections 3.A. through 3.D.), the parameters were chosen based on the conventional design for DBT systems. However, the equations in Section 2 can also be applied to systems with more degrees of freedom in the motions of the source and detector. Our future work will explore whether SR can be achieved more uniformly by re-designing these motions.

5. CONCLUSION

Although SR is achievable in DBT, this paper demonstrates that anisotropies are unavoidable in the current design of the system. We develop a method for quantifying the proportion of the reconstruction volume in which there are anisotropies. The presence of anisotropies was validated experimentally with a BP phantom.

There are two strategies for minimizing the anisotropies: either reduce the range of source motion or increase the number of projections. Neither approach eliminates the anisotropies entirely. For this reason, our future work will explore the potential advantages of re-designing the motions of the source and detector.

ACKNOWLEDGEMENTS

We are grateful to David Higginbotham for his valuable feedback. In addition, we thank Johnny Kuo, Susan Ng, and Peter Ringer of Real Time Tomography (RTT) for providing technical assistance with Piccolo™.

Support was provided by grants PDF14302589 and IIR13264610 from Susan G. Komen®; grant W81XWH-18-1-0082 from the Department of Defense Breast Cancer Research Program; and grant 1R01CA196528 from the National Institute of Health. In addition, equipment support was provided by Analogic Inc., Barco NV, and RTT. The content is solely the responsibility of the authors and does not necessarily represent the official views of the funding agencies.

DISCLOSURE OF CONFLICTS OF INTEREST

Andrew D. A. Maidment is a scientific advisor to RTT, and his spouse is an employee and shareholder of RTT.

Symbol	Meaning
$\lfloor\ \rfloor$	Floor function defined in Eq. (30).
$\mathcal{A}$	X-Ray attenuation operator [Eq. (16)].
$\mathcal{D}$	Digitization operator [Eq. (24)].
$\mathcal{F}$	Fourier operator (subscript denotes dimension).
$\mathcal{L}$	Path length of ray through sine plate [Eq. (16)].
α	Polar angle of input frequency (Figure 2).
β	Angle of BP phantom (Figure 7).
ε	Thickness of sine plate (Figure 1).
κ_j	A quantity defined by Eqs. (21)-(22) to simplify intermediate calculations (j = 1, 2).
μ_{obj}	Attenuation coefficient of sine plate [Eq. (2)].
μ_{SBP}	SBP reconstruction of attenuation coefficient.
ν_{M}	Maximum resolvable frequency in CT [Eq. (1)].
ξ_j	A quantity defined by Eqs. (10)-(12) to simplify intermediate calculations (j = 1, 2, 3).
ψ	Full fan angle in CT [Eq. (1)].
A_1	Amplitude of highest Fourier peak less than alias frequency [Figure 4(d)].
A_2	Amplitude of Fourier peak at input frequency [Figure 4(d)].
a_x, a_y	Del dimensions; if subscripts are removed, del is square.
BP	Bar pattern.
b_z	Distance from breast support to detector.

C_{obj}	Amplitude of sine wave [Eq. (2)].
CT	Computed tomography.
DBT	Digital breast tomosynthesis.
Del	Detector element.
DM	Digital mammography.
f_0	Input frequency.
f_x''	Frequency in Fourier transform, measured along polar angle α.
FS	Focal spot.
H_{BP}	Height of BP phantom along z direction (Figure 7).
$J_{\mathrm{del},1}$	Number of samples (x direction) in integral for del sampling [Eq. (25)].
$J_{\mathrm{del},2}$	Number of samples (y direction) in integral for del sampling [Eq. (25)].
J_{FT}	Number of samples in middle sum approximation to Fourier transform [Eq. (34)].
L_{BP}	Length of BP phantom along x direction (Figure 7).
lp/mm	Line pairs per millimeter.
$\mathbf{m}$	Doublet with indices m_x and m_y used to identify dels.
$m_{\mathrm{SBP},x}$	Del index for detector position $u_{\mathrm{SBP},1}$ [Eq. (28)].
$m_{\mathrm{SBP},y}$	Del index for detector position $u_{\mathrm{SBP},2}$ [Eq. (29)].
n	Projection number.
$N_{\min}$	Minimum number of projections needed to resolve frequency ν_{M} in CT [Eq. (1)].
N	Number of projections.
NGT	"Next-generation" tomosynthesis.

PSF	Point spread function.
Q_x	Range of source motion along x direction.
r-Factor	Ratio of A_1 to A_2 [Eq. (36)].
R	Radius over which the frequency ν_{M} can be resolved in CT without aliasing [Eq. (1)].
SBP	Simple backprojection.
$u_{0,1}$	x-coordinate of point B on detector (Figure 2).
$u_{0,2}$	y-coordinate of point B on detector (Figure 2).
$u_{\mathrm{SBP},1}$	u_1-coordinate determined from ray between $(x_{\mathrm{FS}}, y_{\mathrm{FS}}, z_{\mathrm{FS}})$ and (x, y, z); calculated in Eq. (26).
$u_{\mathrm{SBP},2}$	u_2-coordinate determined from ray between $(x_{\mathrm{FS}}, y_{\mathrm{FS}}, z_{\mathrm{FS}})$ and (x, y, z); calculated in Eq. (27).
VOI	Volume-of-interest.
w	Parameter determining position along ray [Eq. (13)]; subscripts “entr” and “exit” denote the value at the entrance and exit surfaces of the sine plate.
x''	Transformed x-coordinate [Eq. (32)].
x''_{max}	Upper integration limit in Fourier transform [Eq. (33)].
x''_{min}	Lower integration limit in Fourier transform [Eq. (33)].
x_0	x-coordinate of centroid of sine plate.
x_{BP}	x-coordinate of left-most position of BP phantom (Figure 7).
x_{FS}	x-coordinate of focal spot.

y''	Transformed y-coordinate [Eq. (32)].
y_0	y-coordinate of centroid of sine plate.
y_{BP}	y-coordinate of edge of BP phantom that is most proximal to xz plane (Figure 7).
y_{FS}	y-coordinate of focal spot.
z''	Transformed z-coordinate [Eq. (32)].
z_0	z-coordinate of mid-thickness of sine plate.
z_{BP}	z-coordinate of edge of BP phantom that is most proximal to breast support (Figure 7).
z_{FS}	z-coordinate of focal spot.

Author to whom correspondence should be addressed. Electronic mail: Raymond.Acciavatti@uphs.upenn.edu; Telephone: +1-215-746-8759; Fax: +1-215-746-8764

REFERENCES

[1] Gur D, Zuley ML, Anello MI, Rathfon GY, Chough DM, Ganott MA, et al. Dose Reduction in Digital Breast Tomosynthesis (DBT) Screening using Synthetically Reconstructed Projection Images: An Observer Performance Study. Academic Radiology. 2012;19(2):166-71.

[2] Zuley ML, Guo B, Catullo VJ, Chough DM, Kelly AE, Lu AH, et al. Comparison of Two-dimensional Synthesized Mammograms versus Original Digital Mammograms Alone and in Combination with Tomosynthesis Images. Radiology. 2014;271(3):664-71.

[3] Skaane P, Bandos AI, Eben EB, Jebsen IN, Krager M, Haakenaasen U, et al. Two-View Digital Breast Tomosynthesis Screening with Synthetically Reconstructed Projection Images: Comparison with Digital Breast Tomosynthesis with Full-Field Digital Mammographic Images. Radiology. 2014;271(3):655-63.

[4] Gilbert FJ, Tucker L, Gillan MGC, Willsher P, Cooke J, Duncan KA, et al. Accuracy of Digital Breast Tomosynthesis for Depicting Breast Cancer Subgroups in a UK Retrospective Reading Study (TOMMY Trial). Radiology. 2015;277(3):697-706.

[5] Zuckerman SP, Conant EF, Keller BM, Maidment ADA, Barufaldi B, Weinstein SP, et al. Implementation of Synthesized Two-dimensional Mammography in a Population-based Digital Breast Tomosynthesis Screening Program. Radiology. 2016;281(3):730-6.

[6] Zuckerman SP, Maidment ADA, Weinstein SP, McDonald ES, Conant EF. Imaging With Synthesized 2D Mammography: Differences, Advantages, and Pitfalls Compared With Digital Mammography. American Journal of Roentgenology. 2017;209:222-9.

[7] Aujero MP, Gavenonis SC, Benjamin R, Zhang Z, Holt JS. Clinical Performance of Synthesized Two-dimensional Mammography Combined with Tomosynthesis in a Large Screening Population. Radiology. 2017;283(1):70-6.

[8] Ratanaprasatporn L, Chikarmane SA, Giess CS. Strengths and Weaknesses of Synthetic Mammography in Screening. RadioGraphics. 2017;37(7):1913-27.

[9] Friedewald SM, Rafferty EA, Rose SL, Durand MA, Plecha DM, Greenberg JS, et al. Breast Cancer Screening Using Tomosynthesis in Combination With Digital Mammography. Journal of the American Medical Association. 2014;311(24):2499-507.

[10] Vedantham S, Karellas A, Vijayaraghavan GR, Kopans DB. Digital Breast Tomosynthesis: State of the Art. Radiology. 2015;277(3):663-84.

[11] McDonald ES, Oustimov A, Weinstein SP, Synnestvedt MB, Schnall M, Conant EF. Effectiveness of Digital Breast Tomosynthesis Compared With Digital Mammography: Outcomes Analysis From 3 Years of Breast Cancer Screening. JAMA Oncology. 2016;2(6):737-43.

[12] Sharpe RE, Venkataraman S, Phillips J, Dialani V, Fein-Zachary VJ, Prakash S, et al. Increased Cancer Detection Rate and Variations in the Recall Rate Resulting from Implementation of 3D Digital Breast Tomosynthesis into a Population-based Screening Program. Radiology. 2016;278(3):698-706.

[13] Rafferty EA, Park JM, Philpotts LE, Poplack SP, Sumkin JH, Halpern EF, et al. Assessing Radiologist Performance Using Combined Digital Mammography and Breast Tomosynthesis Compared with Digital Mammography Alone: Results of a Multicenter, Multireader Trial. Radiology. 2013;266(1):104-13.

[14] Acciavatti RJ, Maidment ADA. Observation of super-resolution in digital breast tomosynthesis. Medical Physics. 2012;39(12):7518-39.

[15] Acciavatti RJ, Maidment ADA. Oblique reconstructions in tomosynthesis: II. Super-resolution. Medical Physics. 2013;40(11):111912-1 to -19.

[16] Acciavatti RJ, Maidment ADA, editors. Investigating the Potential for Super-Resolution in Digital Breast Tomosynthesis. SPIE Medical Imaging; 2011; Lake Buena Vista, FL: SPIE.

[17] Acciavatti RJ, Mein SB, Maidment ADA. Investigating Oblique Reconstructions with Super-Resolution in Digital Breast Tomosynthesis. Lecture Notes in Computer Science. 2012;7361:737-44.

[18] Acciavatti RJ, Maidment ADA. Proposing an Acquisition Geometry That Optimizes Super-Resolution in Digital Breast Tomosynthesis. Lecture Notes in Computer Science. 2012;7361:386-93.

[19] Acciavatti RJ, Wileyto EP, Maidment ADA, editors. Modeling Acquisition Geometries with Improved Super-Resolution in Digital Breast Tomosynthesis. SPIE Medical Imaging; 2016; San Diego, CA: SPIE.

[20] Hsieh J. Chapter 7: Image Artifacts: Appearances, Causes, and Corrections. Computed Tomography: Principles, Design, Artifacts, and Recent Advances. Bellingham, WA: SPIE Press; 2015. p. 245-347.

[21] Hsieh J, Slack CC, Dutta S, Gordon CL, Li J, Chao E, editors. Adaptive view synthesis for aliasing artifact reduction. SPIE Medical Imaging; 2001: SPIE.

[22] Joseph PM, Schulz RA. View sampling requirements in fan beam computed tomography. Medical Physics. 1980;7(6):692-702.

[23] Barrett HH, Myers KJ. Chapter 3: Fourier Analysis. In: Saleh BEA, editor. Foundations of Image Science. New York, NY: John Wiley & Sons; 2004. p. 95-174.

[24] Ferris WS, Vent TL, Maidment TD, Acciavatti RJ, Wurtele DE, Maidment ADA, editors. Geometric Calibration for a Next-Generation Digital Breast Tomosynthesis System. SPIE Medical Imaging; 2017; Orlando, FL: SPIE.

[25] Maidment TD, Vent TL, Ferris WS, Wurtele DE, Acciavatti RJ, Maidment ADA, editors. Comparing the Imaging Performance of Computed Super Resolution and Magnification Tomosynthesis. SPIE Medical Imaging; 2017; Orlando, FL: SPIE.

[26] Acciavatti RJ, Rodriguez-Ruiz A, Vent TL, Bakic PR, Reiser I, Sechopoulos I, et al., editors. Analysis of Volume Overestimation Artifacts in the Breast Outline Segmentation in Tomosynthesis. SPIE Medical Imaging; 2018; Houston, TX: SPIE.

[27] Choi CJ, Vent TL, Acciavatti RJ, Maidment ADA, editors. Geometric Calibration for a Next-Generation Digital Breast Tomosynthesis System Using Virtual Line Segments. SPIE Medical Imaging; 2018; Houston, TX: SPIE.

[28] Eben JE, Vent TL, Choi CJ, Yarrabothula S, Chai L, Nolan M, et al., editors. Development of a Next Generation Tomosynthesis System. SPIE Medical Imaging; 2018; Houston, TX: SPIE.

[29] Kuo J, Ringer PA, Fallows SG, Bakic PR, Maidment ADA, Ng S, editors. Dynamic Reconstruction and Rendering of 3D Tomosynthesis Images. SPIE Medical Imaging; 2011; Lake Buena Vista, FL: SPIE.

[30] Chan H-P, Goodsitt MM, Helvie MA, Zelakiewicz S, Schmitz A, Noroozian M, et al. Digital Breast Tomosynthesis: Observer Performance of Clustered Microcalcification Detection on Breast Phantom Images Acquired with an Experimental System Using Variable Scan Angles, Angular Increments, and Number of Projections Views. Radiology. 2014;273(3):675-85.

[31] Sechopoulos I. A review of breast tomosynthesis. Part I. The image acquisition process. Medical Physics. 2013;40(1):014301-1 to -12.

[32] Rowlands JA, Yorkston J. Chapter 4: Flat Panel Detectors for Digital Radiography. In: Beutel J, Kundel HL, Van Metter RL, editors. Handbook of Medical Imaging Volume 1 Physics and Psychophysics. 1. Bellingham, WA: SPIE - The International Society for Optical Engineering; 2000. p. 223-328.

[33] Que W, Rowlands JA. X-ray imaging using amorphous selenium: Inherent spatial resolution. Medical Physics. 1995;22(4):365-74.

[34] Hajdok G, Cunningham IA, editors. Penalty on the detective quantum efficiency from off-axis incident x rays. Medical Imaging 2004: Physics of Medical Imaging; 2004; San Diego, CA: SPIE.
[35] Badano A, Freed M, Fang Y. Oblique incidence effects in direct x-ray detectors: A first-order approximation using a physics-based analytical model. Medical Physics. 2011;38(4):2095-8.

Personalization of X-Ray Tube Motion in Digital Breast Tomosynthesis Using Virtual Defrise Phantoms

Raymond J. Acciavatti[1], Bruno Barufaldi[1], Trevor L. Vent[1],
E. Paul Wileyto[2], Andrew D. A. Maidment[1]
[1]University of Pennsylvania, Department of Radiology, 3400 Spruce Street, Philadelphia PA 19104
[2]University of Pennsylvania, Department of Epidemiology, Biostatistics, & Informatics,
423 Guardian Drive, Philadelphia PA 19104
E-mail: {Raymond.Acciavatti@uphs | Bruno.Barufaldi@uphs | tvent@seas |
epw@pennmedicine | Andrew.Maidment@uphs}.upenn.edu

ABSTRACT

In digital breast tomosynthesis (DBT), projection images are acquired as the x-ray tube rotates in the plane of the chest wall. We constructed a prototype next-generation tomosynthesis (NGT) system that has an additional component of tube motion in the perpendicular direction (*i.e.*, posteroanterior motion). Our previous work demonstrated the advantages of the NGT system using the Defrise phantom. The reconstruction shows higher contrast and fewer blurring artifacts. To expand upon that work, this paper analyzes how image quality can be further improved by customizing the motion path of the x-ray tube based on the object being imaged. In simulations, phantoms are created with realistic 3D breast outlines based on an established model of the breast under compression. The phantoms are given an internal structure similar to a Defrise phantom. Two tissue types (fibroglandular and adipose) are arranged in a square-wave pattern. The reconstruction is analyzed as a binary classification task using thresholding to segment the two tissue types. At various thresholds, the classification of each voxel in the reconstruction is compared against the phantom, and receiver operating characteristic (ROC) curves are calculated. It is shown that the area under the ROC curve (AUC) is dependent on the x-ray tube trajectory. The trajectory that maximizes AUC differs between phantoms. In conclusion, this paper demonstrates that the acquisition geometry in DBT should be personalized to the object being imaged in order to optimize the image quality.

Keywords: Digital Breast Tomosynthesis, Mammography, X-Ray Imaging, Digital Imaging, Defrise Phantom, Image Quality, Image Reconstruction, Receiver Operating Characteristic Curve.

1. INTRODUCTION

The Defrise phantom is a test object for evaluating image quality in cone-beam computed tomography (CT). The phantom consists of multiple disks, which are spaced along the direction perpendicular to the plane of source motion. In the reconstruction, there is a cone-beam artifact along this direction; the spacings between the disks are not properly visualized at positions distal to the plane of source motion.[1]

One application of the Defrise phantom is to demonstrate the advantage of new acquisition geometries for CT. For example, in the work of Becker *et al*., a multisource system for dedicated breast CT was evaluated.[2] The system was built with five sources, which were spaced in 2.0 cm increments along the direction of the cone-beam artifact. The contrast between disks was used to quantify image quality. With multisource scanning, there is a broader range of positions over which contrast is within detectable limits, yielding an improvement in image quality over single-source scanning.

Our previous work showed that the Defrise phantom can also be used to evaluate image quality in digital breast tomosynthesis (DBT).[3,4] We demonstrated the existence of a cone-beam artifact along the posteroanterior (PA) direction, which is perpendicular to the motion of the source. To show that image quality can be improved, we later constructed a prototype next-generation tomosynthesis (NGT) system, which is capable of source motion with an additional degree of freedom in the PA direction.[5,6] Although a single source is used in the NGT system, our strategy for

Medical Imaging 2019: Physics of Medical Imaging, edited by Taly Gilat Schmidt, Guang-Hong Chen, Hilde Bosmans,
Proc. of SPIE Vol. 10948, 109480B · © 2019 SPIE · CCC code: 1605-7422/19/$18 · doi: 10.1117/12.2511780

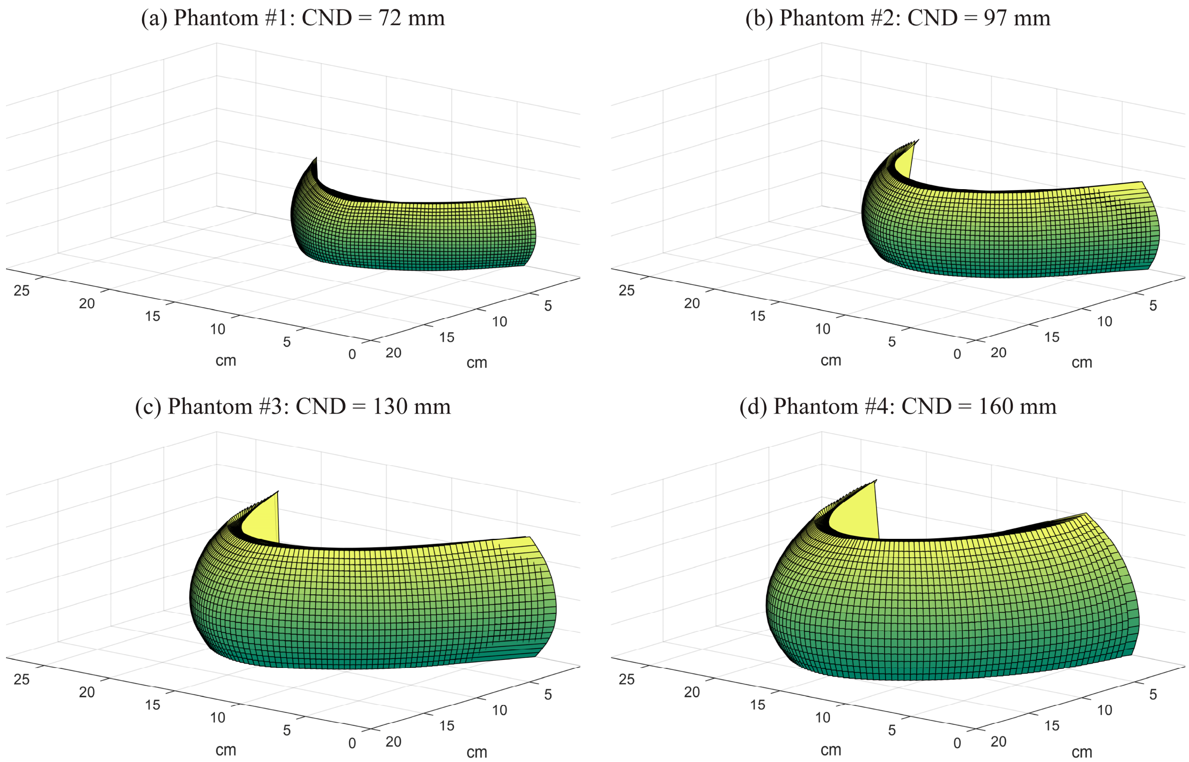

Figure 1. Breast outlines under compression are shown for four phantoms using the model of Rodríguez-Ruiz *et al.*[7]

improving the image quality is similar to the one used by Becker *et al.*[2] in that source positions are introduced along the direction of the cone-beam artifact.

The latest CT scanners incorporate the newest trends in personalized medicine. In point-of-care CT, the scan orbit is customized to the clinical task and body habitus.[8-14] The purpose of this paper is to demonstrate that the acquisition settings in DBT also need to be personalized to each patient. We model virtual Defrise phantoms that are created in the shape of the 3D breast outline under compression.[7] Various acquisition geometries are simulated for each phantom. This paper shows that a given scan motion will not benefit all phantoms the same way. The best image quality is achieved by customizing the motion of the source to the dimensions of the phantom.

2. METHODS

2.1 Phantom Model

Four phantoms were considered for the purpose of this study. The 3D phantom outlines were created based on previous work modeling the breast under compression.[7] Figure 1 shows the output of the MATLAB® software developed by that work. Random phantoms with “advanced 3D curvature” were generated by specifying thicknesses of 45, 55, 75, and 85 mm in this software. Table 1 shows the chest-wall to nipple distance (CND) for each phantom. We truncated some slices at the superior surface of each phantom, as we did in our previous work[15], since the shape of the breast outline was not representative of a breast under compression in these slices. More specifically, three slices in phantom #1, four slices in phantom #2, five slices in phantom #3, and six slices in phantom #4 were truncated. The resultant thicknesses of each phantom are summarized in Table 1.

The 3D breast outline was initially created with 1.0 mm^3 voxels, and then up-sampled to 0.50 mm^3 voxels. Each phantom was given internal structure consisting of two tissue types (fibroglandular and adipose) arranged in a square-wave pattern with a frequency of 0.17 mm^{-1} oriented in the PA direction. This frequency is chosen based on our previous work on the Defrise phantom.[3,4]

Table 1. Four phantoms with different sizes and shapes were analyzed in this simulation study.

Phantom		CND: Chest-Wall to Nipple Distance (mm)	Thickness (mm)		kV	mAs
#1		72	40		29	45
#2		97	50		31	52
#3		130	69		35	72
#4		160	77		37	70

2.2 X-Ray Projection Images

X-ray projection images were simulated with ray-tracing software developed for virtual clinical trials.[16] For the purpose of this study, there were no sources of noise or blurring. Also, the AXS-2430 detector (Analogic Canada Corporation, Montreal, Quebec, Canada) was simulated, since this is the detector used in the NGT system. This detector has 0.085 mm pixels and an active area of 304.64 mm × 239.36 mm.

The kV and mAs for each projection image were determined from a table developed by Feng and Sechopoulos for the automatic exposure control (AEC) settings in DBT for a W/Al target filter combination.[17] According to that table, the kV is dependent on the compressed breast thickness. The kV for each phantom was determined by linear interpolation. This result was rounded to the nearest integer. Next, the mAs was determined based on the kV using linear interpolation, assuming a glandular fraction of 50%.

Figure 2 illustrates an example of a source motion supported by the NGT system. There are components of motion in both the conventional tube travel direction (x) and the PA direction (y). The source can be positioned at arbitrary points in these two directions; for example, along the outline of an ellipse. The trajectory shown in Figure 2 consists of two concentric half-ellipses. The semi-axis lengths for the outer ellipse are a and b in the x and y directions, respectively. These parameters control the range of source motion in each direction. The lengths of the axes of the inner ellipse are modeled to be half of these values.

For the purpose of this paper, we assume that the source positions are displaced around each half-ellipse in 30° increments and that there is an additional source position at the centroid of the ellipses. Hence there are 15 projection images. We define the centroid at the midpoint of the chest wall; this matches the central source position in a conventional DBT scan. The x- and y-coordinates of the focal spot (FS) can be described in terms of the projection number (n) based on the equations

$$x_{\mathrm{FS}} = \begin{cases} 0, & n = 1 \\ \dfrac{a}{2} \cdot \cos\left[\left(n-2 \right) \dfrac{\pi}{6} \right], & 2 \le n \le 8 \\ a \cdot \cos\left[(15-n) \dfrac{\pi}{6} \right], & 9 \le n \le 15 \end{cases} \tag{1}$$

$$y_{\mathrm{FS}} = \begin{cases} 0, & n = 1 \\ \dfrac{b}{2} \cdot \sin\left[\left(n-2 \right) \dfrac{\pi}{6} \right], & 2 \le n \le 8 \\ b \cdot \sin\left[(15-n) \dfrac{\pi}{6} \right], & 9 \le n \le 15 \end{cases} , \tag{2}$$

where n varies between 1 and 15 in integer steps. Figure 2 illustrates the ordering of the FS positions, as shown by the arrows. In all projections, the source-to-support distance is 621.0 mm and the source-to-image distance (SID) is 652.0 mm.

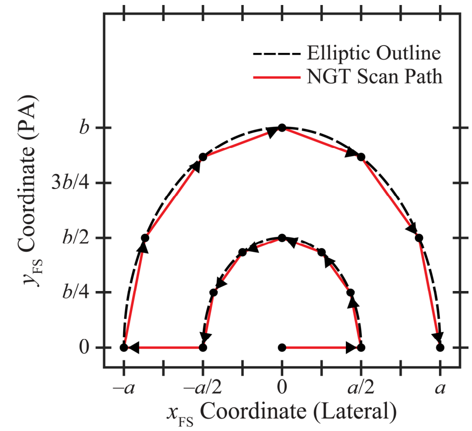

Figure 2. In this trajectory, there are five source positions along the chest wall and 10 additional source positions in the PA direction. The parameters a and b control the range of source motion in each direction.

If Eqs. (1)-(2) were used in the special case $b = 0$, there would be three overlapping FS coordinates at the point (0, 0); *i.e.*, the midpoint of the chest wall. For this reason, a different motion needs to be considered to simulate the conventional acquisition geometry. In this paper, this motion is simulated with equal spacing between source positions; namely, $x_{FS} = a \cdot (n - 8) / 7$. The range of source motion is thus $2a$ in the x direction, similar to Eq. (1). It should be noted that the SID is held constant in the NGT system for all acquisition geometries. Therefore, the simulation of the conventional motion differs from a clinical system in which the source rotates in a circular arc in the plane of the chest wall.

For these simulations, a is varied between 50.0 and 150.0 mm in 5.0 mm increments (or 21 steps), and b is varied between 0 and 200.0 mm in 10.0 mm increments (also 21 steps). This results in 441 acquisition geometries that are simulated. We determine the optimum acquisition geometry for each phantom using the approach described in Section 2.3.

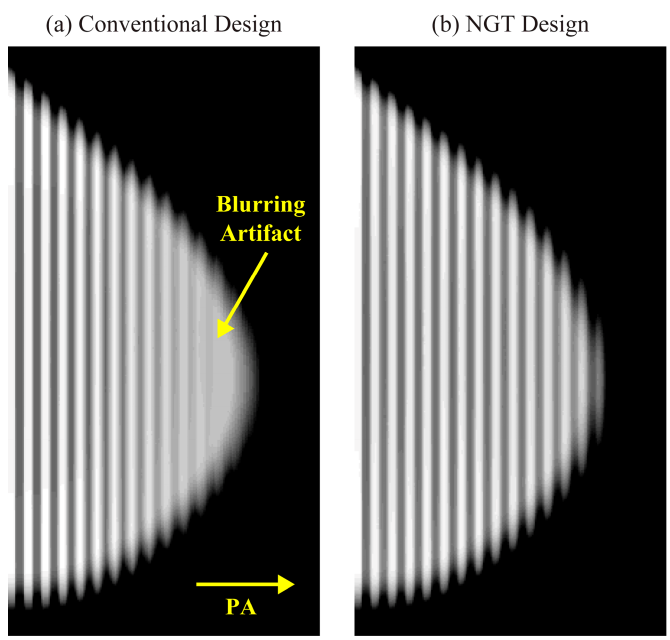

Figure 3. (a) In the central slice of the reconstruction for phantom #2, there is loss of image quality in the PA direction in the conventional design, as shown by the blurring artifact. (b) The NGT design offers better image quality in the PA direction ($b = 90$ mm).

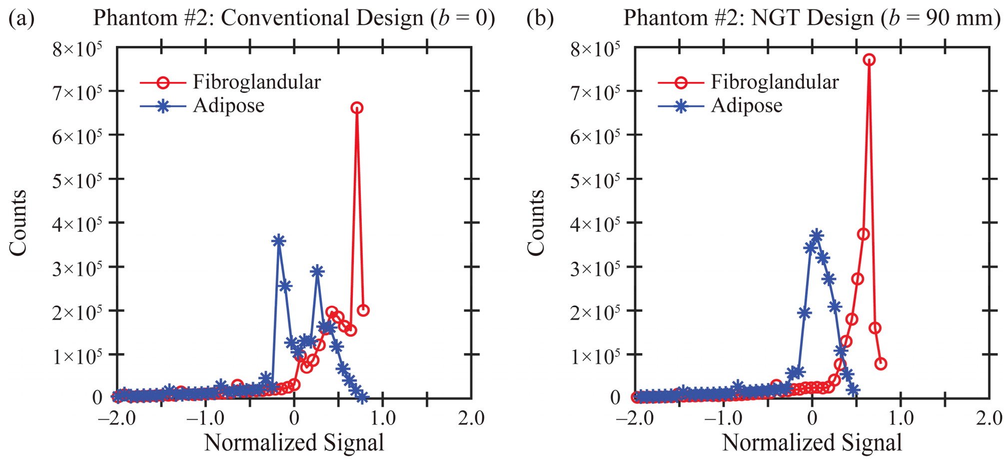

Figure 4. Using the reconstruction obtained with phantom #2, the histograms for the signal in each tissue type (fibroglandular and adipose) are calculated. The separation between the two tissue types is more pronounced in the NGT design (b) than in the conventional design (a).

2.3 Image Analysis

Reconstructions were calculated with Briona™ (Real Time Tomography, LLC, Villanova, PA) with an in-plane pixelation of 0.085 mm × 0.085 mm and a slice spacing of 0.50 mm. Subsequently, the reconstructions were re-scaled to the voxel size of the phantom with bicubic interpolation.

Receiver operating characteristic (ROC) curves were then calculated by using thresholding to segment the two tissue types.[18] Each voxel was classified as fibroglandular tissue (FGT) if the signal exceeds a user-specified threshold. All other voxels were classified as adipose tissue (AT). We define the true positive rate (TPR) as the ratio of the number of voxels classified correctly as FGT to the total number of fibroglandular voxels in the input phantom. The false positive rate (FPR) is the ratio of the number of voxels classified incorrectly as FGT to the total number of adipose voxels in the input phantom. ROC curves were generated by calculating TPR and FPR at all possible thresholds. The area under the ROC curve (AUC) was calculated as a figure-of-merit to identify the acquisition geometry that maximizes the image quality for each phantom.

3. RESULTS

3.1 Results for Conventional and NGT Designs

Figure 3 illustrates the central slice in the reconstruction for the conventional and NGT designs for one phantom (#2). Both figures presume that the range of source motion in the x direction is 200.0 mm; *i.e.*, a = 100.0 mm. As one would expect from previous work[3-6], there is a blurring artifact at positions distal to the chest wall in the conventional design [Figure 3(a)]. It is difficult to discern the spacings between the two tissue types at these positions. By contrast, in the NGT design with PA source motion (b = 90 mm), the relative contrast is improved [Figure 3(b)].

To analyze these results more quantitatively, the signal in each tissue type is visualized with a histogram in Figure 4. These histograms are created using all slices in the reconstruction, not just the central slice shown in Figure 3. The signal (I) has been re-scaled with Z-score normalization based on the mean (μ) and standard deviation (σ) for each tissue type. Eq. (3) describes this transformation. The origin is shifted halfway between the means of each distribution. Also, the signal is normalized by the pooled standard deviation.

$$Z = \frac{I - \dfrac{\mu_{\mathrm{FGT}} + \mu_{\mathrm{AT}}}{2}}{\sqrt{\dfrac{\sigma_{\mathrm{FGT}}^2 + \sigma_{\mathrm{AT}}^2}{2}}} \tag{3}$$

In Figure 4, the distributions are plotted to within ± two units of the pooled standard deviation. As can be seen from this figure, the histograms are highly skewed to the left, and therefore, the tails in the extreme left have been truncated.

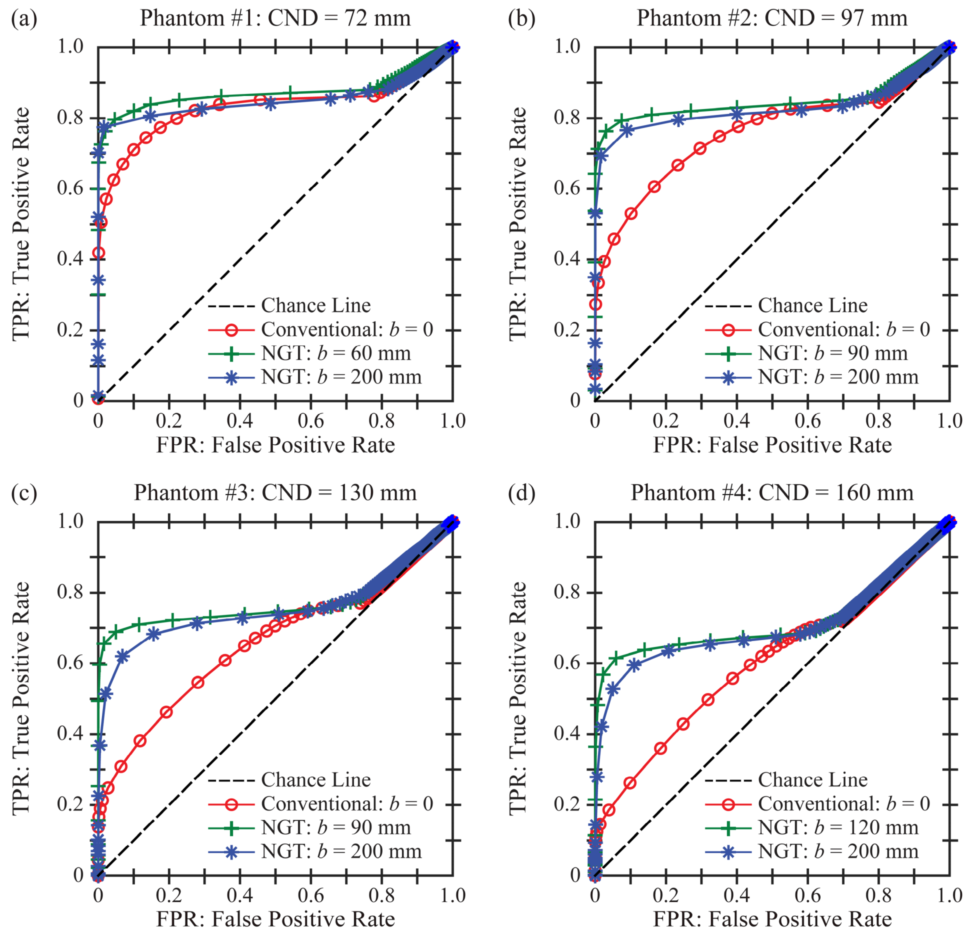

Figure 5. The reconstruction is analyzed as a binary classification task. A threshold is used to segment the two tissue types (fibroglandular and adipose). For each phantom, ROC curves are calculated for three acquisition geometries by varying the threshold, assuming $a = 100.0$ mm. The three acquisition geometries differ in terms of the range of PA source motion; *i.e.*, the conventional design, the NGT design with the highest AUC, and the NGT design with the broadest range of PA source motion.

For image quality to be high, there needs to be a clear separation between the FGT and AT histograms. This separation can be quantified in terms of a ROC curve [Figure 5(b)]. Each point on the ROC curve is calculated using a different threshold to segment the two tissue types. The NGT design for which b = 90 mm offers an improvement in image quality (AUC = 0.85) relative to the conventional design (AUC = 0.76). In Section 3.2, AUC is analyzed in all 441 acquisition geometries in order to identify the optimum scan parameters for each phantom.

3.2 Optimization of the Acquisition Geometry

Figure 6 shows a surface plot of AUC as a function of the scan parameters (a and b) for each phantom. These plots first illustrate that the image quality is effectively independent of the parameter a; *i.e.*, the range of source motion perpendicular to the input frequency. The parameter b, which controls the range of motion in the PA direction, has a more pronounced effect on AUC.

Figure 6 can be used to calculate the value of b that maximizes AUC. Assuming that $a = 100.0$ mm, the optimum values of b are 60, 90, 90, and 120 mm for phantoms #1 to #4, respectively. These optimum values are correlated with CND; Pearson's correlation coefficient is 94%. These results illustrate the benefit of personalizing the source motion based on the dimensions of the phantom.

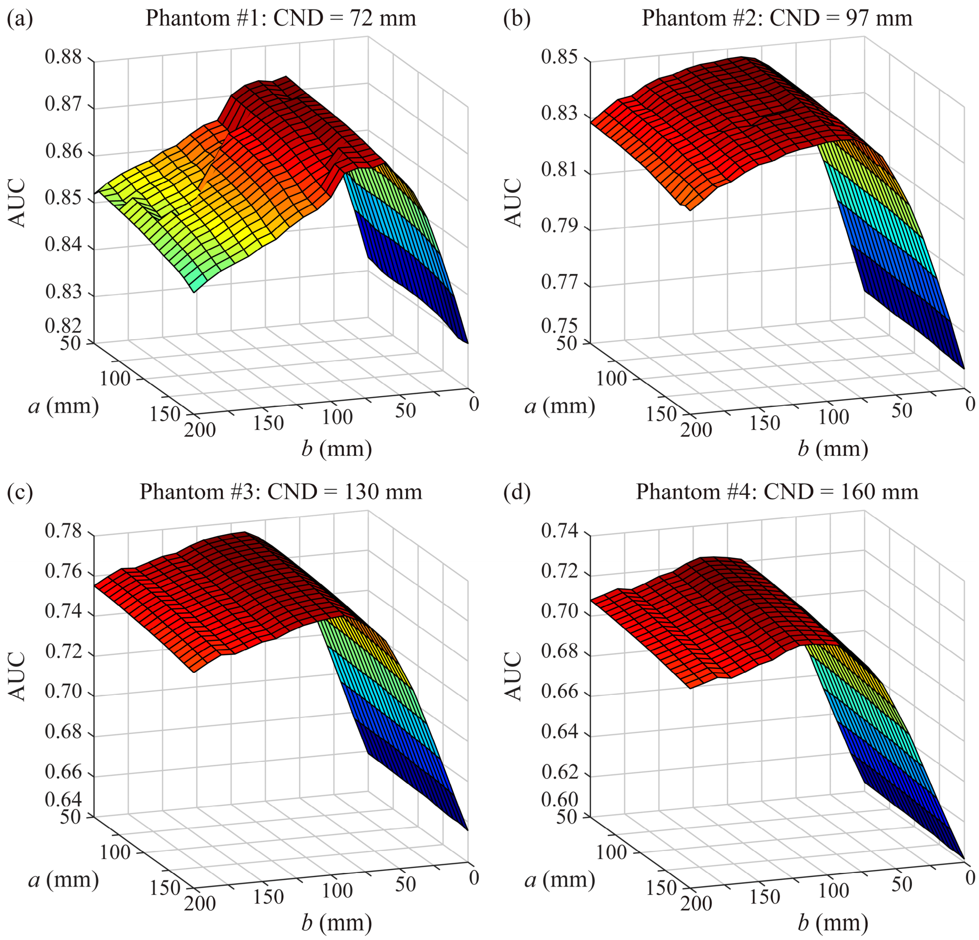

Figure 6. For each phantom, the AUC is plotted as a function of the scan parameters. These results are used to identify the optimum acquisition geometry for each phantom. In these simulations, the input frequency is oriented in the PA direction. The parameter a controls the range of source motion in the perpendicular direction; this parameter has only a small effect on AUC. By contrast, the parameter b needs to be customized to each phantom to optimize the image quality. It should be noted that the range of values in the vertical axis differs between subplots.

For each phantom, the ROC curve for the optimum geometry is compared against the conventional geometry in Figure 5. We continue to make the assumption that a = 100.0 mm. As shown, there is an improvement in AUC; namely, ΔAUC = 0.040, 0.088, 0.115, and 0.118 for phantoms #1 to #4, respectively. Figures 5-6 demonstrate that the phantoms with larger dimensions have inherently lower AUC. This result is expected from previous work, which showed that increasing the thickness of the phantom results in less relative contrast in the reconstruction.[4]

In addition, the ROC curves for the broadest range of PA motion (b = 200.0 mm) are shown in Figure 5. This motion is also characterized by an improvement over the conventional geometry; namely, ΔAUC = 0.019, 0.068, 0.095, and 0.101 for the four respective phantoms.

4. DISCUSSION AND CONCLUSION

In this paper, virtual Defrise phantoms are created in the shape of breasts under compression. There are two tissue types in the phantom (FGT and AT). Consequently, the reconstruction can be analyzed voxel-by-voxel as a binary classification task with a ROC curve. We find that the source motion needs to be customized to the dimensions of the phantom to maximize the AUC. Specifically, as the CND increases, the source needs to traverse a broader range of motion in the PA direction. Since the scan time is proportionate with the path length of the source motion, these results suggest that the phantoms with the broadest CND will require the longest scan time.

Figures 5-6 show that the improvement over the conventional geometry is preserved as the range of PA motion increases beyond the optimum value. However, this comes with the trade-off of increasing the scan time, and therefore, increasing the potential for blurring due to patient motion.[19] Another disadvantage of a longer scan time is prolonging the discomfort associated with breast compression.

One limitation of this paper is that, based on the orientation of the input frequency, image quality is investigated in only one direction (PA). There was no analysis of image quality in the conventional tube travel direction (x). Previous work has demonstrated that image quality is indeed dependent on the range of source motion in this direction. For example, a narrow range of source motion has been shown to be beneficial in calcification imaging.[20] Future work needs to investigate how the source motion can be optimized based on the imaging task.

The results of this paper were determined using a limited number of phantoms. In future work, additional phantoms with different sizes, shapes, and internal compositions should be analyzed, including anthropomorphic phantoms[21-23] with more complex fibroglandular distributions. Future work also needs to investigate whether the CND could be estimated from a low-dose scout image; in a clinical exam, the CND is not known *a priori* as is the case with a phantom. The source motion could be customized around the dimensions obtained from the scout image.

5. ACKNOWLEDGEMENT

The authors acknowledge the early work of Margaret Nolan, Elizabeth Kobe, Sushmitha Yarrabothula, and Lucy Chai at the University of Pennsylvania on this topic. We also thank Johnny Kuo, Susan Ng, and Peter Ringer of Real Time Tomography for technical assistance with Briona™. Andrew D. A. Maidment is a shareholder of Real Time Tomography, and is a member of the scientific advisory board.

Support was provided by the following grants: W81XWH-18-1-0082 from the Department of Defense Breast Cancer Research Program, IRSA 1016451 from the Burroughs Wellcome Fund, 1R01CA196528 from the National Institute of Health, and IIR13264610 from Susan G. Komen®. In addition, equipment support was provided by Analogic Inc., Barco NV, and Real Time Tomography. The content is solely the responsibility of the authors and does not necessarily represent the official views of the funding agencies.

6. REFERENCES

1. Hsieh J. Chapter 10: Multislice and Cone-beam CT. *Computed Tomography: Principles, Design, Artifacts, and Recent Advances*. Third ed. Bellingham, WA: SPIE Press; 2015:423-486.
2. Becker AE, Hernandez AM, Schwoebel P, Boone JM. Multisource x-ray system for artifact reduction in dedicated breast CT. Paper presented at: 14th International Workshop on Breast Imaging (IWBI 2018)2018; Atlanta, GA.
3. Acciavatti RJ, Chang A, Woodbridge L, Maidment ADA. Optimizing the Acquisition Geometry for Digital Breast Tomosynthesis Using the Defrise Phantom. Paper presented at: SPIE Medical Imaging2014; San Diego, CA.
4. Acciavatti RJ, Mannherz W, Nolan M, Maidment ADA. An Alternate Design for the Defrise Phantom To Quantify Resolution in Digital Breast Tomosynthesis. Paper presented at: SPIE Medical Imaging2017; Orlando, FL.
5. Maidment TD, Vent TL, Ferris WS, Wurtele DE, Acciavatti RJ, Maidment ADA. Comparing the Imaging Performance of Computed Super Resolution and Magnification Tomosynthesis. Paper presented at: SPIE Medical Imaging2017; Orlando, FL.
6. Eben JE, Vent TL, Choi CJ, et al. Development of a Next Generation Tomosynthesis System. Paper presented at: SPIE Medical Imaging2018; Houston, TX.
7. Rodriguez-Ruiz A, Agasthya GA, Sechopoulos I. The compressed breast during mammography and breast tomosynthesis: in vivo shape characterization and modeling. *Physics in Medicine and Biology.* 2017;62:6920-6937.
8. Siewerdsen JH, Moseley DJ, Burch S, et al. Volume CT with a flat-panel detector on a mobile, isocentric C-arm: Pre-clinical investigation in guidance of minimally invasive surgery. *Medical Physics.* 2005;32(1):241-254.
9. Schafer S, Nithiananthan S, Mirota DJ, et al. Mobile C-arm cone-beam CT for guidance of spine surgery: Image quality, radiation dose, and integration with interventional guidance. *Medical Physics.* 2011;38(8):4563-4574.
10. Dang H, Stayman JW, Sisniega A, et al. Statistical reconstruction for cone-beam CT with a post-artifact-correction noise model: application to high-quality head imaging. *Physics in Medicine and Biology.* 2015;60:6153-6175.

11. Sisniega A, Zbijewski W, Xu J, et al. High-fidelity artifact correction for cone-beam CT imaging of the brain. *Physics in Medicine and Biology.* 2015;60:1415-1439.

12. Xu J, Sisniega A, Zbijewski W, et al. Modeling and design of a cone-beam CT head scanner using task-based imaging performance optimization. *Physics in Medicine and Biology.* 2016;61:3180-3207.

13. Ouadah S, Jacobson M, Stayman JW, Ehtiati T, Weiss C, Siewerdsen JH. Task-Driven Orbit Design and Implementation on a Robotic C-Arm System for Cone-Beam CT. Paper presented at: SPIE Medical Imaging2017; Orlando, FL.

14. Gang GJ, Stayman JW, Ehtiati T, Siewerdsen JH. Task-driven image acquisition and reconstruction in cone-beam CT. *Physics in Medicine and Biology.* 2015;60:3129-3150.

15. Acciavatti RJ, Rodriguez-Ruiz A, Vent TL, et al. Analysis of Volume Overestimation Artifacts in the Breast Outline Segmentation in Tomosynthesis. Paper presented at: SPIE Medical Imaging2018; Houston, TX.

16. Barufaldi B, Higginbotham D, Bakic PR, Maidment ADA. OpenVCT: A GPU-Accelerated Virtual Clinical Trial Pipeline for Mammography and Digital Breast Tomosynthesis. Paper presented at: SPIE Medical Imaging2018; Houston, TX.

17. Feng SSJ, Sechopoulos I. Clinical Digital Breast Tomosynthesis System: Dosimetric Characterization. *Radiology.* 2012;263(1):35-42.

18. Bakic PR, Ng S, Ringer P, Carton A-K, Conant EF, Maidment ADA. Validation and Optimization of Digital Breast Tomosynthesis Reconstruction using an Anthropomorphic Software Breast Phantom. Paper presented at: SPIE Medical Imaging2010; San Diego, CA.

19. Acciavatti RJ, Maidment ADA. Optimization of Continuous Tube Motion and Step-and-Shoot Motion in Digital Breast Tomosynthesis Systems with Patient Motion. Paper presented at: SPIE Medical Imaging2012; San Diego, CA.

20. Chan H-P, Goodsitt MM, Helvie MA, et al. Digital Breast Tomosynthesis: Observer Performance of Clustered Microcalcification Detection on Breast Phantom Images Acquired with an Experimental System Using Variable Scan Angles, Angular Increments, and Number of Projections Views. *Radiology.* 2014;273(3):675-685.

21. Pokrajac DD, Maidment ADA, Bakic PR. Optimized generation of high resolution breast anthropomorphic software phantoms. *Medical Physics.* 2012;39(4):2290-2302.

22. Chui JH, Pokrajac DD, Maidment ADA, Bakic PR. Towards Breast Anatomy Simulation Using GPUs. *Lecture Notes in Computer Science.* 2012;7361:506-513.

23. Bakic PR, Pokrajac DD, Caro RD, Maidment ADA. Realistic Simulation of Breast Tissue Microstructure in Software Anthropomorphic Phantoms. *Lecture Notes in Computer Science.* 2014;8539:348-355.

Development and Evaluation of a Spatial Resolution Metric for Digital Breast Tomosynthesis

Trevor L. Vent, Raymond J. Acciavatti, and Andrew D. A. Maidment

***Abstract*—An in-plane resolution metric is presented for tomosynthesis. The radial fast Fourier transform (RFFT) metric evaluates resolution of different imaging techniques for digital breast tomosynthesis (DBT). This metric was developed to investigate alternative acquisition geometries for a next generation tomosynthesis (NGT) prototype. Two acquisition geometries and two orientations are compared to present the Radial FFT metric. The first geometry mimics a conventional DBT geometry. The second geometry is a T-shaped x-ray source trajectory. The Radial FFT metric uses a star pattern input to plot modulation in the frequency domain. The RFFT graph portrays all frequencies that are present in the image reconstruction and enhances detail that is not observed by visual inspection. In addition to the fundamental input frequency of the star pattern, the RFFT graph shows spectral leakage, square wave harmonics, and residual noise. The in-plane CTF of a is obtained using the RFFT graph. The CTF is analogous to the modulation transfer function (MTF), but it is not normalized to the zero spatial frequency and accounts for aliased signals. The results verify that super-resolution is present for all frequencies that are parallel to the scanning direction of conventional DBT, and that aliasing is present for frequencies aligned perpendicular to the scanning direction. The Radial FFT metric separates the fundamental-input frequency from spectral leakage, and determines the in-plane limit of spatial resolution with respect to aliased signals. The T acquisition geometry is shown to support isotropic resolution for DBT. The Radial FFT metric adequately compares resolution properties of 2D images and 3D image reconstructions for various x-ray imaging modes without suppressing aliased signals and can also be applied to magnification tomosynthesis.**

***Index Terms*—Digital breast tomosynthesis, super-resolution, spectral leakage, aliasing, modulation transfer function, contrast transfer function, radial fast Fourier transform.**

I. Introduction

CONVENTIONAL digital breast tomosynthesis (DBT) systems acquire multiple x-ray projections over a range of angles along a linear trajectory. The collection of projections for a DBT acquisition is then back-projected to create 3D image reconstructions. Whereas a tomosynthesis acquisition produces a 3D dataset, the data are most frequently read by radiologists in a 2D plane. DBT provides improved in-plane resolution and has been reported to have a clinical advantage over 2D digital mammography [1]. We have shown in previous work that DBT image reconstructions are capable of in-plane super-resolution [2]–[5]. Super-sampled image reconstructions produce reconstructed image slices that accurately represent spatial frequencies above the detector alias frequency (f_{alias}). Many methods exist that evaluate the resolution of DBT systems. One such metric is the modulation transfer function (MTF). The importance of measuring both the 3D MTF and the in-plane MTF for tomosynthesis was presented by Zhao *et al.* [6]. The metric that we introduce in this paper is an in-plane spatial-resolution metric for tomosynthesis. This metric evaluates the intrinsic resolution properties of digital x-ray systems without suppressing aliased signals in 2D images and 3D image reconstructions.

A. Resolution for Tomosynthesis

Resolution for tomosynthesis systems depends on intrinsic system properties and sampling techniques [2], [3], [5]. Superior resolution in DBT is the result of better sampling. In the Fourier domain, the sampled data for a DBT system is a collection of planes, conceptualized as a double-napped cone [7]. The double-napped cone changes shape with a change in acquisition geometry [8], [9]. An *acquisition geometry* is the collection of projection images that are used to create a 3D image reconstruction. For a 2D mammogram, the Fourier representation of the sampled data is a single plane. If we consider the Fourier domain, a double-napped cone represents better sampling than a single plane. However, DBT acquisitions are an under-sampled dataset in terms of both exposure and acquisition geometry. DBT is also referred to as limited-angle tomography and produces anisotropic resolution in image reconstructions. Super-resolution is achieved for frequencies that are aligned parallel to the x-ray source motion, but not achieved for frequencies that are aligned perpendicular to the x-ray source motion [3].

Support was provided by grant W81XWH-18-1-0082 from the Department of Defense Breast Cancer Research Program. The content is solely the responsibility of the authors and does not necessarily represent the official views of the funding agency.

T. L. Vent is with the Department of Bioengineering, University of Pennsylvania, Philadelphia, PA 19104 (email: tvent@seas.upenn.edu).

R. J. Acciavatti is with the Department of Radiology, University of Pennsylvania, Philadelphia, PA 19104 USA (email: Raymond.Acciavatti@uphs.upenn.edu).

A. D. A. Maidment is with the Department of Radiology and the Department of Bioengineering, University of Pennsylvania, Philadelphia, PA 19104 USA (email: Andrew.Maidment@uphs.upenn.edu).

B. Alias Frequency in Digital Detectors and Sampling

Digital imaging systems have an alias frequency above which objects are not resolved. The alias frequency, f_{alias}, of an imaging system is given by the first zero of the Fourier transform of the detector's aperture (d_{el}). The Fourier transform of an aperture is, sinc(d_{el}), and the alias frequency is given by:

$$f_{alias} = \frac{0.5}{d_{el}} \tag{1}$$

Aliasing is predominant in 2D images for any frequencies above f_{alias}. The prominence of aliasing in 3D image reconstructions depends on the acquisition geometry and the orientation of the input object. For a conventional DBT acquisition geometry, aliasing is present and manifested as Moiré patterns for frequencies that are aligned perpendicular to x-ray source motion. Aliasing dominates the input signal of these reconstructions because the magnitude of the spectral-leakage modulation is greater than the magnitude of the input-frequency modulation in the Fourier domain.

Super-resolution is achieved in the direction of source motion because each object is projected onto sufficiently distinct positions of the detector across all projections. The back-projection of these images can then be super-sampled such that the reconstructed image grid is finer than the detector element size [2], [10]. An MTF calculation for any x-ray system shows modulation for frequencies higher than f_{alias}. This is evidence that super-resolution *is* achievable with the proper sampling technique. However, the MTF will *not* show that the frequencies above f_{alias} are dominated by aliasing.

C. Resolution Metrics

The current metrics that evaluate resolution for DBT systems have remained unchanged since before the advent of clinical DBT. Whereas these metrics adequately evaluate the components of an imaging system, they are not adequately specific in terms of system design and implementation. Various DBT systems are currently available for screening mammography, and each system is constructed with a distinct mechanical design and geometric configuration. Additionally, these systems vary in terms of the DBT acquisition technique: number of projections, angular range, and exposure settings [x-ray tube charge (mAs) and energy (kV)]. The variation in the mechanical design and acquisition techniques of these systems necessitates a metric that can distinguish aliasing and establish a standard for comparing the complexities of these systems.

IEC 62220-1 outlines a method to measure the MTF of x-ray systems using the slanted edge. AAPM TG-245 proposes an alternative approach by using a tilted tungsten wire. Both of these methods suppress aliasing through super-sampling. We are seeking a resolution metric that will reveal aliasing.

The radial fast-Fourier transform (RFFT) metric and the contrast transfer function (CTF) that are presented in this paper assesses high-resolution image quality of DBT systems without suppressing relevant information, like aliasing or other artifacts, through super-sampling. The RFFT metric discerns aliasing by identifying signals of spectral leakage separate from the fundamental input frequencies in the Fourier domain. An example of aliasing sensitivity is the evidence of spectral leakage in the oscillatory behavior of the CTF graph in Fig. 1. The CTF is analogous to the MTF but is not normalized to the zero, spatial frequency. The MTF calculation for this system was measured using the slanted edge method described by Fujita [11], [12]. The slanted-edge method suppresses spectral leakage through super-sampling and undermines the capability of the MTF to discern aliasing.

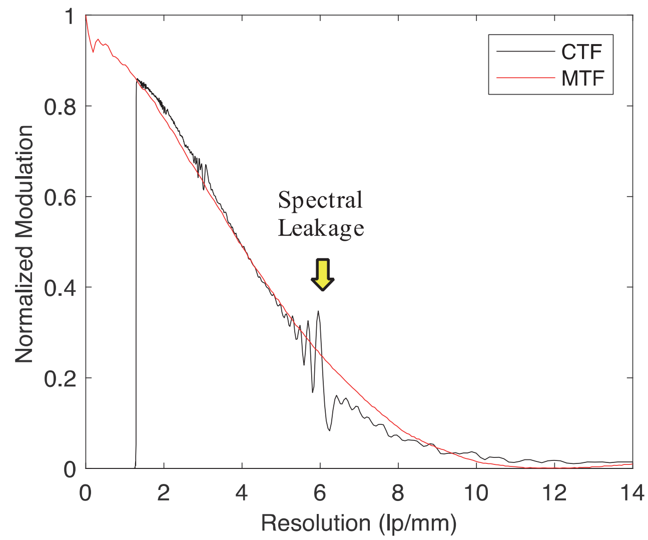

Fig. 1. The normalized modulation of the CTF and MTF are plotted as a function of spatial resolution. The distinction between the MTF and CTF is the characteristic oscillatory behavior of the CTF plot. These oscillations are a manifestation of spectral leakage.

II. Materials

A. Next-generation tomosynthesis prototype

The Radial FFT metric was derived from characterizing our prototype DBT system. The NGT system consists of a gantry that can elevate and rotate an attached C-arm. The C-arm consists of the following components: XM-1016T x-ray tube (IAE, Milan, Italy), AXS-2430 detector (Analogic Canada Corporation, Montreal, Quebec), and a breast support that acts dually as a magnification stand. The magnification stand is used to investigate magnification digital breast tomosynthesis (MDBT) [5]. The detector has an 85μm detector element size (d_{el}) and can resolve up to 5.88 line pairs per millimeter (lp/mm) in 2D. A PMX x-ray generator (Spellman, Hauppauge, NY) and a Parker automation controller (Parker-Hannifin 6K8, Rohnert Park, CA) control the x-ray tube and detector movements. The components of the system are synchronized using custom software (Real Time Tomography, Villanova, PA) and an Arduino microcontroller (Arduino MEGA 2560 Rev3) [13]. The NGT system configuration is shown in Fig. 2.

The NGT prototype is used to investigate alternative acquisition geometries for DBT. Whereas a conventional DBT system scans linearly in one dimension, the NGT prototype positions the x-ray source at various locations within the source plane to execute an acquisition geometry. This sampling technique enhances the sampled frequencies in the Fourier domain [9]. The source-to-image distance (SID) for the NGT system is 652 mm. The range of motion for the x-ray tube of is

±90 mm in x (R_x) and 180 mm in y (R_y). Given these ranges, the NGT prototype is capable of investigating myriad acquisition geometries [14].

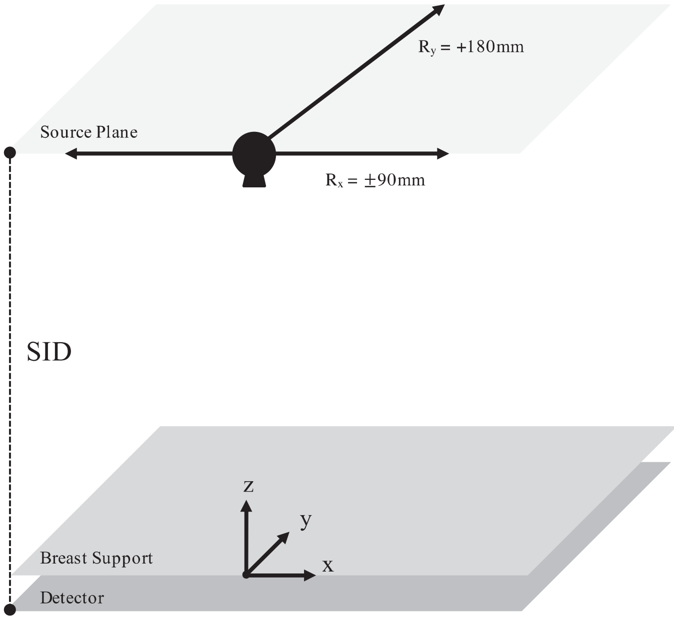

Fig. 2. The coordinate axes and the design geometry are defined for the NGT prototype. The x-y-z coordinate system defines the origin of the NGT system. It is located at the center of the of the detector along the chest-wall edge relative to the patient. The x-axis is parallel to the chest wall and is also parallel to a conventional DBT scanning motion.

The Radial FFT metric provides a platform for comparing the quality of one NGT acquisition geometry to another in terms of spatial resolution, modulation contrast, and aliasing. This metric is introduced with results from two typical acquisition geometries of the NGT system (Fig. 3). The first is the conventional acquisition geometry that mimics the tomosynthesis acquisition of a clinical DBT system (Selenia Dimensions, Hologic, Marlborough, MA). The second geometry is a T-shaped acquisition geometry that introduces x-ray source motion in the **y**-direction within the source plane [4], [5], [15]. The NGT system also supports z-detector motion. However, z-detector motion is beyond the scope of this paper, and the results do not include geometries with z-detector motion.

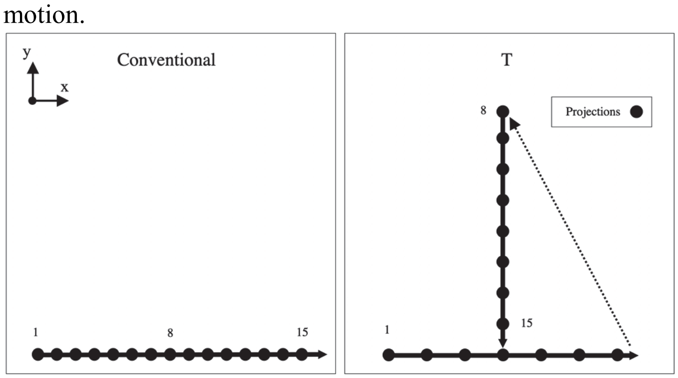

Fig. 3. Two NGT acquisition geometries shown in the source plane. The conventional geometry consists of 15 projections spaced equidistantly in the x-direction. The T geometry is also 15 projections; 7 are in the x-direction and 8 are in the y-direction.

B. *Star Pattern Test Object*

To obtain the CTF, we use the frequencies contained in one quadrant of a star-pattern test object as the fundamental input frequency. The star pattern consists of four quadrants of 29 alternating lead and acrylic sectors at 1° spacings. The angular range of each quadrant is 29° (model 07-542-1000). The sharpness of the edge on the lead foil is a square-wave input similar to a bar-pattern test object. The Fourier transform of a square-wave of length L is a series of sinusoidal waves:

$$\mathcal{F}(t) = \frac{4}{\pi}\sum_{m=1}^{\infty}\frac{-1^{m-1}}{2m-1}\mathrm{Cos}\left(\frac{2\pi m t}{L}\right) \tag{2}$$

The fundamental frequency (m=1) is the most accurate representation of the star pattern input frequencies and is the dominant frequency in an image reconstruction. The finite size of the focal spot and the diffraction of the xrays blur the signal of the high frequencies, producing a sinusoidal signal (Fig. 4). As predicted by Coltman [16], square-wave harmonics are also present in image reconstructions at lower spatial frequencies of the star pattern. This is expected because the intensity profiles of the lower frequencies in a star pattern image are more square-like than the intensity profiles of higher frequencies; there is a lack of blurring at the lower spatial resolutions of the star pattern (1.27-2.5 lp/mm).

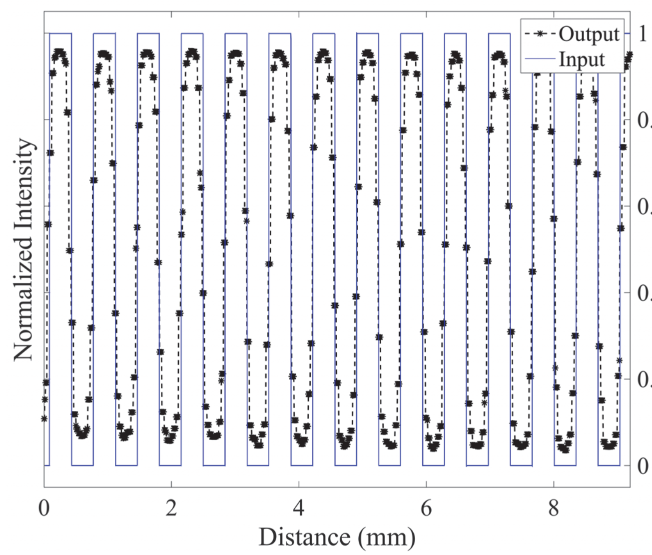

Fig. 4. The sine-wave response (Output) of the square wave (Input) at a resolution of 1.4 lp/mm in the image reconstruction of the star pattern [16]. The output also illustrates the variance of different frequencies sampled across each point of the waveform.

III. Method

A. *Image acquisition*

Images of the star pattern were acquired on the NGT prototype using various techniques. The star pattern was positioned at the origin with the quadrant centers aligned parallel to the detector grid. The two acquisition geometries that are described above were used to obtain projection images that are used for the 3D image reconstructions. All contact mode acquisitions were performed using a technique of 28 kVp and 1.5 mAs per projection with a 0.5 mm aluminum filter. A magnification tomosynthesis image was acquired using the conventional acquisition geometry for the NGT system. The projection images were acquired with 28 kVp and a total of 4.5 mAs with the x-ray tube's small focal spot size (0.1 mm).

Star pattern projection images were reconstructed using commercial reconstruction software (Real Time Tomography: Villanova, PA). This reconstruction software is capable of any multiplanar reconstruction [sagittal (y-z), coronal (x-z), transverse (x-y), and oblique (arbitrary magnitudes of x, y, and z)]. The results in IV include images that are reconstructed conventionally, with slices parallel to the breast support (x-y plane). The software can produce super-sampled reconstructions with grids up to 10 times the detector element size. The reconstruction grid for all contact setting image reconstruction data is 37μm (2.3 times the detector element size of the detector). This factor includes the super-sampled back projection at 2.2 times the detector element size and the geometric magnification correction of 1.05 in the contact mode of the NGT system. The central 2D projection image was used for the 2D analysis below.

B. *RFFT Metric*

The RFFT is calculated using one quadrant of the star pattern as an input to create a graph of modulation in the frequency domain. This graph is referred to as the radial fast Fourier transform (RFFT) graph. The RFFT graph is the normalized modulation of all frequencies contained within a quadrant of the star pattern. It emphasizes details about the image reconstruction that are imperceptible to the human eye.

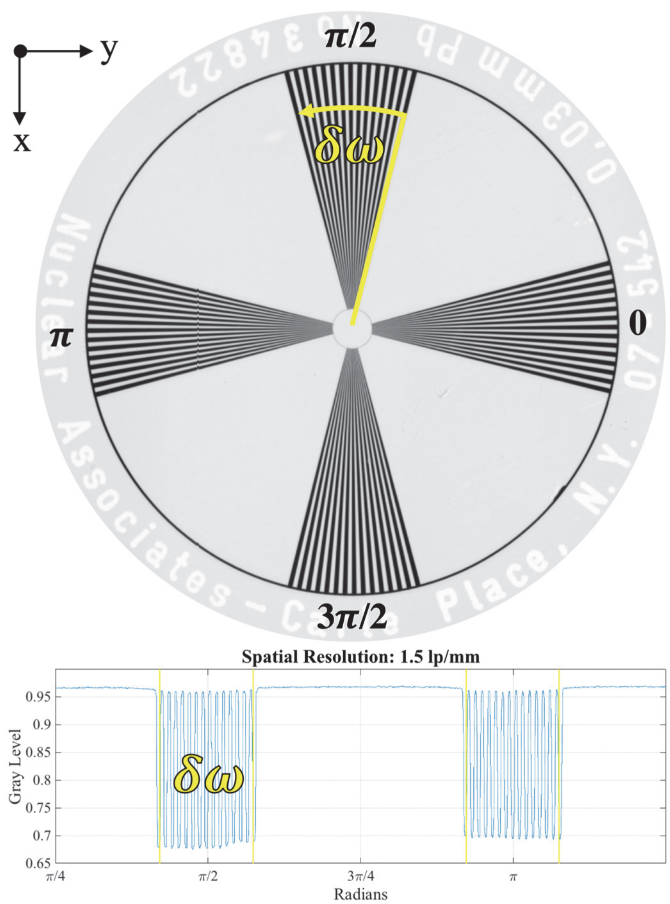

Fig. 5. The profile extraction of the vertical quadrant for the y-direction frequencies at a resolution of 1.5 lp/mm. $\delta\omega$ represents the angular range of the profile extraction. The quadrant is determined by the angle of the unit circle in radians. Note that the frequencies parallel to y are located at odd-valued integer multiples of $\pi/2$ in the image and conversely all frequencies parallel to x are located at integer multiples of π.

From the plane of the star pattern in the reconstruction, the center of the star pattern is determined. Then, starting at the inner ring (20 lp/mm), the plot profile is extracted radially for the quadrant of interest ($\delta\omega$). The quadrants are named by the angle in radians relative to the center (0, $\pi/2$, π, and $3\pi/2$). Each quadrant has an angular range of 29° (Fig. 5). The 1D fast Fourier transform (FFT) is computed for this profile. (The 1D FFT of the profile computes the modulation of each frequency–aliased or not–within the quadrant at the given radius.) The radius is then incremented by one pixel and the process is repeated to the outer ring of the star pattern (1.27 lp/mm). An example of one FFT calculation at a given radius is shown in Fig. 6.

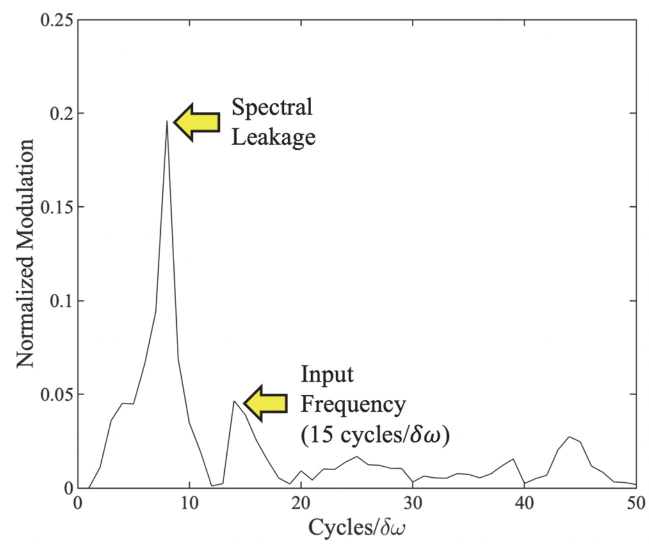

Fig. 6. Example of the 1D FFT at a radius of 8 lp/mm. The modulation of the aliased signal is well above that of the input frequency for this example.

The waveform of each quadrant is sampled using Fourier interpolation with 1,650 increments at each radius. The angle at which the frequencies are oriented across the reconstruction grid varies from one edge of the quadrant to the other. When the star pattern is oriented such that the centers of the quadrants are aligned parallel to the reconstruction grid, the largest angle of orientation for the frequencies is 14.5° (relative to the reconstruction grid). For comparison, the MTF should be computed using an edge that is aligned at 2.5° (relative to the detector grid) with an ROI of at least 10 cm to achieve sufficient sampling [11], [12], [17]. The radial sampling of the star pattern has a similar effect and is observed as the various different vertical positions of the star points in Fig. 4.

The maximum modulation of the input frequency is normalized to the value of the MTF at 1.27 lp/mm. The normalized modulation of all 1D FFT profiles is plotted as a function of resolution (lp/mm) and period (cycles/$\delta\omega$) to create the RFFT graph (Fig. 7). The most prominent peaks in the plot are the signals of the fundamental input frequency at each radius. The input frequency is 15 cycles per quadrant (cycles/$\delta\omega$). Peaks of spectral leakage are also prominent at various other cycles. They create a spine of frequencies that intersects the fundamental frequency at the f_{alias} of the detector. These peaks are indicative of aliasing. When present with a greater magnitude than the input frequencies, aliased signals dominate image reconstructions. The least prominent peaks in the plot create a spine that occurs at 45 cycles/$\delta\omega$. This is modulation for a square wave harmonic of the star pattern (m=3). The input of the star pattern would produce an exact square wave if there were no intrinsic blurring. The waveform is sinusoidal in the plot profile but maintains square-wave characteristics for resolutions lower than 2.5 lp/mm. This follows the findings of Coltman for the sine-wave response function given a square-wave input [16]. Noise from the image reconstruction may contribute to the rough texture observed in the other areas of the plot.

The RFFT graph produces a super-sampled Fourier transform of a quadrant in the star pattern. The CTF is the normalized modulation of the fundamental input frequency, obtained from the RFFT graph, as a function of resolution. The CTF is commensurate to the square-wave response function that is calculated from the sine-wave response function [16]. The CTF is used to discern the aliasing-dependent limit of spatial resolution (LSR). In contrast to the MTF calculation, the Radial FFT metric identifies aliasing as spectral leakage in image reconstructions.

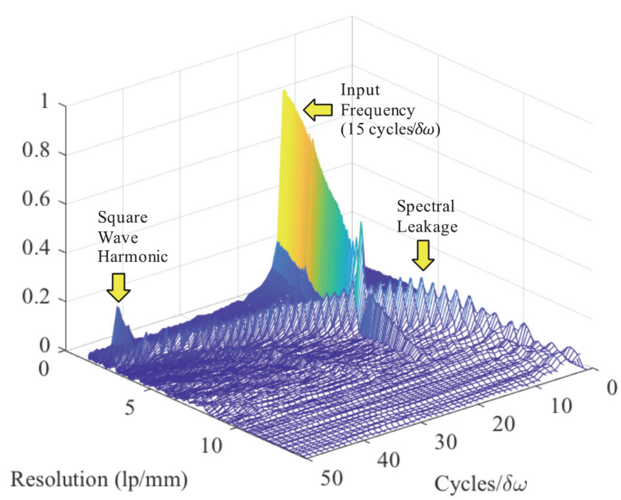

Fig. 7. An example of the Radial FFT graph for y-direction frequencies of a star pattern. The spine of the fundamental frequency occurs at a period of 15 Cycles/$\delta\omega$. The spine of spectral leakage intersects the fundamental frequency at a resolution of 5.88 lp/mm (f_{alias}). The spine of the square wave harmonic for m=3 occurs at 45 cycles/$\delta\omega$.

IV. Results and Discussion

Various analyses are presented for the Radial FFT metric. The MTF is used as the standard of comparison to the CTF for all analyses. (IV.A) The Radial FFT metric compared the two previously defined acquisition geometries of the NGT system. (IV.B) Super-sampled 3D image reconstructions were compared to 2D images. (IV.C) The Radial FFT metric was applied to MDBT image reconstructions and compared to the 2D MTF at the same magnification. The LSR is used to quantify performance of the different approaches. All image reconstructions were obtained without any post-processing.

A. Comparing acquisition geometries using the NGT system

The conventional DBT acquisition geometry is a series of 15 x-ray projections. The source moves parallel to the chest wall edge at a set SID. For the contact imaging setting of the NGT system, the location of breast support relative to the detector in z creates a geometric magnification of 1.05. For this geometry, super-resolution is observed in the x-direction of image reconstructions [Fig. 8(c)], whereas the y-direction shows Moiré patterns [Fig. 9(c)]. These are contrasting results given by the Radial FFT metric; ostensibly however, the system has the same pre-sampled MTF in both directions. This is significant because resolution for conventional DBT is anisotropic, but an MTF calculation does not reflect this result. The Radial FFT metric shows obvious differences in frequencies that are aligned parallel (x) and perpendicular (y) to the x-ray source motion for the conventional DBT acquisition geometry.

The results for the conventional acquisition geometry are represented in [XXX] and [XXX] for the 0- and $\pi/2$-radian quadrants of the star pattern respectively. For figures 8, 9, 11, and 12: (a) is the RFFT graph, (b) is a plot of the CTF and corresponding MTF, and (c) are cropped images of the in-plane reconstructions for the quadrants being analyzed and the blue arcs indicate the LSR.

1) Conventional acquisition geometry

The x-direction frequencies (0-radian quadrant) of the conventional acquisition geometry show evidence of super-resolution and residual aliasing artifacts [Fig. 8(a-b)]. It is important to note that for this geometry and orientation, the frequencies are aligned parallel to the x-ray source motion.

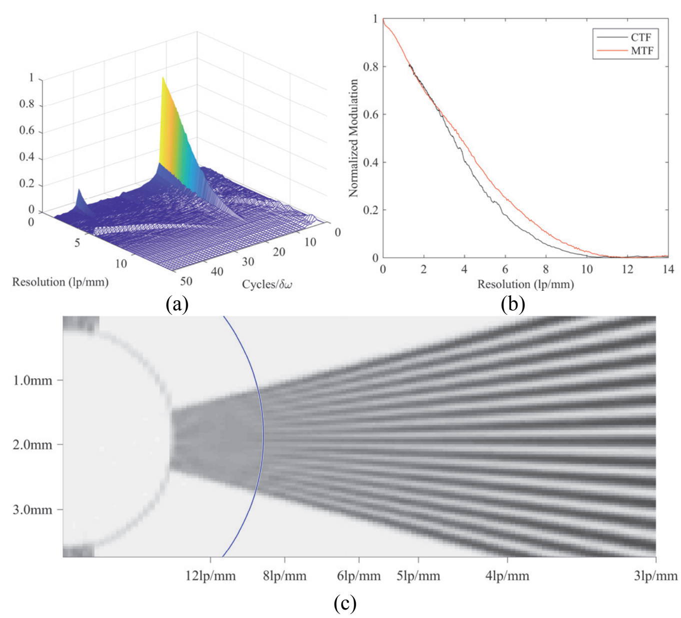

Fig. 8. Results for the conventional geometry x-direction frequencies in the 0-radian quadrant of the star pattern. The RFFT graph (a), CTF plot (b), and resultant image with the LSR designated by the blue arc (c) are shown. The fundamental frequency and square wave harmonic are the only dominant signals in (a). The CTF curve significantly matches the system's MTF for this same orientation (b). The LSR is evident in the CTF plot near 9 lp/mm where modulation is 2%. The Radial FFT metric appropriately discerns the LSR for the image reconstruction at 9 lp/mm (c).

The RFFT shows the spine of the fundamental input frequency, the spine of the square-wave harmonic, and spines of residual spectral leakage. The prominence of spectral leakage is diminished due to the sampling in x and results in super-resolution in the image reconstruction. The fundamental frequency is essentially the only frequency with significant modulation. As a result, the image reconstruction accurately portrays the fundamental input frequency past the alias frequency of the detector.

The CTF shows modulation for the fundamental input frequency. The CTF is normalized at 1.27 lp/mm using the modulation of the MTF at the same resolution. The CTF shows residual aliasing artifacts near 6 lp/mm and modulation up to 10 lp/mm which is discerned to be the LSR. The image in Fig. 8(c) shows the x-direction frequencies of the reconstructed star pattern. The blue line indicates the LSR to be near 9 lp/mm.

The y-direction frequencies ($\pi/2$-radian quadrant) are aligned perpendicular to x-ray source motion for this geometry. Aliasing is present in these image reconstructions. The results for this orientation are represented in Fig. 9. The RFFT graph [Fig. 9 (a)] for this orientation shows the same spines of the fundamental frequency and the square-wave harmonic as before. In contrast to the x-direction frequencies [XXX], the spectral leakage is prominent for this orientation. The spine of spectral leakage has higher modulation where it intersects the spine of the fundamental frequency. The CTF [Fig. 9(b)] shows characteristic oscillatory behavior at the resolution where the spine of the spectral leakage intersects the spine of the fundamental input frequency. This intersection occurs at f_{alias}, and is the LSR for the y-direction frequencies due to aliasing.

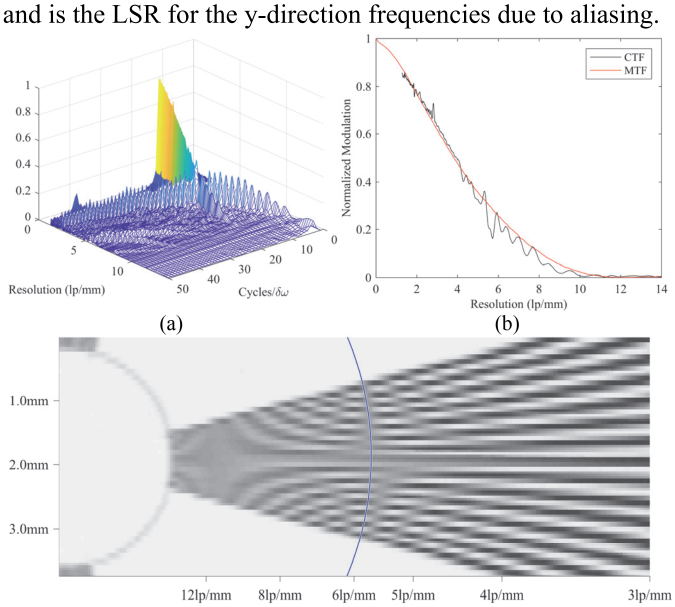

Fig. 9. Results for the conventional geometry y-direction frequencies of $\pi/2$-radian quadrant. The RFFT graph (a) is similar to Fig. 8 (a), but shows significant spectral leakage. The spectral leakage intersects the spine of the fundamental frequency at 6lp/mm. This result is reflected in (B). The CTF is normalized to the same modulation of the MTF for a resolution of at the outer ring of the star pattern. Image (c) shows the limit of spatial resolution as determined by the Radial FFT metric near 6 lp/mm.

The image shows Moiré patterns for frequencies above and below f_{alias}. The oscillatory behavior in the CTF and the Moiré patterns in the image reconstructions repeat according to the detector's pixels, described by (3):

$$\mathrm{M}(n) = \frac{f_{alias}}{n} \tag{3}$$

We demonstrate the repetition of the Moiré pattern and how it corresponds to the RFFT graph in Fig. 10 (above) by viewing the RFFT graph from an aerial perspective next to its corresponding quadrant in the image reconstruction. This figure portrays the fundamental frequency vertically from top to bottom. The spectral leakage appears as the diagonal ripples that intersect the fundamental frequency at three locations. This first occurs near 6 lp/mm, which is 1/2 cycles per pixel (n=1). The spectral leakage repeats at 3 lp/mm (1/4 cycles per pixel, n=2) and at 1.5 lp/mm (1/6 cycles per pixel, n=3).

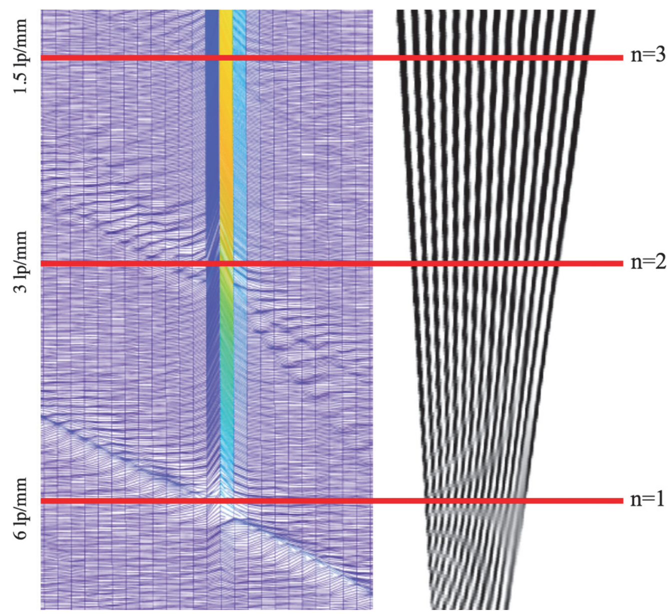

Fig. 10. Depiction of the RFFT graph from an aerial perspective alongside the corresponding star pattern quadrant with repeating Moiré patterns. The integer value n corresponds to (3). The same behavior is observed in Fig. 1.

2) *T-shape geometry*

The other geometry presented is a T-shaped acquisition geometry. This geometry investigates x-ray source motion in the y-direction. The x-ray source acquires seven projections in the x-direction, then eight projections in the y-direction. The trajectory of the x-ray source is nearly equivalent in both directions and resolution was observed to be isotropic for the x- and y-direction frequencies. The results for both of these frequencies are summarized in Fig. 11 and Fig. 12.

The x-direction frequencies of the T-shaped geometry show similar results to those of the conventional geometry (Fig. 12). The spectral leakage is prominent for the x-direction frequencies of this geometry, whereas for the conventional geometry [Fig. 8(a)], spectral leakage was not prominent. The spectral leakage is less prominent than it is in the RFFT graph of the y-direction frequencies for the conventional geometry [Fig. 9(a)]. All other plot features discussed in the RFFT graphs of Fig. 8 and Fig. 9 are similarly observed in the RFFT graph for the T-shaped acquisition geometry.

The CTF for this orientation shows the characteristic oscillatory behavior like the y-direction frequencies of the conventional geometry, but the oscillations are less prominent.

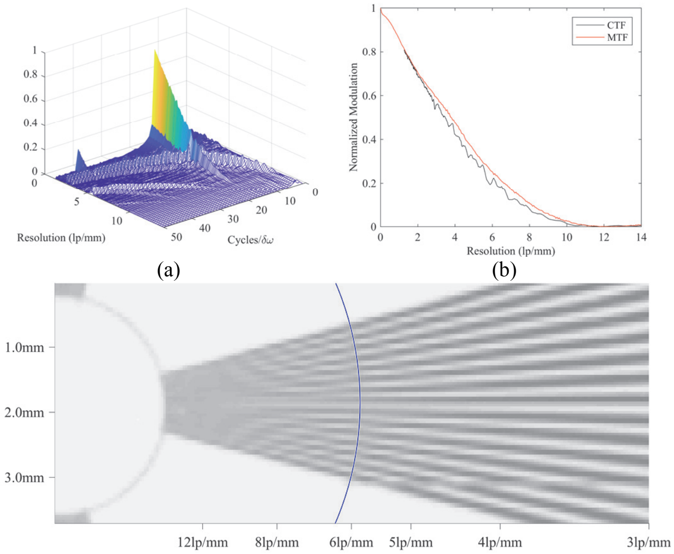

Fig. 11. Results for the T-shape acquisition geometry of the 0-radian quadrant in the star pattern. The RFFT graph (a) shows spectral leakage. The spectral leakage intersects the spine of the fundamental frequency near 6 lp/mm. This result is reflected in (b) as oscillatory behavior. Image (c) shows the LSR to be near 6 lp/mm due to aliasing.

As a result of introducing spectral leakage to the x-direction frequencies, the LSR has been reduced to f_{alias} (6 lp/mm) for the x-direction frequencies. This is shown in the quadrant image of Fig. 11(c).

The y-direction frequencies for the T-shaped geometry are similar to the y-direction frequencies of the conventional geometry. The results for the y-direction frequencies are summarized in Fig. 12. They are compared against both the y-direction frequencies of the conventional geometry and the x-direction frequencies of the T-shaped geometry.

The RFFT graph shows the same features as the conventional geometry. The spine of the spectral leakage is less pronounced for the y-direction frequencies of the T-shaped geometry [Fig. 12(a)] than it is for the y-direction frequencies of the conventional geometry [Fig. 9(a)]. As a result, the Moiré patterns that arise from aliasing appear to be less significant in the image reconstruction [Fig. 12(c)]. The Radial FFT metric was able to identify the T-shaped geometry as superior to the conventional geometry for the y-direction frequencies.

For the T acquisition geometry the results of the x and y-direction frequencies are similar. This is significant for two reasons: First, it shows that the T-shaped acquisition geometry supports isotropic resolution. Second, it verifies that the Radial FFT metric can quantitatively compare the resolution properties of one acquisition geometry to the resolution properties of another acquisition geometry without suppressing aliased signals.

The two geometries and two frequency orientations were compared in terms of LSR and aliasing. The conventional geometry for the x-direction frequencies supports the highest LSR. Due to aliasing, the y-direction frequencies of the

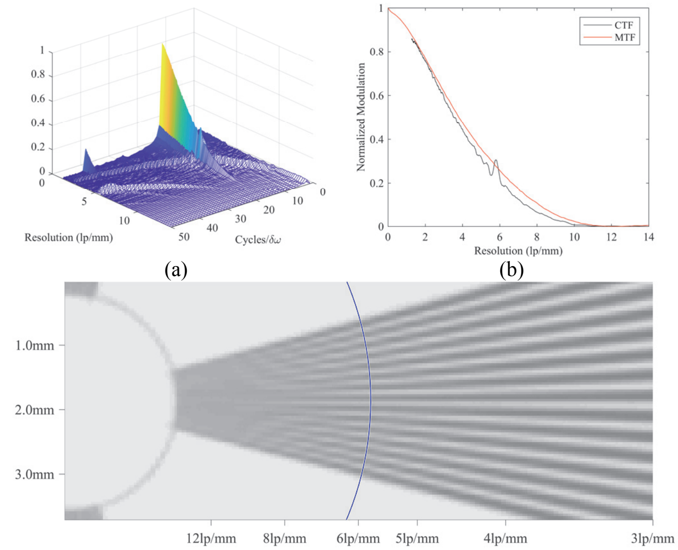

Fig. 12. Results for the T-shape geometry y-direction frequencies of the $\pi/2$-radian quadrant in the star pattern. The results of this orientation are nearly identical to the x-direction orientation.

conventional geometry and both frequencies of the T geometry have an LSR at 5.88 lp/mm. However, modulation is improved for the T acquisition geometry in both directions and aliasing is not as dominant as the as the aliasing for the conventional acquisition geometry. The Radial FFT metric correctly identified the existence of aliasing for multiple orientations and accounted for aliasing in determining the LSR for each acquisition geometry.

B. *Comparing 3D image reconstructions and 2D images*

The Radial FFT metric was applied to a 2D image of the star pattern that was acquired with the x-ray source located at the origin of the source plane in the contact mode setting. The 2D projection has a magnification correction of 1.05 corresponding to a d_{el} of 0.081mm in the plane of the star pattern located on the breast support. The Radial FFT metric can assess the performance of 2D images in the same manner as in-plane 3D image reconstructions.

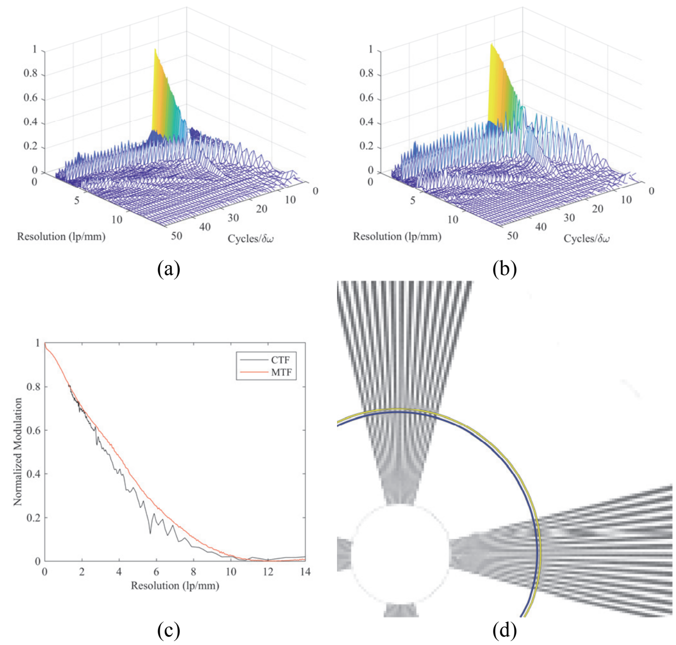

Fig. 13: The Radial FFT metric applied to a 2D image. The 0 (a) and $\pi/2$ (b) quadrants' RFFT graphs are shown to illustrate the capability of the Radial FFT metric to evaluate multiple orientations simultaneously for 2D. The increase in the prominence of spectral leakage between (a) and (b) is likely the result of anisometric focal spot size. One example of the CTF plot is shown for the 0-radian quadrant (c). The LSR is correctly discerned for the 2D image (d) where the spine of spectral leakage intersects the fundamental input frequencies at the alias frequency of the detector.

C. *Radial FFT metric applied to magnification tomosynthesis*

The MTF was performed using the NGT prototype in 2D at a magnification of 1.5. This required use of the x-ray tube's small focal spot. Once the MTF was calculated at this magnification, a tomosynthesis acquisition of the star pattern at the same magnification was performed using the conventional acquisition geometry. The magnified projection images were reconstructed using the same factor of super-sampling as all previous reconstructions ($2.2 \times d_{el}$). With the magnification of 1.5, the in-plane pixel size was determined to be 25.8μm. The 0- and $\pi/2$-radian quadrants were analyzed for this image reconstruction (Fig. 14). The CTF plots [Fig. 14(a) and (b)] match the MTF and discern the LSR. The RFFT graphs [Fig. 14(c) and (d)] show that the location of the spectral leakage spine increases along the resolution axis by a factor of the magnification. The spectral leakage is present but reduced with an increase in magnification. The quadrant images indicate the LSR that was determined using the Radial FFT metric.

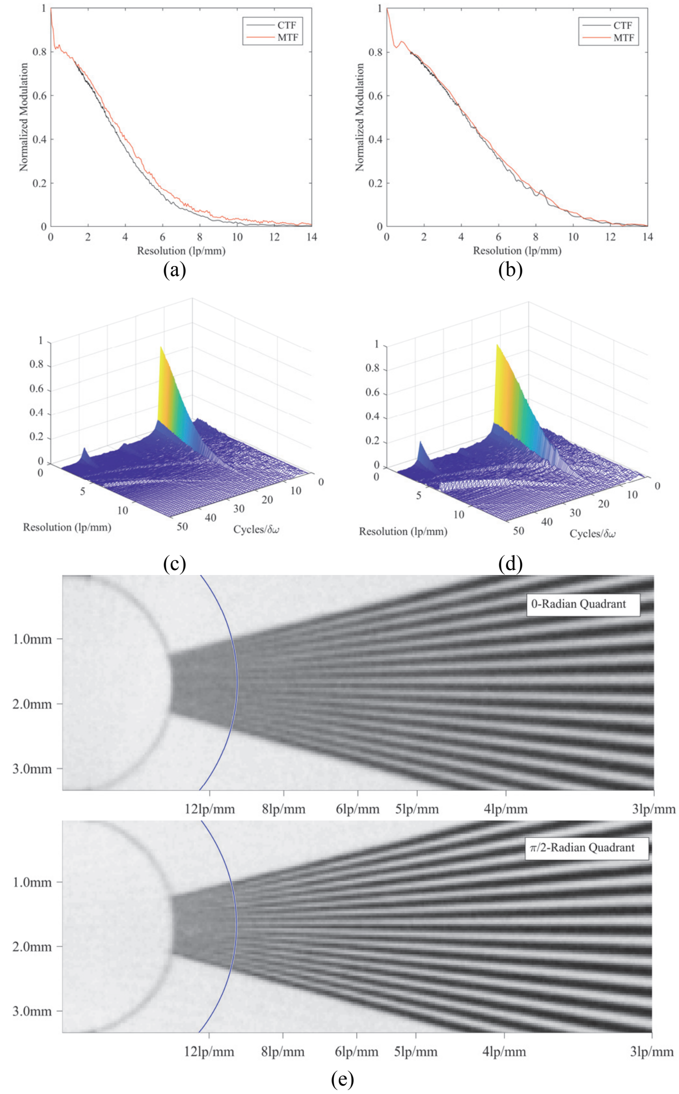

Fig. 14: The Radial FFT metric applied to an MDBT image. The CTF plots are shown for the 0-radian quadrant (a) and the $\pi/2$-radian quadrant (b). The 0-radian (c) and $\pi/2$-radian (d) quadrant RFFT graphs illustrate the diminishment of spectral leakage. The LSR increases with an increase in magnification, shown in the image of each quadrant (e).

V. Conclusion

In this work, we demonstrate the Radial FFT metric using two geometries and two orientations. The Radial FFT metric successfully compared resolution properties of all conditions. It appropriately separates the frequencies of spectral leakage from fundamental input frequencies in 2D images and 3D image reconstructions. The Radial FFT metric produces the CTF of an in-plane image reconstruction without suppressing spectral leakage through super-sampling. The CTF is a more detailed representation of in-plane resolution properties and imaging artifacts for tomosynthesis than the corresponding MTF. The Radial FFT metric will be used to evaluate resolution properties for all acquisition geometries of the NGT prototype. The tools and instructions for this metric were created using MATLAB, and are made available online at: [].

REFERENCES

[1] E. F. Conant, "Clinical Implementation of Digital Breast Tomosynthesis," Radiol. Clin. North Am., vol. 52, no. 3, pp. 499–518, 2014.

[2] R. J. Acciavatti and A. D. A. Maidment, "Observation of super-resolution in digital breast tomosynthesis," Med. Phys., vol. 39, no. 12, pp. 7518–7539, 2012.

[3] T. L. Vent, R. J. Acciavatti, Y. J. Kwon, and A. D. A. Maidment, "Quantification of resolution in multiplanar reconstructions for digital breast tomosynthesis," in Medical Imaging 2016: Physics of Medical Imaging, 2016, vol. 9783, p. 978303.

[4] C. J. Choi, T. L. Vent, A. D. A. Maidment, and R. J. Acciavatti, "Geometric calibration for a next-generation digital breast tomosynthesis system using virtual line segments," Med. Imaging 2018 Phys. Med. Imaging, no. March, p. 12, 2018.

[5] T. D. Maidment, T. L. Vent, W. S. Ferris, D. E. Wurtele, R. J. Acciavatti, and A. D. A. Maidment, "Comparing the imaging performance of computed super resolution and magnification tomosynthesis," in Medical Imaging 2017: Physics of Medical Imaging, 2017, vol. 10132, p. 1013222.

[6] B. Zhao and W. Zhao, "Three-dimensional linear system analysis for breast tomosynthesis," Med. Phys., vol. 35, no. 12, pp. 5219–5232, 2008.

[7] B. Zhao, J. Zhou, Y.-H. Hu, T. Mertelmeier, J. Ludwig, and W. Zhao, "Experimental validation of a three-dimensional linear system model for breast tomosynthesis.," Med. Phys., vol. 36, no. 1, pp. 240–51, 2009.

[8] R. J. Acciavatti and A. D. A. Maidment, "Oblique reconstructions in tomosynthesis. II. Super-resolution," Med. Phys., vol. 40, no. 11, pp. 1–19, 2013.

[9] T. L. Vent, B. L. Lepore, and A. D. A. Maidment, "Evaluating the imaging performance of a next-generation digital breast tomosynthesis prototype," Med. Imaging 2019 Phys. Med. Imaging, no. March, p. 19, 2019.

[10] J. Kuo, P. A. Ringer, S. G. Fallows, P. R. Bakic, A. D. A. Maidment, and S. Ng, "Dynamic reconstruction and rendering of 3D tomosynthesis images," vol. 796116, no. March 2011, p. 796116, 2011.

[11] E. Samei, M. J. Flynn, and D. A. Reimann, "A method for measuring the presampled MTF of digital radiographic systems using an edge test device A method for measuring the presampled MTF of digital radiographic systems using an edge test device a…," Med. Phys. Med. Phys, vol. 25, no. 913, pp. 102–113, 1998.

[12] H. Fujita, K. Ueda, J. Morishita, T. Fuiikawa, A. Ohtsuka, and T. Sai, "Basic imaging properties of a computed radiographic system with photostimulable phosphors," Med. Phys., vol. 16, no. 1, pp. 52–59, 1989.

[13] J. E. Eben, T. L. Vent, C. J. Choi, S. Yarrabothula, L. Chai, M. Nolan, E. Kobe, R. J. Acciavatti, and A. D. A. Maidment, "Development of a Next Generation Tomosynthesis System," in Medical Imaging 2018: Physics of Medical Imaging, 2018, p. 10573.

[14] B. Barufaldi, T. L. Vent, E. P. Wileyto, A. D. A. Maidment, and R. J. Acciavatti, "Personalization of x-ray tube motion in digital breast tomosynthesis using virtual Defrise phantoms," Med. Imaging 2019 Phys. Med. Imaging, no. March, p. 10, 2019.

[15] W. S. Ferris, T. L. Vent, T. D. Maidment, R. J. Acciavatti, D. E. Wurtele, and A. D. A. Maidment, "Geometric calibration for a next-generation digital breast tomosynthesis system," in Medical Imaging 2017: Physics of Medical Imaging, 2017, vol. 10132, p. 101324C.

[16] J. W. Coltman, "The Specification of Imaging Properties by Response to a Sine Wave Input," J. Opt. Soc. Am., vol. 44, no. 6, p. 468, 1954.

[17] S. N. Friedman and I. A. Cunningham, "Normalization of the modulation transfer function: The open-field approach," Med. Phys., vol. 35, no. 10, pp. 4443–4449, 2008.

Summary of Progress Made on Lesion Simulation in VCTs:

Several features were added to the existing Insertion C++ code used in the VCT Pipeline. Originally, only spheroids could be inserted as lesions into the pipeline. These could be used to model masses within the breast, but other geometries were needed to further model non-spherical lesions and calcifications.

The first expansion allowed for ellipsoids of parameters *a, b, c,* α, and γ to be inserted as lesions. The equation governing the ellipsoids was the following:

$$\frac{\left((y-y_0)\sin\alpha+(z-z_0)\cos\alpha\right)^2}{c^2} + \frac{\left((x-x_0)\sin\gamma+(y-y_0)\cos\gamma\cos\alpha-(z-z_0)\cos\gamma\sin\alpha\right)^2}{b^2} + \frac{\left((x-x_0)\cos\gamma-(y-y_0)\sin\gamma\cos\alpha+(z-z_0)\sin\gamma\sin\alpha\right)^2}{a^2} \leq 1 \quad (1)$$

where the ellipsoid is centered at (x_0, y_0, z_0), α is the angle of rotation in degrees in the y, z plane, γ is the angle of rotation in degrees in the x, y plane, and a, b, c are the semi-axes in the x, z, y directions respectively.

A triple for loop traversing the bounding box of the insertion was implemented, and voxels of the phantom meeting the condition in Eq. (1) were assigned a specific material, in this case Calcium. An image of a phantom containing an inserted ellipsoid is shown in Figure 1 below.

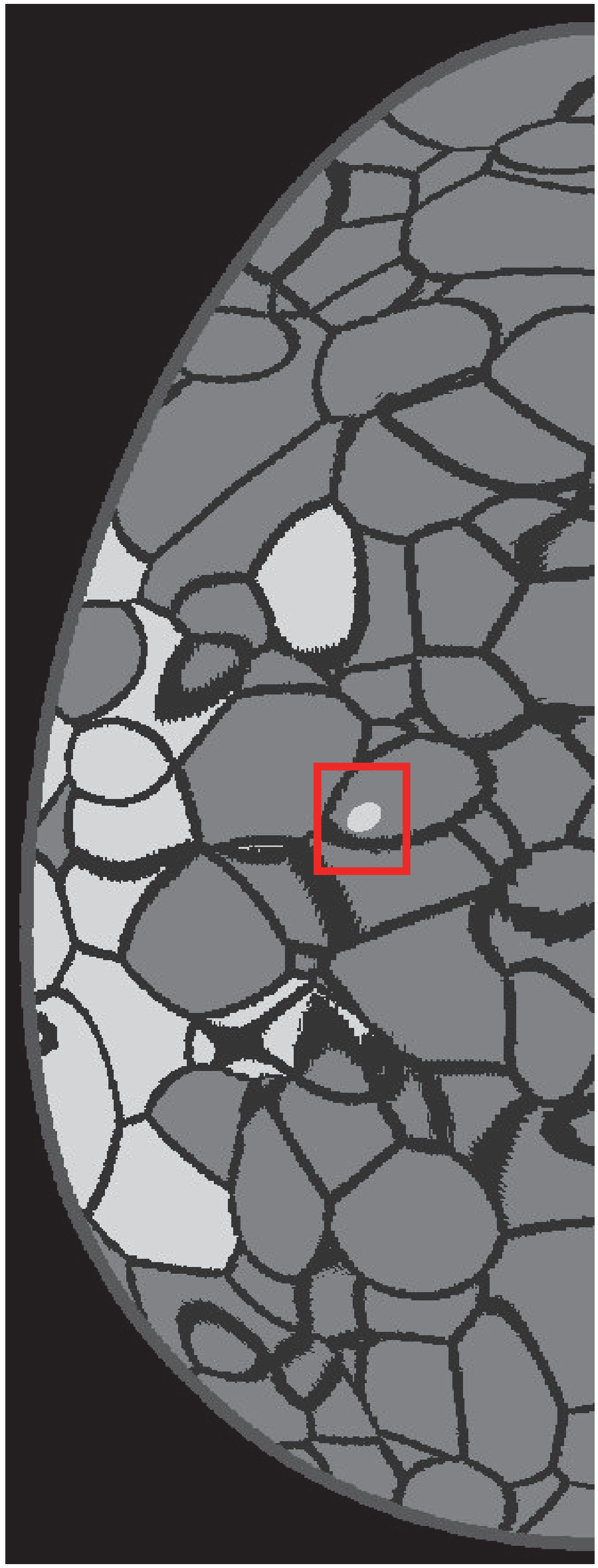

Figure 1: Ellipsoidal lesion inserted into breast phantom.

The next expansion allowed for both random, compact lesion insertion and user-defined insertions. These were handled by 2 separate array inputs. The first array was a reference array to keep track of which voxel the next voxel to be added to the lesion would be extended from. For example, if an insertion was to consist of 5 voxels, this array could consist of values ranging from 1 to 4, the value indicating where the next voxel would be inserted. The second array was a position array to dictate which face of the reference voxel the next voxel would be added to. Values in this array ranged from 1 to 6, each representing either a positive or negative movement by one voxel in the x, y or z direction within the phantom.

An example of the input process for a user-defined lesion is shown in Figure 2:

```xml
<Lesion_ID>0</Lesion_ID>

<Lesion_UID>888076.2.685169686552.20170614115425021</Lesion_UID>

<VOI_UID>003.685169686552.20170614115425151</VOI_UID>

<Is_A_Sphere>false</Is_A_Sphere>

<Is_An_Ellipsoid>false</Is_An_Ellipsoid>

<Is_Polycube>true</Is_Polycube>

<Polycube_Ref>1,2,3,4,5,6,7,8,9,10,11,12,13,14,15,16,17,18,19</Polycube_Ref>

<Polycube_Pos>1,2,3,2,1,2,3,2,1,1,1,1,1,2,3,3,3,3,3</Polycube_Pos>
```

Figure 2: XML file showing how to set up a user-defined lesion.

Given that the first reference voxel is the insertion point of the lesion, the user then enters the reference voxels in sequential order that are to be used in inserting the lesion. In the example shown in Figure 2, the numbers happen to ascend in numerical order, but this need not be the case for every lesion. The position array is then loaded to show which face of the corresponding reference voxel the next voxel will be attached to. In the case of Figure 2, the first pair of reference and position values is (1,1). This means that the next voxel in the lesion will be placed on the *first* face of the *first* voxel in the lesion. Likewise, the 4th pairing, (4,2) means that the next voxel in the lesion will be placed on the *second* face of the *fourth* voxel in the lesion.

Following this pattern, any user-defined lesion can be inserted into a phantom. A user-defined lesion using the XML file shown above is presented in Figure 3.

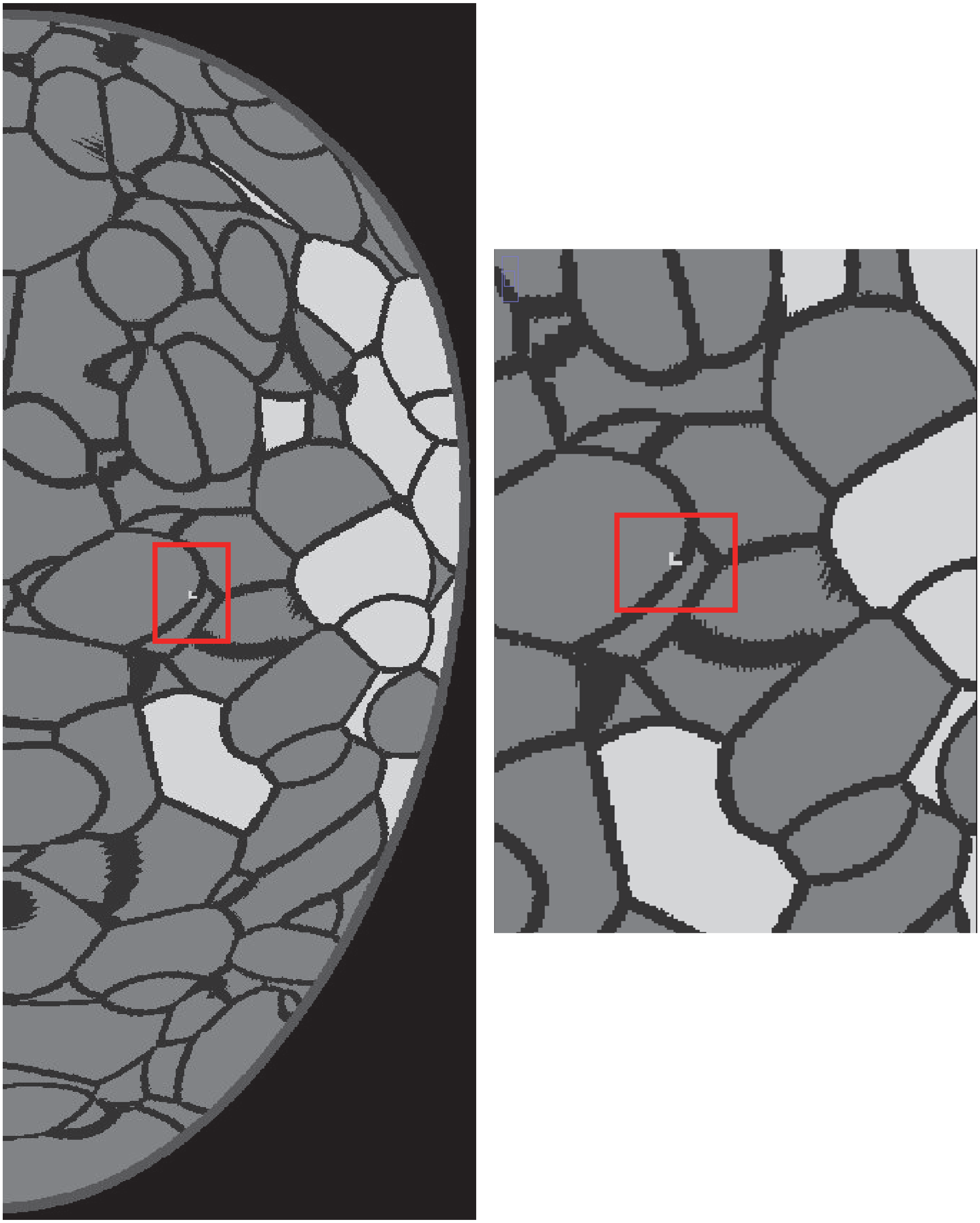

Figure 3: L-shaped lesion inserted into a phantom using the method for user-defined insertion as explained in the text.

The final expansion allowed for random, compact lesion insertion based on an input location and an input desired number of voxels in the lesion. For random insertion, an array of random reference voxels was generated, as well as an array of random positions. To ensure that only valid reference voxels were generated (i.e. ensure that you don't try to build off of the 4th voxel in a lesion when only 3 voxels currently exist in the lesion), a "for" loop was used to create a random number no larger than its position (its index + 1) in the array of reference voxels. The position array was loaded with random values between 1 and 6.

Two other checks needed to be performed to produce an acceptable random insertion. The first was compactness. We defined compactness as essentially a bounding box of the smallest possible dimensions surrounding the lesion. For example, the box surrounding a lesion from between 2 to 8 voxels did not extend more than 2 voxels in any of the $x, y,$ and z dimensions. Likewise, the box for a lesion between 9 and 27 voxels did not extend more than 3 voxels in any dimension. The formula adhered to for calculating the dimensions of this cube was given by the following:

$$\text{Each side of cube for bounding box} = \left\lceil \sqrt[3]{number\ of\ voxels} \right\rceil$$

where $\lceil\ \ \rceil$ denotes the ceiling operator, and the number of voxels is the total number of voxels in the lesion.

The code ensured that the random generation did not exceed this side length, so that no voxels could be added to the lesion that were outside of this bounding box.

The other check was a material check to make sure the same voxel never got added to the same lesion twice. This was done by a simple check of each voxel's material right before assigning a material (i.e. Calcium) to that voxel that would include it as a part of the lesion.

A lesion inserted using this random, compact insertion method is shown in Figures 4 and 5.

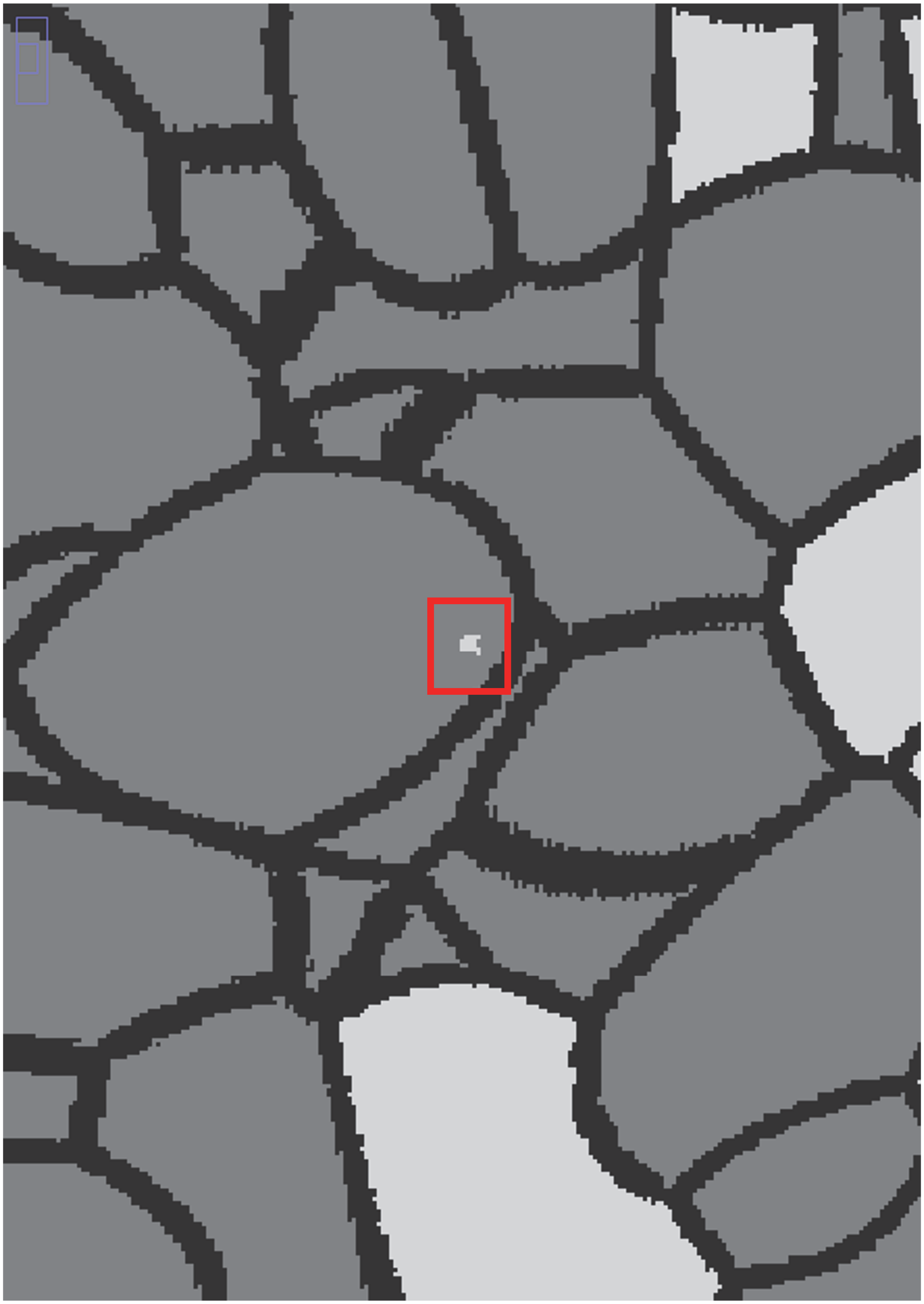

Figure 4: One slice in the z-direction of a phantom with a randomly inserted lesion (80 voxels), according to the method for random insertion as described in the text.

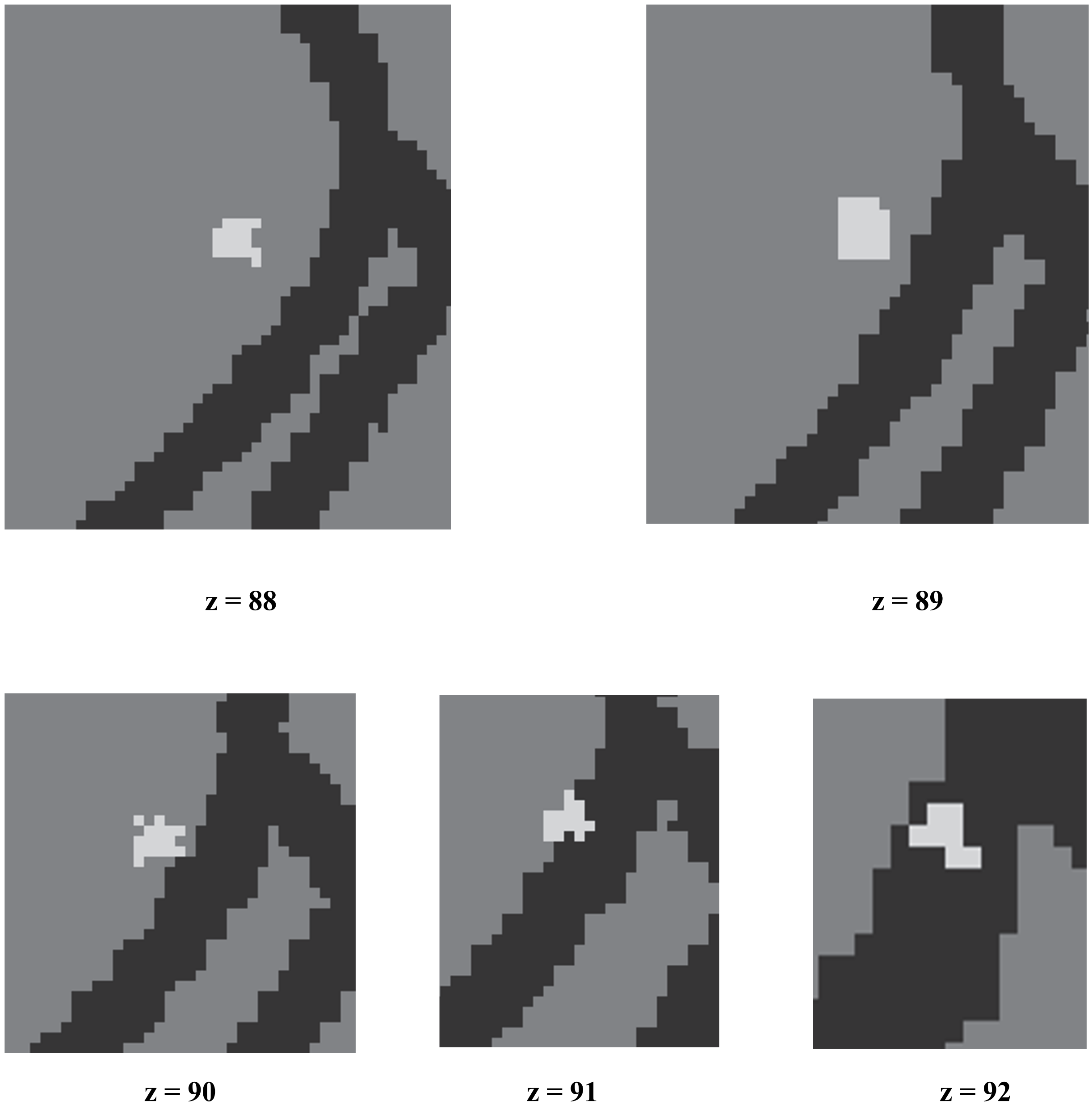

Figure 5: Zoomed in views of randomly inserted lesion from Figure 4. These were taken from 5 different slices in the z dimension. The size of this lesion was 80 voxels.

Non-stationary model of oblique x-ray incidence in amorphous selenium detectors: I. Point spread function

Raymond J. Acciavatti[a)] and Andrew D. A. Maidment
Department of Radiology, Perelman School of Medicine at the University of Pennsylvania, Philadelphia, PA 19104-4206, USA

(Received 23 April 2018; revised 2 October 2018; accepted for publication 16 November 2018; published 16 January 2019)

Purpose: In previous work, a theoretical model of the point spread function (PSF) for oblique x-ray incidence in amorphous selenium (*a*-Se) detectors was proposed. The purpose of this paper is to develop a complementary model that includes two additional features. First, the incidence angle and the directionality of ray incidence are calculated at each position, assuming a divergent x-ray beam geometry. This approach allows the non-stationarity of the PSF to be modeled. Second, this paper develops a framework that is applicable to a digital system, unlike previous work which did not model the presence of a thin-film transistor (TFT) array.
Methods: At each point on the detector, the incidence angle and the ray incidence direction are determined using ray tracing. Based on these calculations, an existing model for the PSF of the x-ray converter (*Med Phys*. 1995;**22**:365-374) is generalized to a non-stationary model. The PSF is convolved with the product of two rectangle functions, which model the sampling of the TFT array. The rectangle functions match the detector element (del) size in two dimensions.
Results: It is shown that the PSF can be calculated in closed form. This solution is used to simulate a digital mammography (DM) system at two x-ray energies (20 and 40 keV). Based on the divergence of the x-ray beam, the direction of ray incidence varies with position. Along this direction, the PSF is broader than the reference rect function matching the del size. The broadening is more pronounced with increasing obliquity. At high energy, the PSF deviates more strongly from the reference rect function, indicating that there is more blurring. In addition, the PSF is calculated along the polar angle perpendicular to the ray incidence direction. For this polar angle, the shape of the PSF is dependent upon whether the ray incidence direction is parallel with the sides of the detector. If the ray incidence direction is parallel with either dimension, the PSF is a perfect rectangle function, matching the del size. However, if the ray incidence direction is at an oblique angle relative to the sides of the detector, the PSF is not rectangular. These results illustrate the non-stationarity of the PSF.
Conclusions: This paper demonstrates that an existing model of the PSF of *a*-Se detectors can be generalized to include the effects of non-stationarity and digitization. The PSF is determined in closed form. This solution offers the advantage of shorter computation time relative to approaches that use numerical methods. This model is a tool for simulating *a*-Se detectors in future work, such as in virtual clinical trials with computational phantoms. © *2018 American Association of Physicists in Medicine* [https://doi.org/10.1002/mp.13313]

Key words: amorphous selenium, digital x-ray detectors, obliquity effect, point spread function (PSF), theoretical modeling

1. INTRODUCTION

The detectors commonly used in breast x-ray imaging are either indirect- or direct-converting. In an indirect-conversion detector such as cesium iodide (CsI), x rays are first converted to visible light, which spreads laterally.[1–4] The visible light is then converted to charged particles by photodiodes. This signal is digitized by a thin-film transistor (TFT) array. By contrast, there is no intermediate conversion of x rays to visible light in a direct-conversion detector such as amorphous-selenium (*a*-Se).[5–7] In these detectors, selenium atoms are ionized by x rays, creating electron-hole pairs. Based on an applied electric field, the electrons and holes migrate to opposite surfaces of the detector, and an image is formed. Badano et al. demonstrated that, for a fixed detector thickness and energy, *a*-Se is characterized by a narrower point response function than CsI at normal incidence[8]; in this paper, we use the term point spread function (PSF).

Due to the low atomic number of selenium ($Z = 34$), *a*-Se detectors have low x-ray absorption at high energies, and hence are more commonly used in low-energy applications, such as DM and digital breast tomosynthesis (DBT). At 20 keV, the quantum detection efficiency of 0.200 mm thick selenium is 98.3% at normal incidence, assuming a mass attenuation coefficient[9] of 4.82×10^3 mm^2/g and a density[10] of 4.20×10^{-3} g/mm^3.

Badano et al. developed a model of the obliquity effect in *a*-Se detectors.[8] They demonstrated that the PSF is broadened due to oblique incidence. In their work, the lateral spread of signal at each depth of *a*-Se was modeled with a Lorentzian function. The parameters were fit to the results of Monte Carlo simulations with MANTIS. Que and Rowlands offered a different approach for calculating the PSF.[11] Rather than calculate a single PSF that models all possible sources of blurring, Que and Rowlands identified multiple x-ray interactions that could introduce blurring, and modeled the PSF for each interaction separately. In their model of the obliquity effect, the PSF is blurred along the ray incidence direction, and is a delta function along the perpendicular direction.

One limitation of these previous works is that the presence of the TFT array was not included in the modeling assumptions, and hence the PSF models a non-pixelated system. The purpose of this paper is to develop a complementary model for a digital system, in which the signal in the x-ray converter is binned into detector elements (dels). For the purpose of this paper, we expand upon the model of the PSF developed by Que and Rowlands.[11] The PSF of the digital system is derived by convolving the PSF of the x-ray converter with the product of two rectangle functions, which match the del size in each direction.[12–14] It is shown that this convolution can be calculated in closed form. The advantage of deriving an analytical formula is that computation time is minimized relative to numerical integration methods.

In x-ray imaging, the shape of the PSF varies with position based on the angle of incidence and the directionality of the incident ray. An additional aim of this paper is to demonstrate how the PSF varies with position. We use this formulation to quantify non-stationarity in *a*-Se detectors.

2. MATERIALS AND METHODS

2.A. Coordinate system

A model of the PSF was previously developed by Que and Rowlands for an arbitrary incidence angle[11]; however, they did not model the non-stationarity of the PSF and did not consider the impact of digitization. These effects are now modeled from first principles for a breast imaging system.

Figure 1 shows a diagram of the acquisition geometry. The exit surface of the detector is defined to be the plane $z = 0$. The origin (O) is the point in this plane at which the ray is normally incident. The x-ray source is treated as a point source at the coordinate $(0, 0, d)$. Figure 1 also allows for the possibility of transforming to a coordinate system with a different reference point (M); in a breast imaging system, point M is the midpoint of the chest wall side of the detector. This transformation is considered in Section 2.D.

At each point along the ray, there are x-ray interactions with selenium atoms (Fig. 2). The electrons and holes that are produced migrate to opposite sides of the x-ray converter due to the applied electric field. We assume that signal is recorded at the exit surface as opposed to the entrance

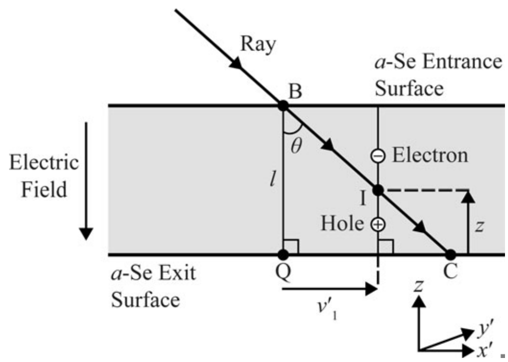

FIG. 2. Electron-hole pairs are produced by the ionization of selenium atoms along the path length of the ray. Due to the applied electric field, the electron and hole migrate to opposite ends of the detector. Signal is formed along the line segment $\overline{QC}$, which lies along the ray incidence direction (x'). For the purpose of this paper, it is presumed that there is no blurring along the perpendicular direction (y').

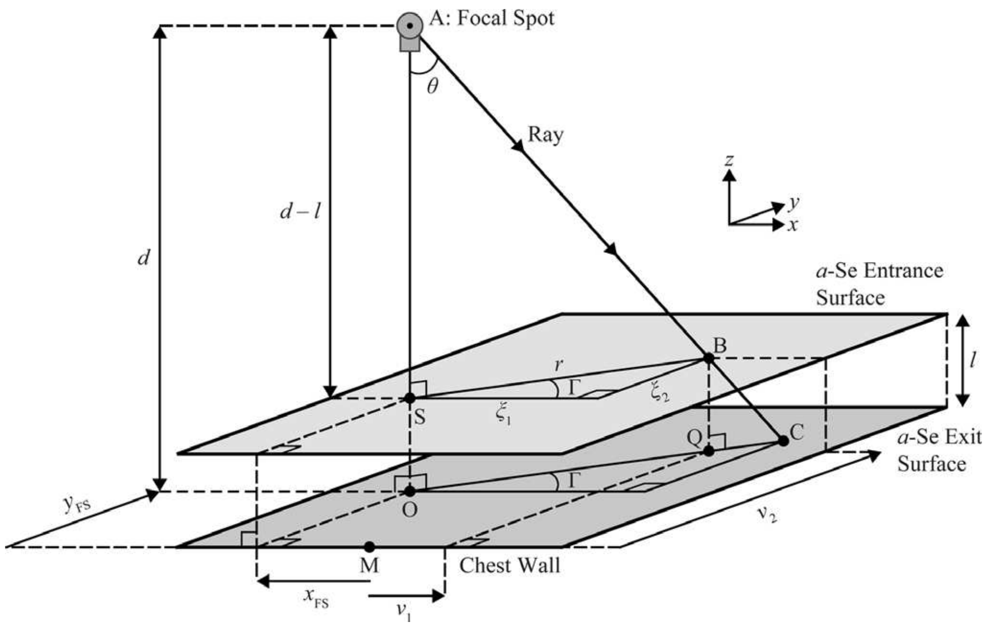

FIG. 1. A diagram of the acquisition geometry is shown. The direction of ray incidence is parallel with vector $\overrightarrow{SB}$ (or equivalently, vector $\overrightarrow{OC}$). Also, θ is the incidence angle, and Γ is the azimuthal angle of the ray. The path length of the ray through *a*-Se (thickness l) begins at point B and ends at point C. This figure is not to scale.

surface. For this reason, the directionality of the electric field determines whether the signal is produced by electrons or holes. The theoretical model can be applied to either. However, in this paper, the signal is taken to be produced by holes, like the AXS-2430 detector (Analogic Canada Corporation, Montreal, Quebec, Canada) modeled in Section 3.

Figure 2 shows how signal is produced along the x' direction in the exit surface of the x-ray converter; this is called the ray incidence direction throughout this paper. This direction lies along the angle Γ relative to the x direction (Fig. 1). To derive the PSF, the signal needs to be calculated in this rotated frame using the transformation

$$\begin{pmatrix} x \\ y \end{pmatrix} = \begin{pmatrix} \xi_1 \\ \xi_2 \end{pmatrix} + \begin{pmatrix} \cos\Gamma & -\sin\Gamma \\ \sin\Gamma & \cos\Gamma \end{pmatrix} \begin{pmatrix} v_1' \\ v_2' \end{pmatrix} \tag{1}$$

where v_1' is position along the ray incidence direction, v_2' is position in the perpendicular direction, and ξ_1 and ξ_2 are the x and y coordinates of the entrance point (B), respectively. Two trigonometric substitutions can be made based on Fig. 1

$$\cos\Gamma = \frac{\xi_1}{r} \tag{2}$$

$$\sin\Gamma = \frac{\xi_2}{r} \tag{3}$$

where

$$r = \sqrt{\xi_1^2 + \xi_2^2} \tag{4}$$

giving

$$v_1' = \frac{\xi_1}{r}x + \frac{\xi_2}{r}y - r \tag{5}$$

$$v_2' = \frac{-\xi_2}{r}x + \frac{\xi_1}{r}y \tag{6}$$

as the inverse transformation. The derivation that follows presumes that $r > 0$. There is normal incidence at the position for which $r = 0$; the PSF at this position is simply the TFT sampling function described in Section 2.B.

2.B. Depth-dependent PSF

The PSF associated with an arbitrary ionization point is now calculated. From Fig. 2, the v_1-coordinate of the ionization point (I) is $(l - z)\tan\theta$, where θ is the incidence angle. The PSF is

$$P_{\mathrm{I}} = \delta\left[v_1' - (l - z)\tan\theta\right]\delta(v_2'), \tag{7}$$

where the subscript "I" is an abbreviation for "Ionization". The angle θ can be determined from Fig. 1.

$$\tan\theta = \frac{r}{d - l} \tag{8}$$

Combining Eqs. (5)–(8) yields

$$P_{\mathrm{I}} = \delta\left(\frac{\xi_1}{r}x + \frac{\xi_2}{r}y + \frac{r}{d-l}z - \frac{dr}{d-l}\right)\delta\left(\frac{-\xi_2}{r}x + \frac{\xi_1}{r}y\right). \tag{9}$$

In a digital system, a TFT array bins the signal produced by the x-ray converter into dels. We model the PSF of the TFT array using

$$P_{\mathrm{TFT}} = \frac{1}{a_x a_y}\mathrm{rect}\left(\frac{x}{a_x}\right)\cdot\mathrm{rect}\left(\frac{y}{a_y}\right), \tag{10}$$

where a_x and a_y denote the del size in the x and y directions, respectively, and P_{TFT} denotes the PSF of the TFT array. If the x and y subscripts are removed, it is assumed that the del is square ($a_x = a_y = a$). Combining the effects of ionization and TFT sampling, the PSF can be written as the two-dimensional (2D) convolution

$$P_z = P_{\mathrm{I}} *_2 P_{\mathrm{TFT}}, \tag{11}$$

where the subscript z emphasizes that this PSF is associated with a specific depth.

2.C. Net PSF

One can integrate P_z over the thickness (l) to determine the net PSF of the system. This function is denoted P_{Net}.

$$P_{\mathrm{Net}} = \int_0^l N\cdot P_z\cdot dz \tag{12}$$

To convert Eq. (12) into a form with infinite integration limits, one can introduce a rectangle function to match the interval of integration, so that

$$P_{\mathrm{Net}} = \int_{-\infty}^{\infty} N\cdot P_z\cdot\mathrm{rect}\left(\frac{z - l/2}{l}\right)dz, \tag{13}$$

where

$$\mathrm{rect}(v) \equiv \begin{cases} 1, & |v| \le 1/2 \\ 0, & |v| > 1/2 \end{cases}. \tag{14}$$

In Eq. (12), the integrand is weighted by N, the relative number of x-ray quanta at each depth z. The function N is determined from the linear attenuation coefficient (μ) of selenium

$$N = C_{\mathrm{I}} e^{-\mu(l-z)\sec\theta}, \tag{15}$$

where

$$\sec\theta = \sqrt{1 + \left(\frac{r}{d-l}\right)^2}. \tag{16}$$

In Eq. (15), C_{I} is a normalization term, which can be determined from the normalization convention used by Swank[15]

$$\int_0^l N\cdot dz = 1 \tag{17}$$

giving

$$C_{\mathrm{I}} = \frac{\mu\sqrt{1 + \left(\frac{r}{d-l}\right)^2}}{1 - e^{-\mu l\sqrt{1+\left(\frac{r}{d-l}\right)^2}}}. \tag{18}$$

Combining Eqs. (9)–(11), (13), (15), (16) yields

$$P_{\mathrm{Net}} = \int_{-\infty}^{\infty} C_{\mathrm{I}} e^{-\mu\sqrt{1+\left(\frac{r}{d-l}\right)^2}(l-z)} \cdot \left[\int_{-\infty}^{\infty}\int_{-\infty}^{\infty}\left(\begin{array}{c}\delta\left(\frac{\xi_1}{r}\omega_1+\frac{\xi_2}{r}\omega_2+\frac{r}{d-l}z-\frac{dr}{d-l}\right)\\ \cdot\delta\left(\frac{-\xi_2}{r}\omega_1+\frac{\xi_1}{r}\omega_2\right)\frac{1}{a_xa_y}\mathrm{rect}\left(\frac{x-\omega_1}{a_x}\right)\mathrm{rect}\left(\frac{y-\omega_2}{a_y}\right)\end{array}\right)d\omega_1 d\omega_2\right]\mathrm{rect}\left(\frac{z-l/2}{l}\right)dz. \tag{19}$$

We can re-order the integration so that the integral over z is calculated first.

$$P_{\mathrm{Net}} = \frac{C_{\mathrm{I}}}{a_xa_y}\int_{-\infty}^{\infty}\int_{-\infty}^{\infty}\delta\left(\frac{-\xi_2}{r}\omega_1+\frac{\xi_1}{r}\omega_2\right) \cdot \mathrm{rect}\left(\frac{x-\omega_1}{a_x}\right)\mathrm{rect}\left(\frac{y-\omega_2}{a_y}\right) \cdot \int_{-\infty}^{\infty}\left(\begin{array}{c} e^{-\mu\sqrt{1+\left(\frac{r}{d-l}\right)^2}(l-z)}\mathrm{rect}\left(\frac{z-l/2}{l}\right)\\ \cdot\delta\left(\frac{\xi_1}{r}\omega_1+\frac{\xi_2}{r}\omega_2+\frac{r}{d-l}z-\frac{dr}{d-l}\right)\end{array}\right)dz\,d\omega_1 d\omega_2 \tag{20}$$

$$P_{\mathrm{Net}} = C_{\mathrm{Net}}\int_{-\infty}^{\infty}\int_{-\infty}^{\infty}\left(\begin{array}{c} e^{\frac{-\mu}{r}\sqrt{1+\left(\frac{d-l}{r}\right)^2}\left(\xi_1\omega_1+\xi_2\omega_2-r^2\right)}\mathrm{rect}\left(\frac{-\xi_1(d-l)}{lr^2}\omega_1-\frac{\xi_2(d-l)}{lr^2}\omega_2+\frac{2d-l}{2l}\right)\\ \cdot\delta\left(\frac{-\xi_2}{r}\omega_1+\frac{\xi_1}{r}\omega_2\right)\mathrm{rect}\left(\frac{x-\omega_1}{a_x}\right)\mathrm{rect}\left(\frac{y-\omega_2}{a_y}\right)\end{array}\right)d\omega_1 d\omega_2. \tag{26}$$

The integral over z can be evaluated using the identity for the delta function of a composition.[16,17] The identity presumes that the argument of the delta function has a finite number of zeros and that there are no repeated zeros.

$$\delta[g(z)] = \sum_k \frac{\delta(z-z_k)}{|g'(z_k)|} \tag{21}$$

Each term z_k denotes the kth zero of the function $g(z)$. In Eq. (20), the argument of the delta function has only one zero; namely,

$$z = \frac{-\xi_1(d-l)}{r^2}\omega_1 - \frac{\xi_2(d-l)}{r^2}\omega_2 + d \tag{22}$$

Thus

$$P_{\mathrm{Net}} = C_{\mathrm{Net}}\int_{-\infty}^{\infty}\int_{-\infty}^{\infty}\delta\left(\frac{-\xi_2}{r}\omega_1+\frac{\xi_1}{r}\omega_2\right) \cdot \mathrm{rect}\left(\frac{x-\omega_1}{a_x}\right)\mathrm{rect}\left(\frac{y-\omega_2}{a_y}\right) \cdot \int_{-\infty}^{\infty}\left(\begin{array}{c} e^{-\mu\sqrt{1+\left(\frac{r}{d-l}\right)^2}(l-z)}\mathrm{rect}\left(\frac{z-l/2}{l}\right)\\ \cdot\delta\left[z-\left(\frac{-\xi_1(d-l)}{r^2}\omega_1-\frac{\xi_2(d-l)}{r^2}\omega_2+d\right)\right]\end{array}\right)dz\,d\omega_1 d\omega_2 \tag{23}$$

where

$$C_{\mathrm{Net}} = \frac{C_{\mathrm{I}}(d-l)}{a_xa_yr}. \tag{24}$$

The integral can be evaluated using the definition of the delta function

$$\int_{-\infty}^{\infty}\phi(z)\cdot\delta(z-\beta)\cdot dz \equiv \phi(\beta), \tag{25}$$

where ϕ is an arbitrary function of z and $\beta \in \mathbb{R}$. This gives

Eq. (26) can be evaluated in closed form. There are three cases for the values of ξ_1 and ξ_2 that are now considered separately.

2.C.1. Case 1: ray incidence in $\pm x$ direction

First, ray incidence in the $\pm x$ direction is considered; that is, $\xi_1 \neq 0$ and $\xi_2 = 0$. From Eq. (4), it follows that $r = |\xi_1|$.

$$P_{\mathrm{Net},1} = C_{\mathrm{Net}}\int_{-\infty}^{\infty}\delta\left(\frac{\xi_1}{|\xi_1|}\omega_2\right)\mathrm{rect}\left(\frac{y-\omega_2}{a_y}\right)d\omega_2 \cdot \int_{-\infty}^{\infty} e^{\frac{-\xi_1}{|\xi_1|}\mu(\omega_1-\xi_1)\sqrt{1+\left(\frac{d-l}{\xi_1}\right)^2}} \cdot \mathrm{rect}\left(\frac{-(d-l)}{l\xi_1}\omega_1+\frac{2d-l}{2l}\right)\mathrm{rect}\left(\frac{x-\omega_1}{a_x}\right)d\omega_1 \tag{27}$$

The delta function can be simplified using the sign function ("sgn")

$$\delta\left(\frac{\xi_1}{|\xi_1|}\omega_2\right) = \delta[\mathrm{sgn}(\xi_1)\cdot\omega_2] \tag{28}$$

$$= \delta(\omega_2), \tag{29}$$

where

$$\operatorname{sgn}(v) \equiv \begin{cases} -1, v<0 \\ 0, v=0 \\ 1, v>0. \end{cases} \tag{30}$$

The exponential in Eq. (27) can also be simplified with the sign function. Additionally, it is useful to flip the signs of the arguments of the two rect functions in Eq. (27); this is justified since the rect function [Eq. (14)] is an even function.

$$P_{\mathrm{Net},1} = C_{\mathrm{Net}} \cdot \operatorname{rect}\left(\frac{y}{a_y}\right) \cdot \int_{-\infty}^{\infty} e^{-\operatorname{sgn}(\xi_1)\cdot\mu(\omega_1-\xi_1)\sqrt{1+\left(\frac{d-l}{\xi_1}\right)^2}} \cdot \operatorname{rect}\left(\frac{d-l}{l\xi_1}\omega_1 + \frac{l-2d}{2l}\right)\operatorname{rect}\left(\frac{\omega_1 - x}{a_x}\right)d\omega_1 \tag{31}$$

To determine the interval of overlap for the rect functions in Eq. (31), the integrand needs to be rewritten in a form that shows the centroid and width of each rect function.

$$P_{\mathrm{Net},1} = C_{\mathrm{Net}} \cdot \operatorname{rect}\left(\frac{y}{a_y}\right) \cdot \int_{-\infty}^{\infty} e^{-\operatorname{sgn}(\xi_1)\cdot\mu(\omega_1-\xi_1)\sqrt{1+\left(\frac{d-l}{\xi_1}\right)^2}} \cdot \operatorname{rect}\left(\frac{\omega_1 - \frac{(2d-l)\xi_1}{2(d-l)}}{\frac{\xi_1 l}{d-l}}\right)\operatorname{rect}\left(\frac{\omega_1 - x}{a_x}\right)d\omega_1 \tag{32}$$

For each rect function, the centroid is given by the offset term in the numerator, while the width is given by the denominator. The left-hand endpoints of the two rect functions are thus

$$h_{1,1} = \min\left\{\xi_1, \frac{d\xi_1}{d-l}\right\} \tag{33}$$

$$h_{1,2} = x - \frac{a_x}{2}. \tag{34}$$

The first subscript identifies the case number, while the second subscript identifies the order of the rect function when reading Eq. (32) from left-to-right. Similarly, the right-hand endpoints are

$$j_{1,1} = \max\left\{\xi_1, \frac{d\xi_1}{d-l}\right\} \tag{35}$$

$$j_{1,2} = x + \frac{a_x}{2}. \tag{36}$$

It is useful to re-number the rect functions based on the positioning of the left-hand endpoints.

$$h'_{1,1} = \min\{h_{1,1}, h_{1,2}\} \tag{37}$$

$$h'_{1,2} = \max\{h_{1,1}, h_{1,2}\} \tag{38}$$

The primed superscript emphasizes that the ordering is now based on position in space. Under this ordering of the rect functions, the right-hand endpoints are as follows.

$$j'_{1,1} = \begin{cases} j_{1,1}, & h_{1,1} \le h_{1,2} \\ j_{1,2}, & h_{1,1} > h_{1,2} \end{cases} \tag{39}$$

$$j'_{1,2} = \begin{cases} j_{1,2}, & h_{1,1} \le h_{1,2} \\ j_{1,1}, & h_{1,1} > h_{1,2} \end{cases} \tag{40}$$

Two mutually exclusive possibilities for the positioning of the two rect functions are now considered.

If the two rect functions do not overlap, as would occur if the right-hand endpoint of one rect function is less than or equal to the left-hand endpoint of the other rect function, then $j'_{1,1} \le h'_{1,2}$, and the integral in Eq. (32) is zero.

If the two rect functions overlap, the lower limit of overlap is the larger of the two left-hand endpoints.

$$t_{1,1} = h'_{1,2} \tag{41}$$

Similarly, the upper limit of overlap is the smaller of the two right-hand endpoints.

$$t_{1,2} = \min\{j'_{1,1}, j'_{1,2}\} \tag{42}$$

The limits of overlap ($t_{1,1}$ and $t_{1,2}$) are arranged by position based on the second subscript. The integral in Eq. (32) can now be evaluated

$$P_{\mathrm{Net},1} = \begin{cases} 0, & j'_{1,1} \le h'_{1,2} \\ C_{\mathrm{Net}} \cdot \operatorname{rect}\left(\frac{y}{a_y}\right) \cdot \int_{t_{1,1}}^{t_{1,2}} e^{-\operatorname{sgn}(\xi_1)\cdot\mu(\omega_1-\xi_1)\sqrt{1+\left(\frac{d-l}{\xi_1}\right)^2}} d\omega_1, & \text{otherwise} \end{cases} \tag{43}$$

$$= \begin{cases} 0, & j'_{1,1} \le h'_{1,2} \\ \dfrac{-\operatorname{sgn}(\xi_1)\cdot\operatorname{rect}\left(\frac{y}{a_y}\right)}{a_x a_y\left(1-e^{-\mu l\sqrt{1+\left(\frac{\xi_1}{d-l}\right)^2}}\right)}\left[e^{-\operatorname{sgn}(\xi_1)\cdot\mu(t_{1,2}-\xi_1)\sqrt{1+\left(\frac{d-l}{\xi_1}\right)^2}} - e^{-\operatorname{sgn}(\xi_1)\cdot\mu(t_{1,1}-\xi_1)\sqrt{1+\left(\frac{d-l}{\xi_1}\right)^2}}\right], & \text{otherwise} \end{cases} \tag{44}$$

which is a closed-form solution for the PSF.

2.C.2. Case 2: ray incidence in ±y direction

In the case of ray incidence in the $\pm y$ direction. Equation (26) can be evaluated with the substitutions: $\xi_1 = 0$ and $\xi_2 \neq 0$. Following the reasoning used in the transition between Eqs. (27) and (32), it can be shown that

$$P_{\mathrm{Net},2} = C_{\mathrm{Net}} \cdot \mathrm{rect}\left(\frac{x}{a_x}\right) \cdot \int_{-\infty}^{\infty} e^{-\mathrm{sgn}(\xi_2)\cdot\mu(\omega_2-\xi_2)\sqrt{1+\left(\frac{d-l}{\xi_2}\right)^2}} \cdot \mathrm{rect}\left(\frac{\omega_2 - \frac{(2d-l)\xi_2}{2(d-l)}}{\frac{\xi_2 l}{d-l}}\right)\mathrm{rect}\left(\frac{\omega_2 - y}{a_y}\right)d\omega_2 \tag{45}$$

Equation (45) is in a form analogous to Eq. (32). This integral can be evaluated with the approach described in Eqs. (33)–(44). This solution is given explicitly in the Data S1.

2.C.3. Case 3: ray incidence in an oblique direction

In the case of ray incidence in an oblique direction, Eq. (26) can be evaluated with the substitutions: $\xi_1 \neq 0$ and $\xi_2 \neq 0$. Rewriting the delta function in Eq. (26)

$$\delta\left(\frac{-\xi_2}{r}\omega_1 + \frac{\xi_1}{r}\omega_2\right) = \frac{r}{|\xi_1|}\delta\left(\omega_2 - \frac{\xi_2}{\xi_1}\omega_1\right), \tag{46}$$

the ω_2-integral can be evaluated.

$$P_{\mathrm{Net},3} = \frac{C_{\mathrm{Net}} r}{|\xi_1|}\int_{-\infty}^{\infty} e^{\frac{-\mu r(\omega_1-\xi_1)}{\xi_1}\sqrt{1+\left(\frac{d-l}{r}\right)^2}} \cdot \mathrm{rect}\left(\frac{\omega_1 - \frac{(2d-l)\xi_1}{2(d-l)}}{\frac{\xi_1 l}{d-l}}\right)\mathrm{rect}\left(\frac{\omega_1 - x}{a_x}\right) \cdot \mathrm{rect}\left(\frac{\omega_1 - \frac{y\xi_1}{\xi_2}}{\frac{a_y \xi_1}{\xi_2}}\right)d\omega_1 \tag{47}$$

To evaluate Eq. (47) in closed form, it is necessary to determine the interval of overlap for the three rect functions in the integrand. This solution is detailed in the Data S1.

2.D. Coordinate transformation

Figure 1 shows how these equations can be applied to a breast imaging system by transforming the coordinate system. In Fig. 1, point M is a reference point in the plane $z = 0$; that is, the midpoint of the chest wall side of the detector. In our previous work, the focal spot coordinates (x_{FS} and y_{FS}) were measured relative to this point.[18,19] In DM, x_{FS} and y_{FS} should be roughly aligned with point M. The exact positioning in a physical system is sensitive to geometric imprecisions.

The equations for transforming the coordinate system between reference points O and M are as follows:

$$\xi_1 = v_1 - x_{FS} \tag{48}$$

$$\xi_2 = v_2 - y_{FS}, \tag{49}$$

where v_1 and v_2 are the coordinates of point B (the entrance point of the ray) relative to point M as shown in Fig. 1.

3. RESULTS

3.A. Modeling parameters

We model a next-generation tomosynthesis (NGT) system that was constructed at the University of Pennsylvania for research use.[20–25] This system, which is discussed in more detail in Part 2, is capable of source motion in two directions (x and y). For the purpose of Part 1, only a 2D DM image is simulated with the acquisition parameters given in Table I.

Similar to previous work[18,19], the focal spot is treated as a point in the plane of the chest wall ($y_{FS} = 0$), as shown in Fig. 3 by the positioning of the origin (O) along this side of the detector. This differs from the positioning of the origin in Fig. 1, which is more generalized for an arbitrary coordinate for the focal spot.

The NGT system was built with the AXS-2430 detector described previously. The del dimensions are 0.085 mm × 0.085 mm, and the active area is 304.64 mm × 239.36 mm. Each del is labeled with integer indices m_x and m_y. The coordinates of the centroid of an arbitrary del are

$$v_1 = (m_x - 1792 - 1/2)a_x \tag{50}$$

$$v_2 = (m_y - 1/2)a_y, \tag{51}$$

where m_x varies from 1 to 3584 and m_y varies from 1 to 2816.

Since there is an even number of dels along the chest wall, point M is at the interface between two dels. For the purpose of this simulation, we assume that x_{FS} is aligned with the centroid of the del with an x index of 1793; that is, x_{FS} is displaced from point M by half of a pixel (Table I). This positioning is chosen for convenience so that the centroids of the dels with this x index are aligned with the azimuthal angle Γ = 90° (Fig. 3), which is considered in Section 3.B.1.

TABLE I. The acquisition parameters for the simulation of a DM system are summarized.

Acquisition parameter	Value (mm)
Del size (a)	0.085
d	650.0
Se thickness (l)	0.200
x_{FS}	0.5a (0.0425)
y_{FS}	0

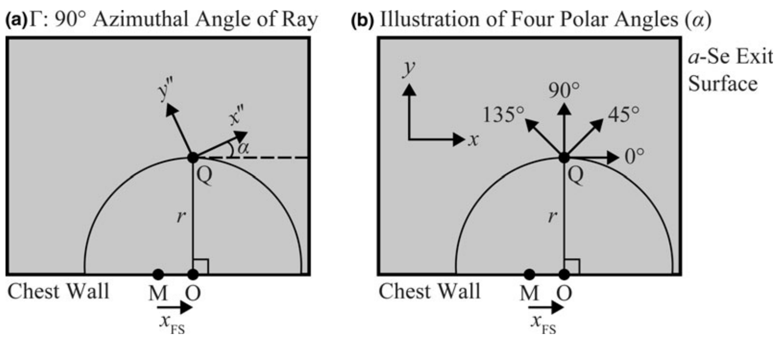

FIG. 3. (a) For simulation of a DM system, the focal spot is treated as a point in the plane of the chest wall, and hence the origin (O) is positioned along this side of the detector. Each point on the circle centered on point O is characterized by the same incidence angle (θ), but by a different azimuthal angle (Γ) for the ray; here, $\Gamma = 90°$. (b) Four examples are given (0°, 45°, 90°, and 135°) to illustrate the polar angle, α.

3.B. Calculation of the net PSF

3.B.1. Ray Incidence along 90° azimuthal angle

In Fig. 4(b), the net PSF is calculated at 20 keV at a position with 15° incidence; that is, at the coordinates $m_x = 1793$ and $m_y = 2049$. This position is aligned with the azimuthal angle $\Gamma = 90°$ (Fig. 3). The origin of the surface plot is matched to this position. Due to the obliquity effect, the surface is not a perfect 2D rect function [Fig. 4(a)], like the PSF for detector sampling (P_{TFT}).

In Fig. 5, cross sections through this surface plot are calculated along various polar angles (α) using the transformation

$$\begin{pmatrix} x \\ y \end{pmatrix} = \begin{pmatrix} \xi_1 \\ \xi_2 \end{pmatrix} + \begin{pmatrix} \cos\alpha & -\sin\alpha \\ \sin\alpha & \cos\alpha \end{pmatrix} \begin{pmatrix} x'' \\ y'' \end{pmatrix}. \tag{52}$$

Figure 3(a) illustrates the rotated coordinates x'' and y''. Also, Fig. 3(b) shows four polar angles ($\alpha = 0°$, 45°, 90°, and 135°), which are used as examples throughout this paper. In Fig. 5, the cross sections align with the centroid of the del; thus, $y'' = 0$.

If the polar angle is perpendicular to the ray incidence direction ($\alpha = 0°$), Fig. 5(a) shows that the cross section is a 2D rect function with 0.085 mm width. This width matches the del size. Conversely, if the polar angle is aligned with the ray incidence direction ($\alpha = 90°$), the width of the net PSF is broadened by 63.2% [Fig. 5(c)]. This broadening is an illustration of the obliquity effect.

Measurements can also be made along 45° or 135° polar angles, which lie along the diagonal of the del. These two cross sections are equivalent, as shown in Fig. 5(b). The width of this cross section is 0.120 mm; that is, $\sqrt{2}$ times larger than 0.085 mm.

3.B.2. Ray incidence along 45° azimuthal angle

In Fig. 3, a circle centered on point O can be used to identify positions with the same incidence angle but different azimuthal angles for the ray incidence direction. The position corresponding to a 45° azimuthal angle (Γ) is illustrated in Fig. 6 (point C). At 15° incidence, the del that is most closely aligned with this azimuthal angle has the coordinates $m_x = 3241$ and $m_y = 1449$. Figure 7 shows cross sections of the net PSF along various polar angles, similar to Fig. 5.

In Section 3.B.1., we found that the net PSF is a rect function along the polar angle perpendicular to the ray incidence

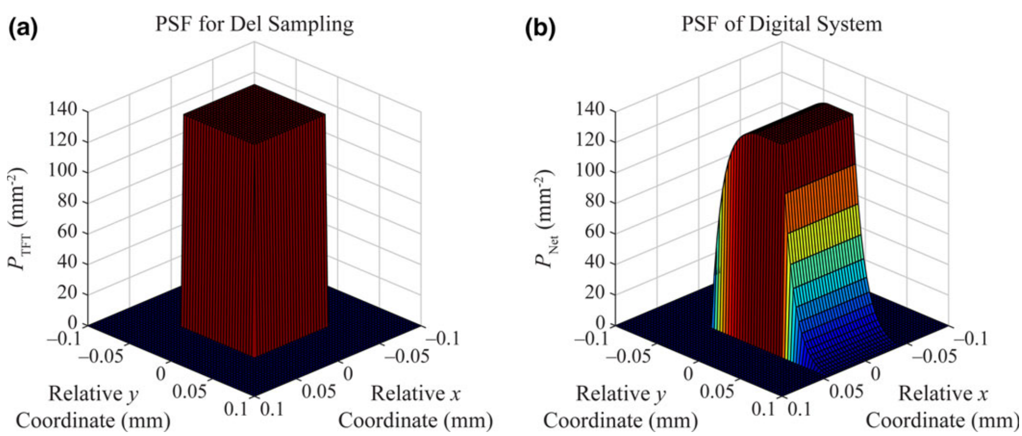

FIG. 4. The PSF is illustrated by surface plots at 20 keV. (a) The PSF for del sampling (P_{TFT}) is a 2D rect function with dimensions 0.085 mm × 0.085 mm. (b) The net PSF is shown at a position with 15° incidence and a 90° azimuthal angle. The cross sections are rect functions along the x direction (perpendicular to the ray incidence direction), but are blurred along the y direction (parallel with the ray incidence direction). [Color figure can be viewed at wileyonlinelibrary.com]

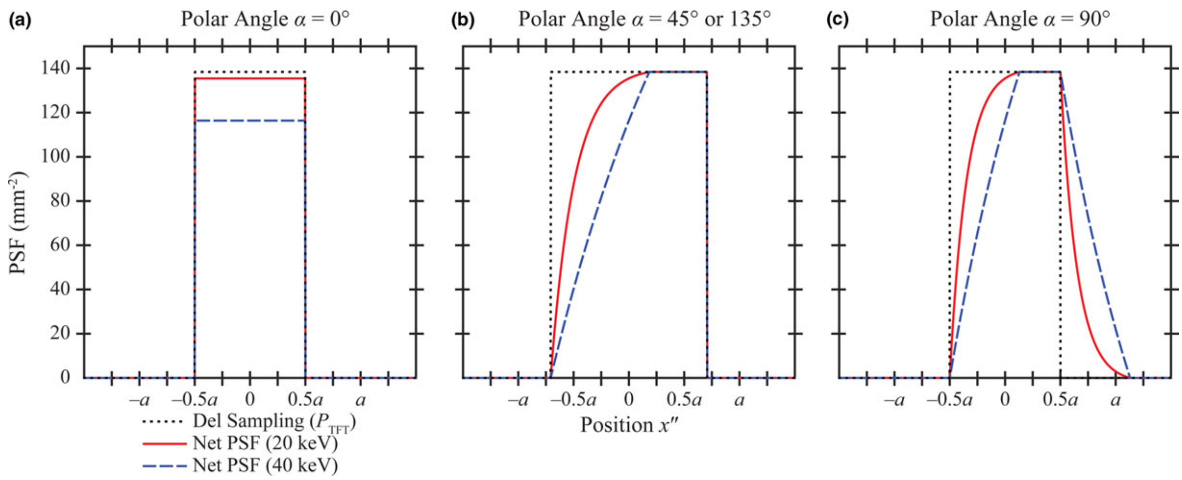

FIG. 5. Cross sections of the net PSF are shown at a position with 15° incidence and a 90° azimuthal angle. (a) The signal is a rect function along the 0° polar angle (perpendicular to the ray incidence direction). (b) Along the 45° or 135° polar angle, the net PSF is blurred over a 0.120 mm length, matching the diagonal of the del. (c) The net PSF is broader than the width of the del (0.085 mm) along a 90° polar angle (the ray incidence direction). [Color figure can be viewed at wileyonlinelibrary.com]

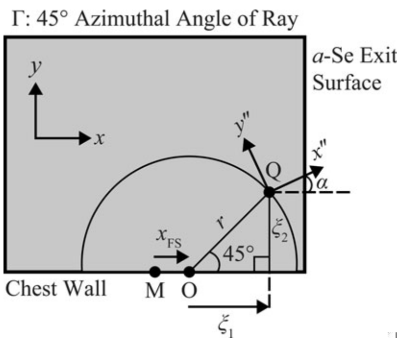

FIG. 6. Varying the position around the circle centered on point O changes the azimuthal angle (Γ); here, Γ = 45°.

direction. This result is no longer the case, as shown in Fig. 7(c) at a 135° polar angle. This finding illustrates the non-stationarity of the net PSF.

Figure 7 indicates that the net PSF is 0.174 mm wide along the ray incidence direction [$\alpha = 45°$, Fig. 7(b)], and is 0.123 mm wide along a 45° angle relative to the ray incidence direction [$\alpha = 0°$ or 90°, Fig. 7(a)]. These cross sections are broader than the reference rect functions. Also, they do not match the cross sections in Section 3.B.1. at similar polar angles, further demonstrating the non-stationarity of the net PSF.

3.B.3. Effect of x-ray energy

Although low energies are typically used in breast imaging to maximize subject contrast,[26,27] there are applications that require higher energy; for example, contrast-enhanced digital mammography (CE-DM) and contrast-enhanced digital breast tomosynthesis (CE-DBT).[28–37] In CE-DM and CE-DBT, an iodinated contrast agent is used to quantify blood flow to a tumor. X-ray images are acquired at energies above

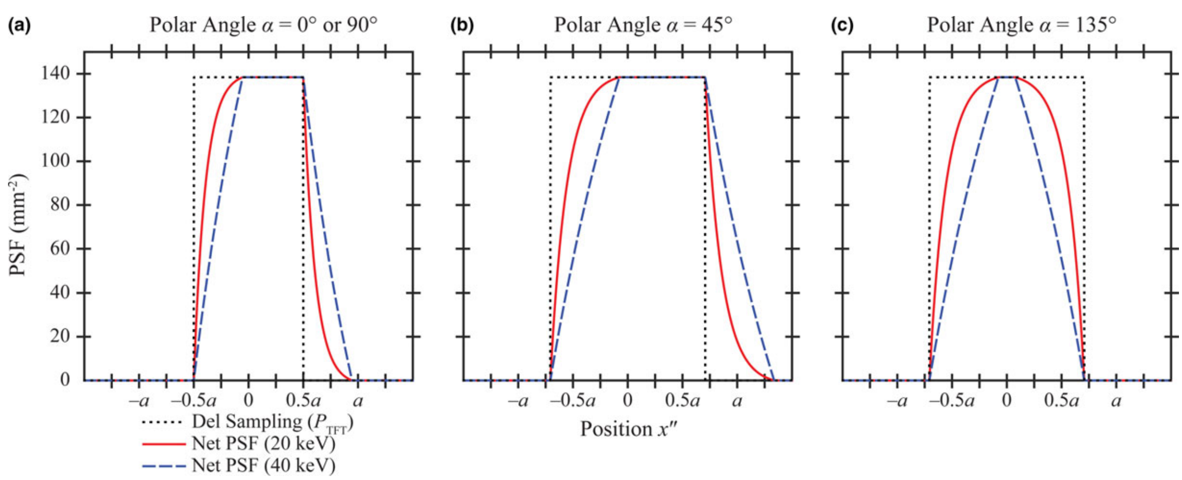

FIG. 7. Cross sections of the net PSF are shown at a position with the same incidence angle as Fig. 5 but a different azimuthal angle (Γ = 45°). The cross sections differ from those in Fig. 5 at similar polar angles; this illustrates the non-stationarity of the net PSF. [Color figure can be viewed at wileyonlinelibrary.com]

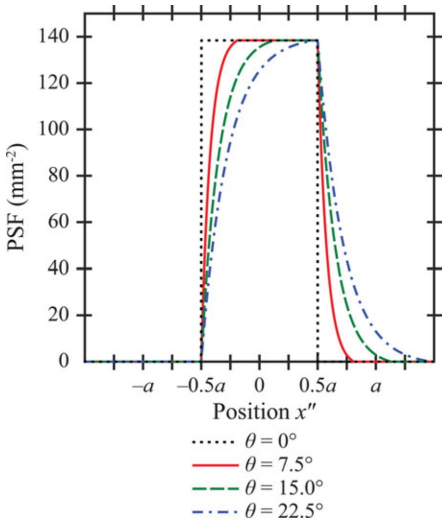

FIG. 8. The net PSF is broadened with increasing obliquity. This figure assumes that the x-ray energy is 20 keV, and that the PSF is measured along the polar angle aligned with the ray incidence direction (Γ = α = 90°). [Color figure can be viewed at wileyonlinelibrary.com]

and below the K edge of iodine (33.2 keV), and a weighted logarithmic subtraction is used to measure perfusion.

For simulation of CE-DM, the PSF at 40 keV is also shown in Figs. 5 and 7. The PSF deviates more strongly from the reference rect function at 40 keV (μ = 3.02 mm^{-1}) than at 20 keV (μ = 20.2 mm^{-1}). These results illustrate that there is loss of resolution at high energy; this is expected, since the x-ray beam is attenuated less quickly as it passes through the x-ray converter.

3.B.4. Effect of incidence angle

Figure 8 considers four incidence angles (θ = 0°, 7.5°, 15.0°, and 22.5°) to illustrate the effect on the PSF. For the purpose of this figure, the 90° azimuthal angle (Γ) is considered (Fig. 3), and the polar angle (α) is aligned with this direction (Γ = α = 90°). The x-ray energy is taken to be 20 keV.

Figure 8 demonstrates that increasing the incidence angle gives rise to a broader PSF. This result is expected; the x-ray beam projects onto the exit surface with the length $l \tan \theta$ (line segment $\overline{QC}$ in Fig. 2). Since $\tan \theta$ is an increasing function, the signal is spread across a broader length at higher obliquity.

4. DISCUSSION

In previous work, the PSF of an *a*-Se detector was calculated from first principles, assuming that the incidence angle (θ) was given and that the ray incidence direction was the x direction.[11] By contrast, this paper determines how the incidence angle and the ray incidence direction vary with position based on the divergence of the x-ray beam. This allows the non-stationarity of the PSF to be demonstrated. In addition, this paper includes digitization in the model, unlike previous work.

We analyze cross sections through the PSF at various polar angles. Oblique incidence blurs the shape of the PSF relative to a reference rect function matching the del size. The resolution loss is more pronounced at high energy, since there is less attenuation in the x-ray converter. In addition, the PSF is blurred more strongly at positions with higher obliquity; for example, at positions with increasing distance (y) from the chest wall in DM. Although these results were illustrated with the AXS-2430 detector, similar results are expected in other *a*-Se detectors.

This paper has applications in simulating *a*-Se detectors in virtual clinical trials (VCTs), which can be used to evaluate new imaging technologies at low cost without requiring human subjects.[38] Since P_{Net} was evaluated with a closed-form solution, this paper ensures that the detector signal calculation in a VCT is computationally efficient.

Some of the limitations of this paper and directions for future modeling are now discussed. In future work, the three-dimensional (3D) PSF of a DBT reconstruction should be calculated from the 2D PSFs of the projection images. In some DBT systems, the detector rotates during the scan.[18,19,39–41] Detector rotation can be modeled with a different coordinate transformation for point M (Section 2.D.). In addition, the 3D PSF should model the reconstruction filter.[42]

In this paper, it is assumed that the electron and hole migrate in perfect orthogonal paths to opposite sides of the *a*-Se x-ray converter (Fig. 2). However, future work should consider additional x-ray interactions such as K fluorescence and Compton scatter, which can act as sources of blurring according to the work of Que and Rowlands.[11] Also, the focal spot can introduce blurring[43] that was not modeled in this paper, since the x-ray source was assumed to be point-like.

This paper presumes that the collection efficiency of selenium is 100%. However, future work should model how the collection efficiency is dependent on the depth (z) of the interaction.[8] Also, while this paper presumes that the entire area of each del is sensitive to x-rays, future work should model the fill factor.

5. CONCLUSION

This paper is an extension of previous work modeling the PSF for oblique x-ray incidence in *a*-Se detectors.[11] There are two differences between this paper and previous work. First, this paper develops a model of the non-stationarity of the PSF based on the divergent x-ray beam geometry. Second, while previous work calculated the PSF for the x-ray converter, this paper provides a complementary derivation for a digital system.

In this paper, the solution for the PSF is determined in closed form. This formula is a tool that can be used in future simulations of *a*-Se detectors (e.g., in VCTs). One advantage of a closed-form solution is that computation time is minimized relative to numerical methods.

ACKNOWLEDGMENTS

We thank Denny L. Y. Lee for many useful discussions on the physics of *a*-Se detectors. In addition, we are grateful to David Higginbotham for providing constructive feedback. Support was provided by the following grants: PDF14302589 and IIR13264610 from Susan G. Komen®; 1R01CA154444 and 1R01CA196528 from the National Institute of Health; IRSA 1016451 from the Burroughs Wellcome Fund; and W81XWH-18-1-0082 from the Department of Defense Breast Cancer Research Program. In addition, equipment support was provided by Analogic Inc., Barco NV, and Real Time Tomography (RTT), LLC (Villanova, PA). The content is solely the responsibility of the authors and does not necessarily represent the official views of the funding agencies.

CONFLICTS OF INTEREST

Andrew D. A. Maidment is a scientific advisor to RTT, and his spouse is an employee and shareholder of RTT.

APPENDIX: NOMENCLATURE

Symbol	Meaning
$*_2$	Two-dimensional convolution operator
α	Polar angle (defined in Figs. 3 and 6)
Γ	Azimuthal angle of ray (Fig. 1)
δ	Delta function
θ	Incidence angle (Figs. 1, 2).
μ	Linear attenuation coefficient of selenium
ξ_1, ξ_2	Coordinates of point B relative to point S (Fig. 1)
ω_1, ω_2	Dummy variables in the evaluation of a convolution [Eq. (19)].
a_x, a_y	Del dimensions; if $a_x = a_y$, the dimension is abbreviated a
C_I	Normalization term for P_I [Eq. (18)]
C_Net	Normalization term for P_Net [Eq. (24)]
CE-DBT	Contrast-enhanced digital breast tomosynthesis
CE-DM	Contrast-enhanced digital mammography.
d	Distance between focal spot and origin in Fig. 1
DBT	Digital breast tomosynthesis
Del	Detector element
DM	Digital mammography
FS	Focal spot
$h_{i,k}$	Left-hand endpoint of rect function [i = case number, k = ordering based on Eq. (32)]
$h'_{i,k}$	Left-hand endpoint of rect function [i = case number, k = ordering by positioning of left-hand endpoints]
$j_{i,k}$	Right-hand endpoint of rect function [i = case number, k = ordering based on Eq. (32)]
$j'_{i,k}$	Right-hand endpoint of rect function [i = case number, k = ordering by positioning of left-hand endpoints]
l	Selenium thickness
m_x, m_y	Del indices [Eqs. (50), (51)]
MTF	Modulation transfer function

Appendix. Continued.

Symbol	Meaning
N	Relative number of x-ray quanta at depth z [Eq. (15)]
P_I	PSF associated with arbitrary ionization point in x-ray converter
P_Net	Net PSF (additional subscripts denote case number)
P_TFT	PSF of TFT array
P_z	Depth-dependent PSF (combined effect of P_I and P_TFT)
PSF	Point spread function
r	Distance between points B and S in Fig. 1
$t_{i,k}$	Lower (k = 1) or upper (k = 2) limit of overlap of rect functions (i = case number)
TFT	Thin-film transistor
v_1, v_2	Coordinate transformation for point B [Eqs. (48), (49)]
v'_1	Position (relative to point Q) measured along x' direction in Fig. 2
v'_2	Position (relative to point Q) measured along y' direction
VCT	Virtual clinical trial
x'	Position along ray incidence direction
x''	Position measured along polar angle α in Figs. 3 and 6
x_FS, y_FS	Focal spot coordinates (Fig. 1)
y'	Position perpendicular to ray incidence direction
y''	Position measured perpendicular to polar angle α in Figs. 3 and 6
Z	Atomic number

[a]Author to whom correspondence should be addressed. Electronic mail: raymond.acciavatti@uphs.upenn.edu; Telephone: +1 215 746 8759; Fax: +1 215 746 8764.

REFERENCES

1. Zhao W, Ristic G, Rowlands JA. X-ray imaging performance of structured cesium iodide scintillators. *Med Phys*. 2004;31:2594–605.
2. Badano A, Kyprianou IS, Jennings RJ. Anisotropic imaging performance in breast tomosynthesis. *Med Phys*. 2007;34:4076–4091.
3. Freed M, Park S, Badano A. A fast, angle-dependent, analytical model of CsI detector response for optimization of 3D x-ray breast imaging systems. *Med Phys*. 2010;37:2593–2605.
4. Freed M, Park S, Badano A. Erratum: a fast, angle-dependent, analytical model of CsI detector response for optimization of 3D x-ray breast imaging systems [Med. Phys. 37, 2593-2605 (2010)]. *Med Phys*. 2011;38:2307.
5. Zhao W, Ji WG, Debrie A, Rowlands JA. Imaging performance of amorphous selenium based flat-panel detectors for digital mammography: characterization of a small area prototype detector. *Med Phys*. 2003;30:254–263.
6. Zhao B, Zhao W. Imaging performance of an amorphous selenium digital mammography detector in a breast tomosynthesis system. *Med Phys*. 2008;35:1978–1987.
7. Hajdok G, Battista JJ, Cunningham IA. Fundamental x-ray interaction limits in diagnostic imaging detectors: spatial resolution. *Med Phys*. 2008;35:3180–3193.
8. Badano A, Freed M, Fang Y. Oblique incidence effects in direct x-ray detectors: a first-order approximation using a physics-based analytical model. *Med Phys*. 2011;38:2095–2098.
9. Hubbell JH, Seltzer SM. X-Ray Mass Attenuation Coefficients [cited 2018 March 12]. Available from: https://www.nist.gov/pml/x-ray-mass-attenuation-coefficients.
10. Hajdok G, Cunningham IA. Penalty on the detective quantum efficiency from off-axis incident x rays. In: Yaffe MJ, Flynn MJ, eds. *Physics of Medical Imaging*. San Diego, CA: SPIE; 2004:109–118.

11. Que W, Rowlands JA. X-ray imaging using amorphous selenium: inherent spatial resolution. *Med Phys*. 1995;22:365–374.
12. Acciavatti RJ, Maidment ADA. An analytical model of NPS and DQE comparing photon counting and energy integrating detectors. In: Samei E, Pelc NJ, eds. *Physics of Medical Imaging*. San Diego, CA: SPIE; 2010:76220I-1–76220I-12.
13. Acciavatti RJ, Maidment ADA. A comparative analysis of OTF, NPS, and DQE in energy integrating and photon counting digital x-ray detectors. *Med Phys*. 2010;37:6480–6495.
14. Acciavatti R, Maidment A. TU-FG-209-01: a model of noise anisotropy in amorphous selenium digital detectors. *Med Phys*. 2016;43:3760.
15. Swank RK. Calculation of modulation transfer functions of x-ray fluorescent screens. *Appl Opt*. 1973;12:1865–1870.
16. Barrett HH, Myers KJ. Chapter 2: dirac delta and other generalized functions. In: Saleh BEA, ed. *Foundations of Image Science*. New York, NY: John Wiley & Sons; 2004:63–94.
17. Lea SM. Chapter 6: generalized functions in physics. In: *Mathematics for Physicists*. Belmont, CA: Brooks/Cole - Thomson Learning; 2004:287–322.
18. Acciavatti RJ, Maidment ADA. Observation of super-resolution in digital breast tomosynthesis. *Med Phys*. 2012;39:7518–7539.
19. Acciavatti RJ, Maidment ADA. Oblique reconstructions in tomosynthesis: II. Super-resolution. *Med Phys*. 2013;40:111912-1–111912-19.
20. Maidment AD, Acciavatti R, Vent T, et al. *SSC14-03: Construction of a Prototype Digital Breast Tomosynthesis System with Superior Spatial Resolution*. Radiological Society of North America (RSNA) Conference, Chicago, IL; 2016.
21. Ferris WS, Vent TL, Maidment TD, Acciavatti RJ, Wurtele DE, Maidment ADA. Geometric Calibration for a Next-Generation Digital Breast Tomosynthesis System. In: Flohr TG, Lo JY, Schmidt TG, eds. *Physics of Medical Imaging*. Orlando, FL: SPIE; 2017:101324C-1–101324C-10.
22. Maidment TD, Vent TL, Ferris WS, Wurtele DE, Acciavatti RJ, Maidment ADA. Comparing the Imaging Performance of Computed Super Resolution and Magnification Tomosynthesis. In: Flohr TG, Lo JY, Schmidt TG, eds. *Physics of Medical Imaging*. Orlando, FL: SPIE; 2017:1013222-1–1013222-10.
23. Acciavatti RJ, Rodríguez-Ruiz A, Vent TL, et al. Analysis of Volume Overestimation Artifacts in the Breast Outline Segmentation in Tomosynthesis. In: Lo JY, Schmidt TG, Chen G-H, eds. *Physics of Medical Imaging*. Houston, TX: SPIE; 2018:1057359-1–1057359-8.
24. Choi CJ, Vent TL, Acciavatti RJ, Maidment ADA. Geometric Calibration for a Next-Generation Digital Breast Tomosynthesis System Using Virtual Line Segments. In: Lo JY, Schmidt TG, Chen G-H, eds. *Physics of Medical Imaging*. Houston, TX: SPIE; 2018:105730D-1–105730D-10.
25. Eben JE, Vent TL, Choi CJ, et al. Development of a Next Generation Tomosynthesis System. In: Lo JY, Schmidt TG, Chen G-H, eds. *Physics of Medical Imaging*. Houston, TX: SPIE; 2018:105735Q-1–105735Q-8.
26. Johns PC, Yaffe MJ. X-ray characterization of normal and neoplastic breast tissues. *Phys Med Biol*. 1987;32:675–695.
27. Yaffe MJ. Chapter 5: digital mammography. In: Beutel J, Kundel HL, Metter RLV, eds. *Handbook of Medical Imaging Volume 1 Physics and Psychophysics*. Bellingham, WA: SPIE - The International Society for Optical Engineering; 2000. 329–372.
28. Carton A-K, Li J, Chen SC, Conant EF, Maidment ADA. Optimization of contrast-enhanced digital breast tomosynthesis. In: Astley SM, Brady M, Rose C, Zwiggelaar R, eds. *Digital Mamography*. Vol. 4046. Lecture Notes in Computer Science. Berlin: Springer; 2006:183–189.
29. Chen SC, Carton AK, Albert M, Conant EF, Schnall MD, Maidment ADA. Initial clinical experience with contrast-enhanced digital breast tomosynthesis. *Acad Radiol*. 2007;14:229–238.
30. Fredenberg E, Hemmendorff M, Cederstrom B, Aslund M, Danielsson M. Contrast-enhanced spectral mammography with a photon-counting detector. *Med Phys*. 2010;37:2017–2029.
31. Carton AK, Gavenonis SC, Currivan JA, Conant EF, Schnall MD, Maidment ADA. Dual-energy contrast-enhanced digital breast tomosynthesis - a feasibility study. *Br J Radiol*. 2010;83:344–350.
32. Carton A-K, Ullberg C, Lindman K, Acciavatti R, Francke T, Maidment ADA. Optimization of a dual-energy contrast-enhanced technique for a photon-counting digital breast tomosynthesis system: I. A theoretical model. *Med Phys*. 2010;37:5896–5907.
33. Carton A-K, Ullberg C, Maidment ADA. Optimization of a dual-energy contrast-enhanced technique for a photon-counting digital breast tomosynthesis system: II. An experimental validation. *Med Phys*. 2010;37:5908–5913.
34. Lau KC, Acciavatti RJ, Maidment ADA. Estimating breast thickness for dual-energy subtraction in contrast-enhanced digital mammography: a theoretical model. In: Tingberg A, Lång K, Timberg P, eds. *Breast Imaging*. Vol. 9699. Lecture Notes in Computer Science. Berlin: Springer; 2016:593–600.
35. Lau KC, Kwon YJ, Aziz MK, Acciavatti RJ, Maidment ADA. Estimating breast thickness for dual-energy subtraction in contrast-enhanced digital mammography using calibration phantoms. In: Kontos D, Flohr TG, Lo JY, eds. *Physics of Medical Imaging*. San Diego, CA: SPIE; 2016:978307-1–978307-12.
36. Puong S, Patoureaux F, Iordache R, Bouchevreau X, Muller S. Dual-energy contrast enhanced digital breast tomosynthesis: concept, method and evaluation on phantoms. In: Hsieh J, Flynn MJ, eds. *Physics of Medical Imaging*. San Diego, CA: SPIE; 2007:65100U-1–65100U-12.
37. Puong S, Bouchevreau X, Duchateau N, Iordache R, Muller S. Optimization of beam parameters and iodine quantification in Dual-Energy Contrast Enhanced Digital Breast Tomosynthesis. In: Hsieh J, Samei E, eds. *Physics of Medical Imaging*. San Diego, CA: SPIE; 2008:69130Z-1–69130Z-11.
38. Maidment ADA. Virtual clinical trials for the assessment of novel breast screening modalities. In: Fujita H, Hara T, Muramatsu C, eds. *Breast Imaging*. Lecture Notes in Computer Science. Vol. 8539. Berlin: Springer;2014:1–8.
39. Sechopoulos I. A review of breast tomosynthesis. Part I. The image acquisition process. *Med Phys*. 2013;40:014301-1–014301-12.
40. Acciavatti RJ, Maidment ADA. Investigating the Potential for Super-Resolution in Digital Breast Tomosynthesis. In: Pelc NJ, Samei E, Nishikawa RM, eds. *Physics of Medical Imaging*. Lake Buena Vista, FL: SPIE; 2011:79615K-1–79615K-12.
41. Acciavatti RJ, Maidment ADA. Optimization of Continuous Tube Motion and Step-and-Shoot Motion in Digital Breast Tomosynthesis Systems with Patient Motion. In: Pelc NJ, Nishikawa RM, Whiting BR, eds. *Physics of Medical Imaging*. San Diego, CA: SPIE; 2012:831306-1–831306-12.
42. Zhao B, Zhao W. Three-dimensional linear system analysis for breast tomosynthesis. *Med Phys*. 2008;35:5219–5232.
43. Johns HE, Cunningham JR. *The Physics of Radiology.* Chapter 16: Diagnostic Radiology, 4th ed. Springfield, IL: Charles C Thomas; 1983:557–669.

SUPPORTING INFORMATION

Additional supporting information may be found online in the Supporting Information section at the end of the article.

Data S1. Closed-form solutions for the net PSF in Case 2 (Section 2.C.2.) and Case 3 (Section 2.C.3.) are derived.

Nonstationary model of oblique x-ray incidence in amorphous selenium detectors: II. Transfer functions

Raymond J. Acciavatti[a)] and Andrew D. A. Maidment
Department of Radiology, Perelman School of Medicine at the University of Pennsylvania, Philadelphia, PA 19104-4206, USA

(Received 23 April 2018; revised 2 October 2018; accepted for publication 16 November 2018; published 11 January 2019)

Purpose: One limitation of experimental techniques for quantifying resolution and noise in detectors is that the measurement is made in a region-of-interest (ROI). With theoretical modeling, these properties can be measured at a point, allowing for quantification of spatial anisotropy. This paper calculates nonstationary transfer functions for amorphous selenium (*a*-Se) detectors in breast imaging. We use this model to demonstrate the performance advantage of a "next-generation" tomosynthesis (NGT) system, which is capable of x-ray source motion with more degrees of freedom than a clinical tomosynthesis system.

Methods: Using Swank's formulation, the optical transfer function (OTF) and presampled noise power spectra (NPS) are determined based on the point spread function derived in Part 1. The modulation transfer function (MTF) is found from the normalized modulus of the OTF. To take into account the presence of digitization, the presampled NPS is convolved with a two-dimensional comb function, for which the period along each direction is the reciprocal of the detector element size. The detective quantum efficiency (DQE) is then determined from combined knowledge of the OTF and NPS.

Results: First, the model is used to demonstrate the loss of image quality due to oblique x-ray incidence. The MTF is calculated along various polar angles, corresponding to different orientations of the input frequency. The MTF is independent of the incidence angle if the polar angle is perpendicular to the ray incidence direction. However, along other polar angles, oblique incidence results in MTF degradation at high frequencies. The MTF degradation is most substantial along the ray incidence direction. Unlike the MTF, the normalized NPS (NNPS) is independent of the incidence angle. To measure the relative signal-to-noise, the DQE is also calculated. Oblique incidence yields high-frequency DQE degradation, which is more pronounced than the MTF degradation. This arises because the DQE is proportionate with the square of the MTF. Ultimately, this model is used to evaluate how the image quality varies over the detector area. For various projection images, we calculate the variation in the incidence angle over this area. With the NGT system, the source can be positioned in such a way that this variation is minimized, and hence the DQE exhibits less anisotropy. To achieve this improvement in the image quality, the source needs to have a component of motion in the posteroanterior (PA) direction, which is perpendicular to the conventional direction of source motion in tomosynthesis.

Conclusions: In *a*-Se detectors, the DQE at high frequencies is degraded due to oblique incidence. The DQE degradation is more pronounced than the MTF degradation. This model is used to quantify the spatial variation in DQE over the detector area. The use of PA source motion is a strategy for minimizing this variation and thus improving the image quality. [https://doi.org/10.1002/mp.13312]

Key words: amorphous selenium, detective quantum efficiency (DQE), digital x-ray detectors, modulation transfer function (MTF), obliquity effect

1. INTRODUCTION

Oblique x-ray incidence is a source of resolution loss in amorphous selenium (*a*-Se) detectors. The loss of resolution can be quantified with the modulation transfer function (MTF). Que and Rowlands used theoretical modeling to derive a closed-form solution for the MTF in *a*-Se detectors.[1] This model was later validated by Hajdok and Cunningham with Monte Carlo simulations.[2] These simulations show that the MTF degradation is pronounced at high energy, since the incident ray is less attenuated as it passes through the x-ray converter.

X-ray experiments in previous works have validated the MTF degradation due to oblique incidence. The MTF was calculated with a digital breast tomosynthesis (DBT) system using a tungsten edge.[3,4] Previous works have also shown that increasing the thickness of selenium results in more substantial MTF degradation.[3,5] This arises because the incident ray traverses a broader path length through the x-ray converter, yielding more blurring.

The purpose of this paper is to develop a nonstationary model of the MTF in *a*-Se detectors. This model is used to quantify the spatial variation in the image quality across the detector area. One limitation of experimental methods[6–9] used to measure MTF is that spatial anisotropy cannot be quantified, since it is presumed that the MTF is stationary within a region-of-interest (ROI). We calculate the MTF using the model of the point spread function (PSF) developed in Part 1.[10] This model includes the effects of the divergent-beam geometry and digitization.

Unlike the MTF, the NPS is effectively independent of the incidence angle in *a*-Se detectors. This result was demonstrated by Hajdok and Cunningham with Monte Carlo simulations.[2] Hu et al. reached a similar conclusion in an experimental study.[3] Based on the MTF and NPS results, it has been shown that the detective quantum efficiency (DQE) is degraded by oblique incidence. The DQE is proportionate with the square of the MTF, and hence, the DQE degradation is more pronounced than the MTF degradation.[2]

Ultimately, this model is used to demonstrate the performance advantage of a prototype "next-generation" tomosynthesis (NGT) system, which we are developing at the University of Pennsylvania.[11–16] This system is capable of x-ray source motion with more degrees of freedom than a clinical DBT system. Our previous work showed that the NGT system offers an improvement in image quality using the Defrise phantom.[13,16] This paper analyzes how the DQE varies over the detector area in different projection views supported by the NGT system. We demonstrate that the source can be positioned in such a way that there is less pronounced variation in DQE, and hence, the image quality is more isotropic.

2. MATERIALS AND METHODS

2.A. Modulation transfer function (MTF)

2.A.1 X-ray converter

To determine the MTF of the x-ray converter, it is first necessary to calculate the two-dimensional (2D) Fourier transform of P_{I}; that is, the PSF associated with the interaction point at the height z above the exit surface of the x-ray converter

$$\mathcal{F}_2 P_{\mathrm{I}} = \int_{-\infty}^{\infty}\int_{-\infty}^{\infty} P_{\mathrm{I}} \cdot e^{-2\pi i\left(f_x x + f_y y\right)} dxdy \tag{1}$$

where $i = \sqrt{-1}$ and where f_x and f_y measure the frequency along the x and y directions, respectively. This integral can be transformed from the (x, y) coordinate system into the (v'_1, v'_2) coordinate system using the equations of Part 1.[10]

$$\mathcal{F}_2 P_{\mathrm{I}} = \int_{-\infty}^{\infty}\int_{-\infty}^{\infty} \delta[v'_1 - (l-z)\tan\theta]\delta(v'_2) \cdot e^{-2\pi i\left[f_x(\xi_1 + v'_1\cos\Gamma - v'_2\sin\Gamma) + f_y(\xi_2 + v'_1\sin\Gamma + v'_2\cos\Gamma)\right]} dv'_1 dv'_2 \tag{2}$$

$$\mathcal{F}_2 P_{\mathrm{I}} = \int_{-\infty}^{\infty}\int_{-\infty}^{\infty} \delta\left[v'_1 - \frac{r(l-z)}{d-l}\right]\delta(v'_2) \cdot e^{-2\pi i\left[f_x\left(\xi_1 + v'_1\frac{\xi_1}{r} - v'_2\frac{\xi_2}{r}\right) + f_y\left(\xi_2 + v'_1\frac{\xi_2}{r} + v'_2\frac{\xi_1}{r}\right)\right]} dv'_1 dv'_2 \tag{3}$$

$$= e^{-2\pi i\left(\frac{\xi_1 f_x + \xi_2 f_y}{d-l}\right)(d-z)} \tag{4}$$

These equations presume that $r > 0$, as was the case in Part 1.[10] Following Swank,[17] the optical transfer function (OTF) of the x-ray converter is determined by integrating $\mathcal{F}_2 P_{\mathrm{I}}$ over the thickness (l) of selenium, and weighting the integrand by the relative number of x-ray quanta at each depth z.

$$G_{\mathrm{Se}} = \int_0^l N \cdot \mathcal{F}_2 P_{\mathrm{I}} \cdot dz \tag{5}$$

$$= C_{\mathrm{I}} e^{\frac{-2\pi i d\left(\xi_1 f_x + \xi_2 f_y\right)}{d-l}} \int_0^l e^{-\mu(l-z)\sqrt{1+\left(\frac{r}{d-l}\right)^2} + \frac{2\pi i\left(\xi_1 f_x + \xi_2 f_y\right)}{d-l} z} dz \tag{6}$$

$$= \frac{e^{-2\pi i\left(\xi_1 f_x + \xi_2 f_y\right)}}{1 - e^{-\mu l\sqrt{1+\left(\frac{r}{d-l}\right)^2}}} \left[\frac{1 - e^{-\mu l\sqrt{1+\left(\frac{r}{d-l}\right)^2} + \frac{-2\pi i\left(\xi_1 f_x + \xi_2 f_y\right) l}{d-l}}}{1 + \frac{2\pi i\left(\xi_1 f_x + \xi_2 f_y\right)}{\mu r\sqrt{1+\left(\frac{d-l}{r}\right)^2}}}\right] \tag{7}$$

The MTF of the x-ray converter can be determined from the normalized modulus of the OTF

$$\mathrm{MTF}_{\mathrm{Se}} = \frac{|G_{\mathrm{Se}}|}{G_{\mathrm{Se}}|_{\mathbf{f}=\mathbf{0}}} \tag{8}$$

where $\mathbf{f}$ denotes the doublet with components f_x and f_y.

2.A.2. Digital system

Analogous to Eq. (5), the net OTF of the digital system can be calculated by replacing P_{I} with P_z.

$$G_{\mathrm{Net}} = \int_0^l N \cdot \mathcal{F}_2 P_z \cdot dz \tag{9}$$

Since P_z is a convolution of two functions [Eq. (11), Acciavatti and Maidment[10]], the 2D Fourier transform can be evaluated using the convolution theorem

$$\mathcal{F}_2 P_z = \mathcal{F}_2 P_{\mathrm{I}} \cdot \mathcal{F}_2 P_{\mathrm{TFT}} \tag{10}$$

where

$$\mathcal{F}_2 P_{\mathrm{TFT}} = \mathrm{sinc}(a_x f_x) \cdot \mathrm{sinc}(a_y f_y) \tag{11}$$

and where

$$\mathrm{sinc}(v) \equiv \frac{\sin(\pi v)}{\pi v} \tag{12}$$

Hence,

$$G_{\mathrm{Net}} = \mathcal{F}_2 P_{\mathrm{TFT}} \cdot \int_0^l N \cdot \mathcal{F}_2 P_{\mathrm{I}} \cdot dz \tag{13}$$

$$= \mathcal{F}_2 P_{\mathrm{TFT}} \cdot G_{\mathrm{Se}} \tag{14}$$

The MTF of the digital system can be determined with a normalization formula similar to the one described by Eq. (8) for the x-ray converter. In the special case of normal incidence ($r = 0$), G_{Se} is unity since there is no loss of image quality; hence, G_{Net} is given by 2D Fourier transform of P_{TFT} [Eq. (11)].

2.B. Normalized noise power spectra (NNPS)

2.B.1. X-ray converter

The NPS of the x-ray converter can be calculated from P_{I}, the PSF associated with each interaction point in selenium. Since the Fourier transform of P_{I} has a modulus of unity, the NPS is white (i.e., frequency-independent) at all incidence angles.

$$W_{\mathrm{Se}} = \int_0^l N \cdot |\mathcal{F}_2 P_{\mathrm{I}}|^2 \cdot dz \tag{15}$$

$$= \int_0^l N \cdot 1^2 \cdot dz \tag{16}$$

$$= 1 \tag{17}$$

The notation "W" comes from the alternate NPS term "Wiener spectra."[18] Eqs. (15)–(17) represent the normalized NPS (NNPS), as there is no weighting based on the x-ray fluence.[19,20]

2.B.2. Digital system

In the digital system, the presampled NPS is calculated with the same approach, but P_{I} is replaced with P_z to take into account the presence of the TFT array.

$$W_{\mathrm{Pre}} = \int_0^l N \cdot |\mathcal{F}_2 P_z|^2 \cdot dz \tag{18}$$

$$= \int_0^l N \cdot |\mathcal{F}_2 P_{\mathrm{I}}|^2 \cdot |\mathcal{F}_2 P_{\mathrm{TFT}}|^2 \cdot dz \tag{19}$$

$$= |\mathcal{F}_2 P_{\mathrm{TFT}}|^2 \cdot \int_0^l N \cdot 1^2 \cdot dz \tag{20}$$

$$= |\mathcal{F}_2 P_{\mathrm{TFT}}|^2 \tag{21}$$

Previous work demonstrated that the digital NPS is found by convolving W_{Pre} with a 2D comb function. The period of the comb function is a_x^{-1} in the x direction and a_y^{-1} in the y direction, where a_x and a_y are the del dimensions in the two respective directions.

$$W_{\mathrm{Net}}(f_x, f_y) = \sum_{k_y=-\infty}^{\infty} \sum_{k_x=-\infty}^{\infty} W_{\mathrm{Pre}} *_2 \delta\left(f_x - \frac{k_x}{a_x}\right)\delta\left(f_y - \frac{k_y}{a_y}\right) \tag{22}$$

$$= \sum_{k_y=-\infty}^{\infty} \sum_{k_x=-\infty}^{\infty} \mathrm{sinc}^2(a_x f_x) \cdot \mathrm{sinc}^2(a_y f_y) *_2 \delta\left(f_x - \frac{k_x}{a_x}\right)\delta\left(f_y - \frac{k_y}{a_y}\right) \tag{23}$$

$$= \sum_{k_x=-\infty}^{\infty} \mathrm{sinc}^2\left[a_x\left(f_x - \frac{k_x}{a_x}\right)\right] \cdot \sum_{k_y=-\infty}^{\infty} \mathrm{sinc}^2\left[a_y\left(f_y - \frac{k_y}{a_y}\right)\right] \tag{24}$$

$$= 1 \tag{25}$$

The transition from Eq. (24) to Eq. (25) follows from an identity described in our previous work.[20] Eq. (25) indicates that the NNPS of the digital system is white, just as the NNPS of the x-ray converter is white.

2.C. Detective quantum efficiency (DQE)

Following Nishikawa and Yaffe,[21] the DQE is calculated from the product of four terms

$$\mathrm{DQE} = A_{\mathrm{Q}} A_{\mathrm{S}} R_{\mathrm{C}} R_{\mathrm{N}}, \tag{26}$$

where A_{Q} is the quantum detection efficiency (QDE).

$$A_{\mathrm{Q}} = \left(1 - e^{-\mu l \sec\theta}\right)\cos\theta \tag{27}$$

$$= \frac{1 - e^{-\mu l \sqrt{1 + \left(\frac{r}{d-l}\right)^2}}}{\sqrt{1 + \left(\frac{r}{d-l}\right)^2}} \tag{28}$$

In Eq. (27), the quantity in parentheses is the percentage of x rays that are absorbed based on the attenuation coefficient (μ) of selenium. The term $\cos\theta$ models the degradation in x-ray fluence with increasing obliquity, which approaches zero at shearing incidence ($\theta = 90°$).

Second, A_{S} is the Swank factor[17,22]; it measures the relative signal-to-noise at zero frequency.

$$A_{\mathrm{S}} = \frac{G^2|_{\mathbf{f}=\mathbf{0}}}{W|_{\mathbf{f}=\mathbf{0}}} \tag{29}$$

Since this formula applies to both the x-ray converter and the digital system, the subscripts "Se" and "Net" are being removed from the terms G and W.

Third, the term R_{C} is the Lubberts fraction; it quantifies the frequency dependence of the DQE.

$$R_{\mathrm{C}} = \frac{1}{A_{\mathrm{S}}} \cdot \frac{|G|^2}{W} \tag{30}$$

Finally, the term R_N is a relative measure of quantum noise power to total noise power. For the purpose of this paper, it is assumed that R_N is unity at all frequencies.

3. RESULTS

3.A. Calculation of MTF

3.A.1. Low x-ray energy

We model the NGT system[11–16] with the same acquisition parameters as those described in Part 1[10] for a digital mammography (DM) image (analogous to the central projection in DBT). To calculate the MTF along any polar angle (α), a coordinate transformation can be introduced

$$f_x = f_r \cos\alpha \tag{31}$$

$$f_y = f_r \sin\alpha, \tag{32}$$

where f_r denotes radial frequency. Figures 1(a) and 2(a) illustrate how the MTF at 15° incidence varies with radial frequency at an energy of 20 keV. The two plots differ in terms of the azimuthal angle (Γ) of the ray; that is, 90° in Fig. 1(a) and 45° in Fig. 2(a). The detector positions corresponding to these angles were illustrated in Part 1 (Acciavatti and Maidment,[10] Figs. 3 and 6).

In a non-pixelated system, the MTF is perfect (1.0 at all frequencies) if the polar angle is perpendicular to the ray incidence direction; that is, 0° in Fig. 1(a) and 135° in Fig. 2(a). However, there is loss of resolution along the other polar angles, as one would expect.

It is also shown that the digital system has lower MTF than the x-ray converter. At a 0° or 90° polar angle, $\mathrm{MTF}_{\mathrm{Net}}$ is zero at the frequency a^{-1} (11.8 mm^{-1}). By contrast, along 45° or 135° polar angles, the zero increases by a factor of $\sqrt{2}$, giving 16.6 mm^{-1}. These zeros are not dependent on the parameter Γ, which controls the direction of ray incidence.

3.A.2. High x-ray energy

At high energy, the x-ray beam is attenuated less quickly as it passes through the x-ray converter. As a result, the MTF degradation due to the obliquity effect is more pronounced [Figs. 1(b) and 2(b)]. This finding is consistent with previous work.[2]

The plots at high energy show Gibbs ringing,[23] unlike the plots at low energy. This result is concordant with the work of Que and Rowlands,[1] who demonstrated that the frequency span of the MTF can be determined from the equation

$$f_g = \max\left\{(l\tan\theta)^{-1}, \mu\csc\theta\right\} \tag{33}$$

At 20 keV, f_g is so large (78.2 mm^{-1}) that it exceeds the frequency range of the plot. However, at 40 keV, f_g is 18.7 mm^{-1}. This frequency is a perfect match to the local minimum if the polar angle (α) is aligned with the ray incidence direction; that is, 90° in Fig. 1(b) and 45° in Fig. 2(b). If the polar angle is at a 45° angle relative to the ray incidence direction, this frequency is scaled up by a factor of $\sqrt{2}$, giving 26.4 mm^{-1}.

3.A.3. Dependency on incidence angle

Figure 3 illustrates how the MTF is degraded as a function of the incidence angle, assuming that f_r = 5.0 mm^{-1} and Γ = 90°. The incidence angle is varied by increasing the distance from the chest wall along the $+y$ direction. This plot presumes that the x-ray energy is 20 keV, as is the case in all subsequent plots unless explicitly stated. The MTFs are shown for both a digital and a non-pixelated system. The MTFs of these two systems differ by a constant factor, which is given by the MTF of the detector sampling function [Eq. (11)].

If frequency is perpendicular to the ray incidence direction (α = 0°), the MTF is independent of the incidence angle. However, there is MTF degradation along the other polar angles. The most pronounced resolution loss is seen along the 90° polar angle (parallel to the ray incidence direction).

To generalize Fig. 3 to more than one frequency, Fig. 4 shows the MTF at 20 keV as a function of both incidence angle and frequency. This figure presumes that $\Gamma = \alpha$ = 90°, so the polar angle is aligned with the ray incidence direction. Frequencies up to the alias frequency $0.5a^{-1}$ (5.88 mm^{-1})

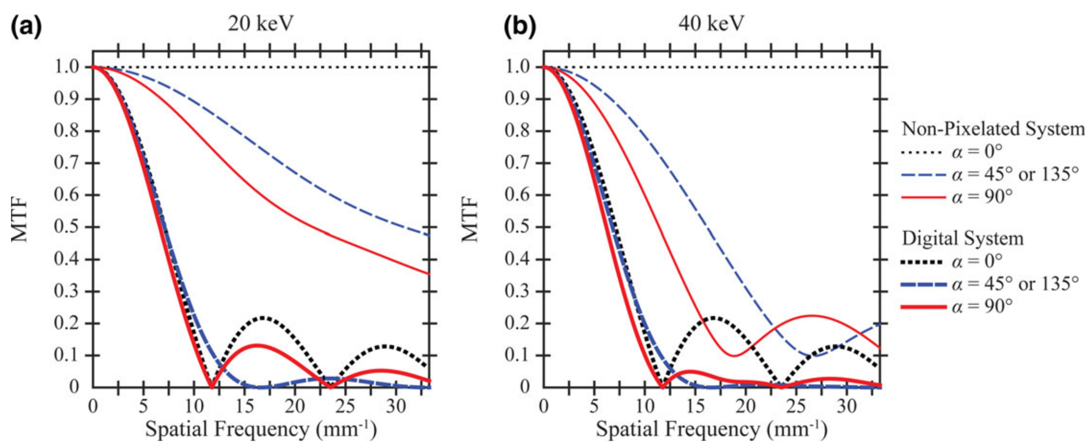

FIG. 1. The MTF at 15° incidence is plotted as a function of frequency. The ray incidence direction is at a 90° azimuthal angle (Γ), so the most MTF degradation is seen along this direction. The MTF degradation is more pronounced at high energy. [Color figure can be viewed at wileyonlinelibrary.com]

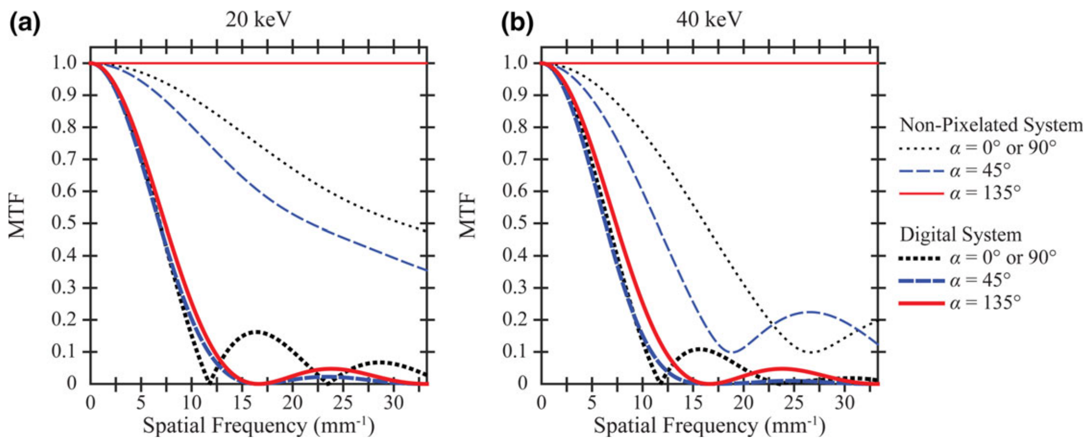

FIG. 2. The MTF is calculated under assumptions similar to Fig. 1, but the azimuthal angle (Γ) is 45°. Along the perpendicular direction (α = 135°), there is no MTF degradation due to oblique incidence. [Color figure can be viewed at wileyonlinelibrary.com]

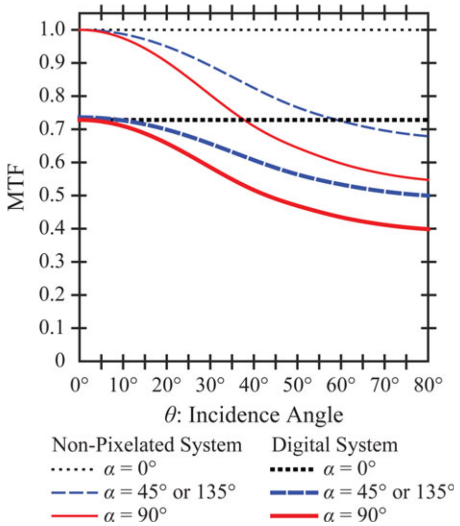

FIG. 3. For a 20 keV x-ray beam, the MTF at 5.0 mm^{-1} is plotted as a function of the incidence angle, assuming Γ = 90°. The MTF is unaffected by oblique incidence if frequency is measured along the polar angle perpendicular to the ray incidence direction (α = 0°). However, the MTF is degraded by oblique incidence along the other polar angles shown. [Color figure can be viewed at wileyonlinelibrary.com]

are considered. At low obliquity ($\theta \sim 0°$), the MTF of a non-pixelated system [Fig. 4(a)] is effectively constant, yet the MTF of a digital system [Fig. 4(b)] is degraded at high frequencies. As the incidence angle increases, both the non-pixelated and digital systems show MTF degradation at high frequencies.

3.B. Calculation of DQE

3.B.1. Effect of x-ray energy and polar angle

Under assumptions similar to Figs. 1 and 2, the DQE is plotted as a function of frequency in Figs. 5 and 6. Following the approach used in previous work, the DQE is plotted up to the alias frequency.[20,24] Along the 0° and 90° polar angles, the alias frequency is $0.5a^{-1}$ (5.88 mm^{-1}). By contrast, along the 45° and 135° polar angles, the alias frequency increases by a factor of $\sqrt{2}$, giving 8.32 mm^{-1}.

Using Eq. (29) and the equations for OTF and NPS, it can be shown that the Swank factor (A_S) is unity for both the non-pixelated and digital systems. Therefore, the DQE at zero-frequency is equivalent to A_Q (the QDE); namely, 0.951 at 20 keV and 0.449 at 40 keV. There is lower DQE at high energy, since fewer x rays are absorbed by the detector. These results hold for both the non-pixelated and digital systems.

The DQE degradation is most pronounced along the polar angle aligned with the ray incidence direction; that is, 90° in Fig. 5 and 45° in Fig. 6. These are consistent with the polar angles corresponding to the most pronounced MTF degradation.

In a non-pixelated system, the DQE is not degraded along the polar angle perpendicular to the ray incidence direction. This arises because the MTF and NNPS of the x-ray converter are independent of frequency along this direction. By contrast, in the digital system, the DQE is frequency-dependent along all polar angles.

It should be noted that digitization introduces electronic noise not modeled in this paper. Based on our previous work,[20] including this noise source in the model would rescale the curves in Figs. 5 and 6 by a constant factor, reducing the DQE.

3.B.2. Obliquity effect

Figure 7 shows the dependency of DQE on incidence angle (under similar assumptions as Fig. 3). Oblique incidence results in DQE degradation along all polar angles. This includes the polar angle perpendicular to the ray incidence direction (α = 0°), even though there is no MTF degradation along this direction. To understand why there is DQE degradation along this direction, it is important to recall the QDE formula [Eq. (27)]. The formula consists of two terms. The term $\left(1 - e^{-\mu l \sec\theta}\right)$ is an increasing function of the incidence

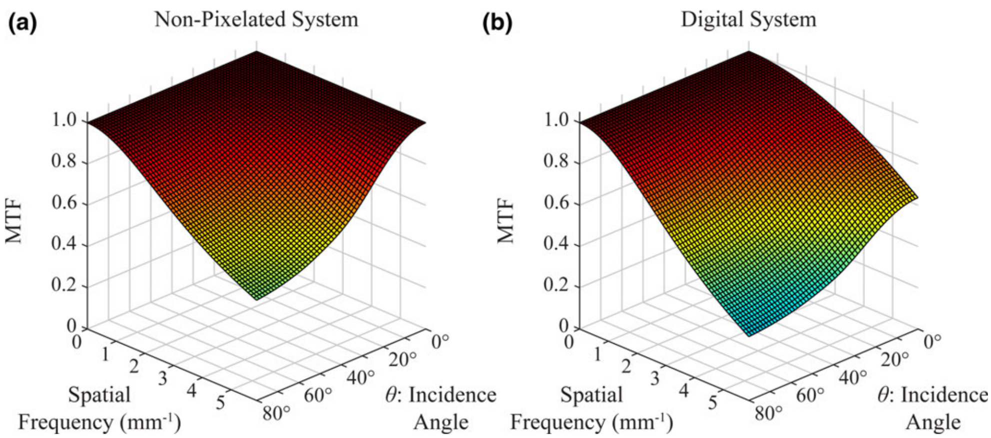

FIG. 4. The MTF at 20 keV is plotted as a function of both the incidence angle and frequency, assuming that $\Gamma = \alpha = 90°$. At low frequency, the MTF is effectively independent of the incidence angle. However, at high frequency, the MTF is more strongly dependent on the incidence angle. [Color figure can be viewed at wileyonlinelibrary.com]

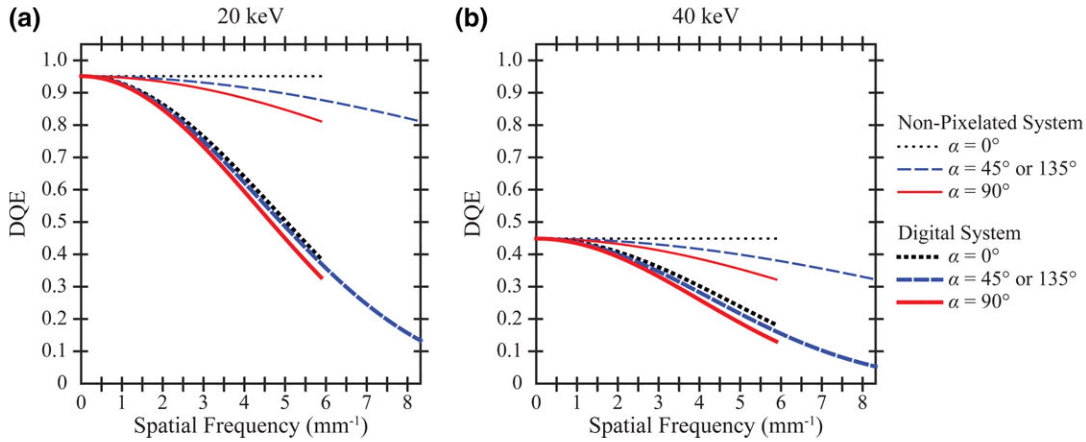

FIG. 5. The DQE is calculated under assumptions similar to Fig. 1; that is, $\Gamma = 90°$. Unlike the DQE of the x-ray converter, the DQE of the digital system is frequency-dependent along all polar angles, including the polar angle perpendicular to the ray incidence direction ($\alpha = 0°$). Increasing the energy results in less x-ray absorption and hence lower DQE. [Color figure can be viewed at wileyonlinelibrary.com]

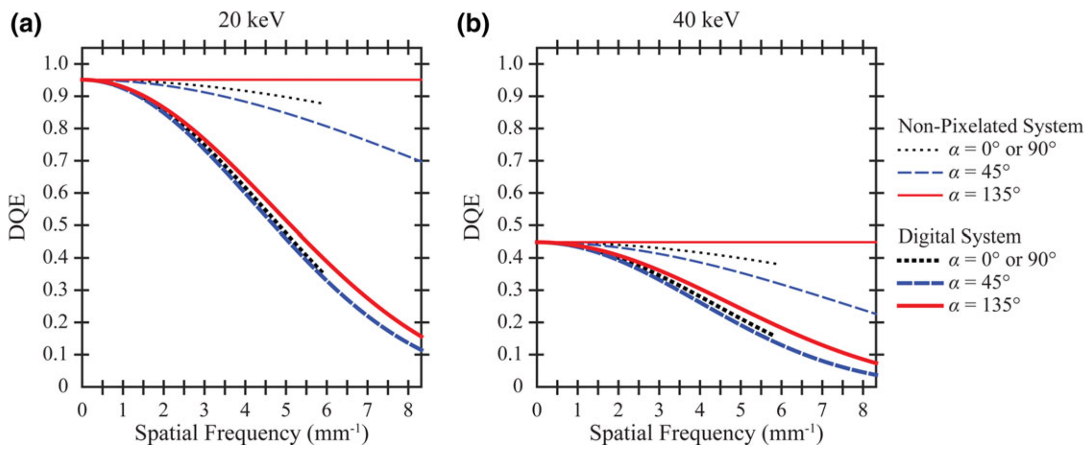

FIG. 6. The DQE is calculated under assumptions similar to Fig. 2. Hence, the direction corresponding to the most DQE degradation is aligned with the 45° polar angle (α). [Color figure can be viewed at wileyonlinelibrary.com]

angle; yet, the term $\cos\theta$ is a decreasing function. The latter term has a more dominant effect on QDE.

Figure 7 also illustrates that the DQE is degraded by oblique incidence more strongly than the MTF. The DQE degradation is most pronounced along the ray incidence direction (α = 90°); for example, at 15° incidence, the percent change in MTF relative to normal incidence is 5.6%, yet the percent change in DQE is 13.7%. These percent differences are the same for both the x-ray converter and the digital system.

Figure 8 is an extension of Fig. 7 to a broader range of frequencies, assuming that frequency is measured along the ray incidence direction. At low frequency ($f \sim 0$ mm^{-1}), the DQE is given by the QDE and thus is degraded by oblique incidence. This differs from the MTF (Fig. 4), which is unaffected by oblique incidence at low frequency. At high frequencies, the MTF and DQE are both degraded by oblique incidence, although the DQE degradation is greater.

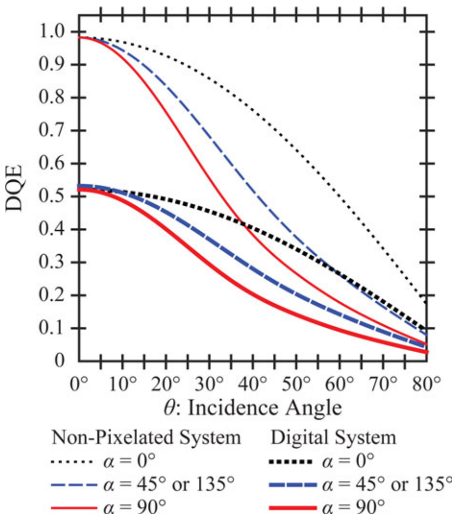

FIG. 7. The DQE is degraded by oblique incidence. Similar to the MTF, the degradation is most pronounced along the ray incidence direction (α = 90°). There is also DQE degradation along the perpendicular direction (α = 0°); this is due to degradation in QDE. The assumptions made in this figure are similar to Fig. 3. [Color figure can be viewed at wileyonlinelibrary.com]

3.C. An application in tomosynthesis system design

3.C.1. Acquisition geometry

We now explore how the obliquity effect gives rise to spatial variation in image quality. This calculation is used to demonstrate an advantage of the NGT design; namely, that the image quality shows less spatial anisotropy.

In the NGT system, the source is capable of arbitrary motions in a plane parallel to the breast support; for example, T-shaped motion (Fig. 9). This motion includes a component in the conventional scan direction (x). There is also a component of motion in the perpendicular direction (y); that is, the posteroanterior (PA) direction. To demonstrate the advantage of this design, the image quality can be quantified in different projection views.

3.C.2. Spatial anisotropy in the incidence angle

For image quality to be high, the incidence angle should be as close to 0° as possible. Figure 10 illustrates how the incidence angle varies over the active area of the detector (304.64 mm × 239.36 mm) in the central and oblique projection images of a conventional system design. The central projection [Fig. 10(a)] uses the same acquisition geometry considered previously for DM imaging. By contrast, in the oblique projection [Fig. 10(b)], the source is shifted by −100.0 mm in the x direction. The incidence angle increases at positions distal to the (x, y) coordinate of the source. It should be noted that, in the NGT system, the z-coordinate of the source is the same in all projections; this differs from a clinical system, in which there is circular motion in the xz plane.

Figure 11 shows the benefit of introducing source motion in the PA direction. For the purpose of this figure, it is

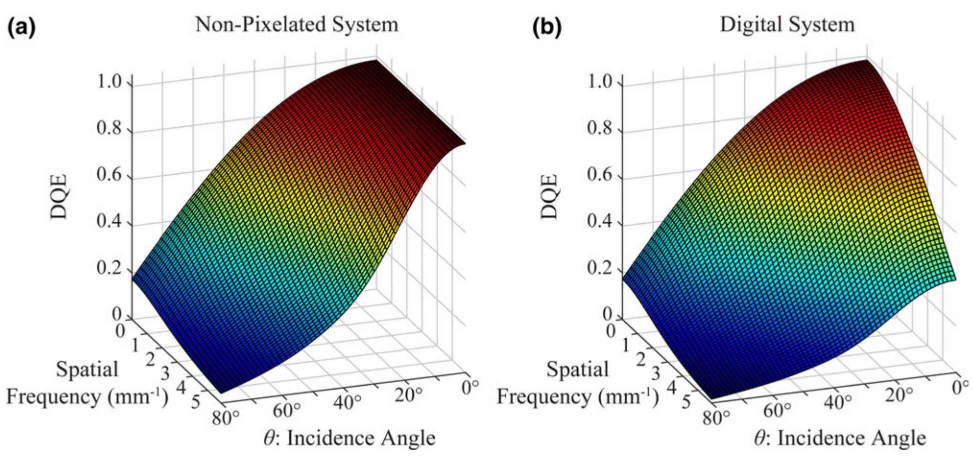

FIG. 8. Figure 7 is generalized to a range of frequencies under assumptions similar to Fig. 4. Increasing the incidence angle results in DQE degradation at all frequencies (including zero-frequency due to loss of QDE). [Color figure can be viewed at wileyonlinelibrary.com]

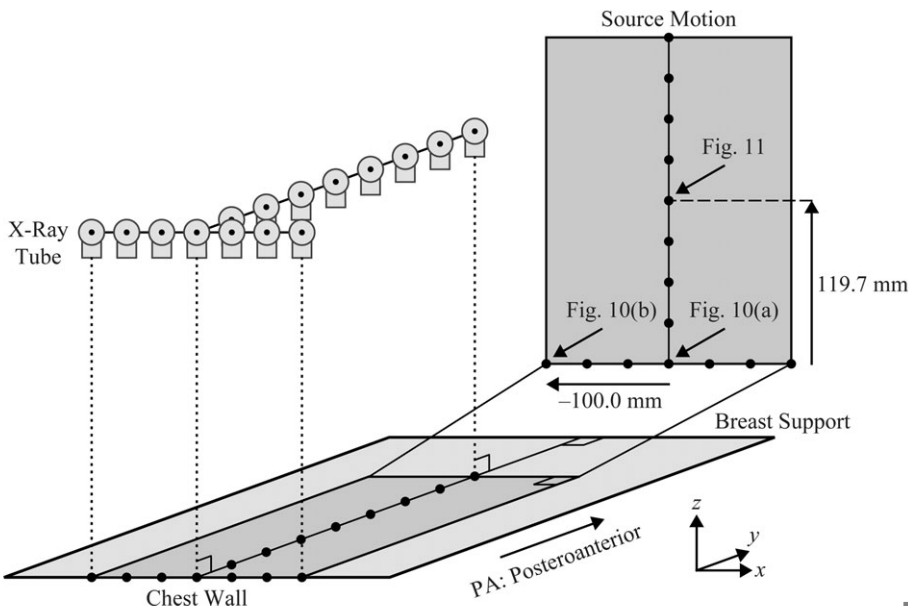

FIG. 9. In the NGT system, there are two degrees of freedom in the motion of the source (x and y). This differs from a clinical DBT system in which there is no source motion in the y direction; that is, posteroanteriorly. An example of a motion supported by the NGT system is T-shaped. This figure is not to scale.

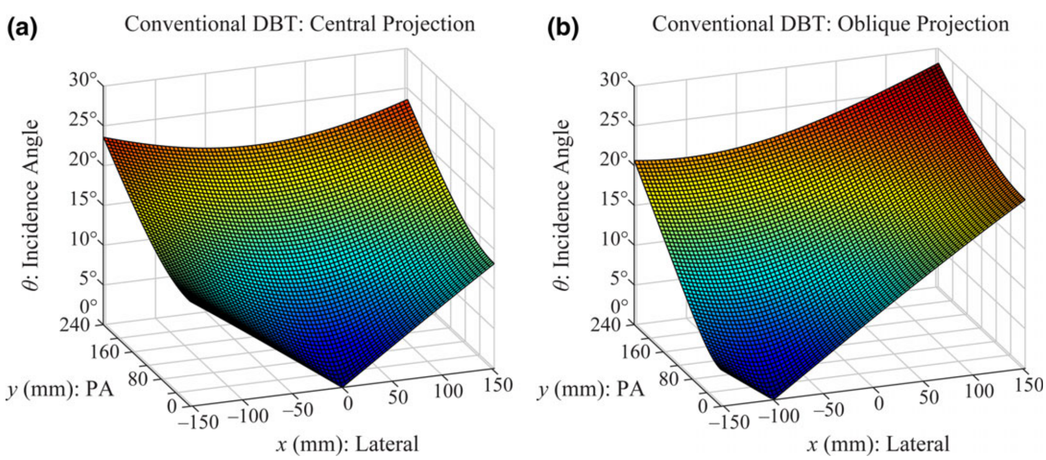

FIG. 10. The incidence angle varies over the detector area. (a) In the central projection of a conventional DBT system, the angle increases up to 23.6°. (b) In the oblique projection, the angle increases up to 28.2°. [Color figure can be viewed at wileyonlinelibrary.com]

assumed that the x-coordinate of the source is the same as the central projection of the conventional design [Fig. 10(a)] but the y-coordinate is displaced halfway between the chest wall and the opposite end of the detector (i.e., 119.7 mm anterior to the chest wall). Compared against the projections in the conventional design, the incidence angle varies over a smaller range of values, and hence one would expect more isotropic image quality across the detector area.

3.C.3. Spatial anisotropy in DQE

Figure 12 illustrates how the net DQE at 5.0 mm^{-1} varies over the detector area for these three projections, assuming 20 keV x rays. For better visualization of the surface, the plots are prepared with a different orientation than Figs. 10 and 11. The benefit of PA source motion (bottom row) is that there is less spatial variation in DQE. This can be illustrated with the results along a 90° polar angle (α). The DQE range (difference between max and min) is 0.13 for the central projection and 0.14 for the oblique projection in the conventional design. Yet, the DQE range is only 0.047 for the projection obtained with PA source motion.

Figure 12 also illustrates how the DQE is sensitive to the polar angle (α) of the input frequency. In the conventional design, the spatial anisotropy is more pronounced along a 45° polar angle (DQE ranges of 0.16 and 0.21 for the central and oblique projections, respectively) than along a 90° polar angle. The use of PA source motion minimizes the anisotropy (DQE range of 0.087).

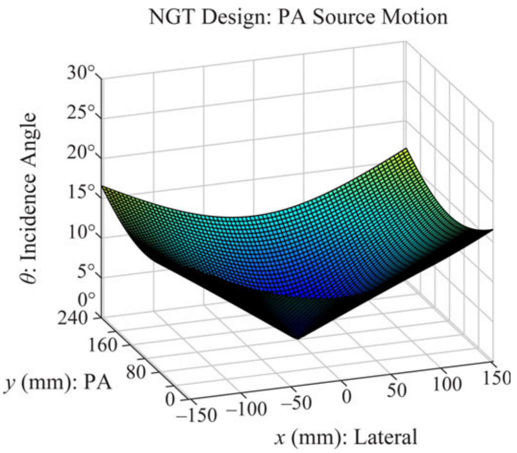

FIG. 11. The NGT system supports PA source motion. There is a smaller range of incidence angles (up to 16.6°) compared against projections obtained with the conventional design (Fig. 10). [Color figure can be viewed at wileyonlinelibrary.com]

4. DISCUSSION

This paper develops a nonstationary model of the obliquity effect in *a*-Se detectors. We show that the MTF is degraded by oblique incidence. This result is consistent with previous works on both direct- and indirect-converting detectors.[1–5,9,25,26] The MTF degradation is most pronounced along the ray incidence direction. There is no MTF degradation along the perpendicular direction. Although these results were illustrated with the AXS-2430 detector, similar results are expected in other detector applications.

We follow the approach used by Que and Rowlands[1] to model the obliquity effect; namely, we consider this effect separate from other x-ray interactions in selenium. With this approach, we find that the NPS is white. Previous work has demonstrated that, at low energy, the NPS is effectively white.[4] However, in high-energy applications, it has been shown that the NPS exhibits more pronounced dependency on frequency.[2–4] This arises from x-ray interactions not included in our model; for example, Compton scattering.[2]

This paper shows that the DQE is degraded by oblique incidence, similar to the MTF. The DQE degradation is most pronounced along the ray incidence direction. The DQE is more strongly dependent on the incidence angle than the MTF, since the DQE is proportionate with the square of the MTF. There is additional DQE degradation due to the dependency of QDE on $\cos\theta$ [Eq. (27)].

In breast imaging, calcifications are high-frequency structures that can act as an early sign of cancer. Based on Monte Carlo simulations of DQE, Hajdok and Cunningham concluded that oblique incidence gives rise to poorer calcification visibility.[2] However, their work is limited in that they did not calculate how the DQE varies over the detector area. Furthermore, they did not model the presence of detector pixelation (i.e., digitization). Our results suggest that calcification visibility does indeed fluctuate over the detector area, and that the image quality at a given detector position differs between projection views (Fig. 12). Exploring the anisotropies in calcification imaging should be the subject of future work.

In the work by Hajdok and Cunningham, the DQE was calculated assuming that frequency is oriented along the ray incidence direction.[2] By contrast, in this paper, the input frequency is modeled along an arbitrary polar angle (α). In studying the spatial variation in DQE, we show that the net DQE variation over the detector area is dependent on the polar angle.

This model is a tool for evaluating the image quality in a prototype NGT system. This system is capable of source motion in the PA direction, unlike a clinical system. In various projection images supported by this system, we analyze how the incidence angle varies over the detector area. The use of PA source motion minimizes the range of angles over this area, and hence anisotropies in the DQE are minimized. This results in an improvement in image quality.

While this paper proposes a model of image quality in an individual projection image, future work should perform these calculations in the reconstruction. In addition, the three-dimensional transfer functions should simulate the reconstruction filter.[27,28]

This paper shows that the Swank factor (A_S) is unity for all incidence angles, and thus the DQE at zero-frequency is determined by the QDE [Eq. (26)]. This result differs from our previous work modeling indirect-converting detectors.[25,26] We demonstrated that A_S does show angular dependence if an optical dye is added to a scintillator. The purpose of the optical dye is to absorb some of the visible light produced by the scintillator, and thus minimize the lateral spread of light due to optical scatter.

As was discussed in Section 3.B.1., electronic noise has not been included in the modeling assumptions of this paper. This noise source re-scales the DQE in Figs. 5 and 6 by a constant factor,[20] resulting in a loss of image quality. While this paper presumes that the x-ray system is quantum-limited, future work should explore additional sources of noise[29] affecting the term R_N in the DQE formula [Eq. (26)].

5. CONCLUSION

In Part 1, the consequences of oblique incidence in *a*-Se detectors were analyzed in the spatial domain.[10] By contrast, this paper focuses on the Fourier domain. We show that there is MTF and DQE degradation resulting from oblique incidence.

This model is ultimately used to quantify spatial variation in image quality over the detector area. We calculate the DQE in projection images supported by the NGT system. The benefit of PA source motion is that it minimizes the spatial variation in DQE, and hence the image quality is more isotropic.

ACKNOWLEDGMENTS

We thank Denny L. Y. Lee for many useful discussions on the physics of *a*-Se detectors. In addition, we

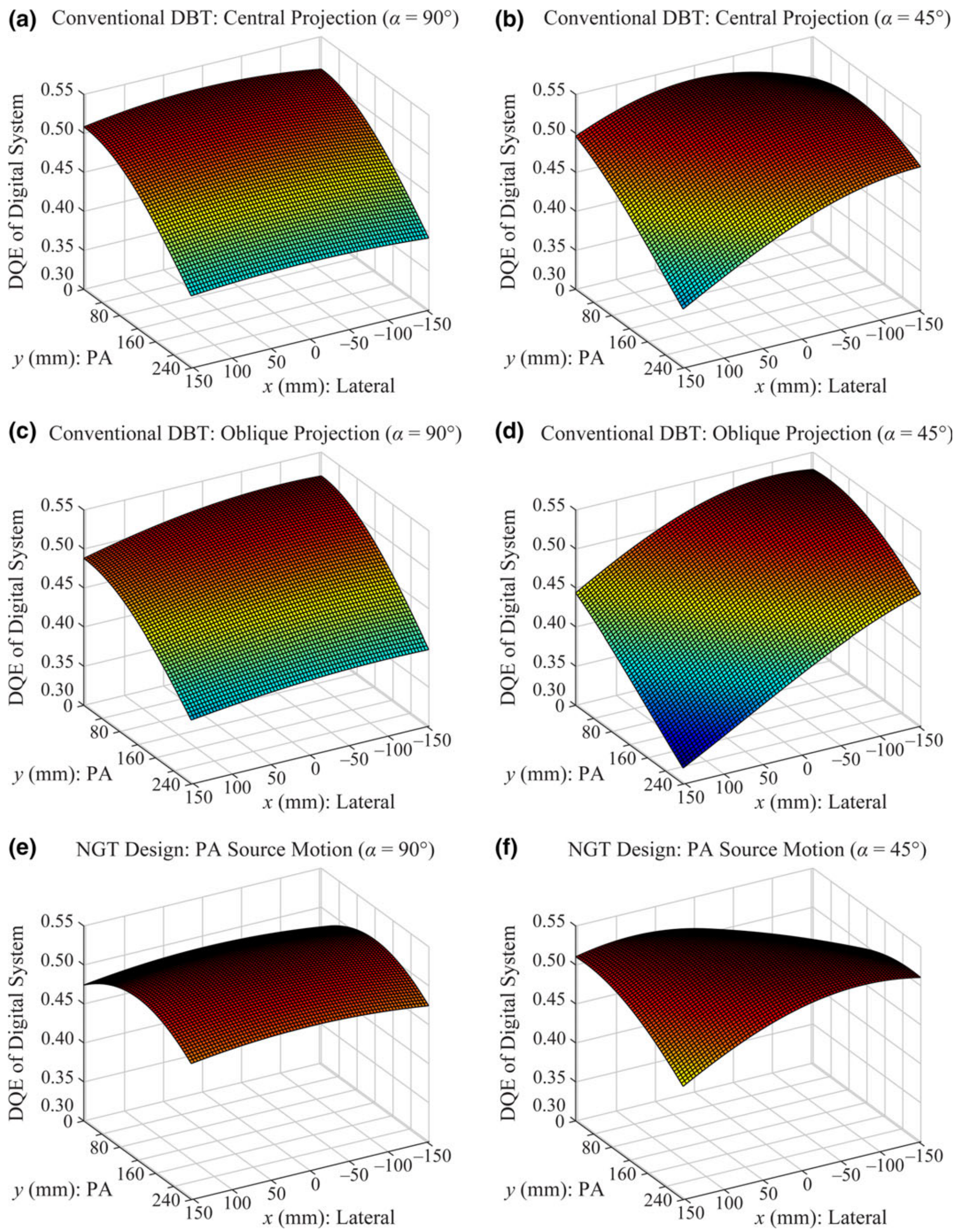

FIG. 12. The net DQE varies over the detector area. With PA source motion (bottom row), there is less pronounced variation and hence more isotropic image quality. The shape of these surface plots is dependent on the polar angle (α) of the input frequency. These calculations presume an input frequency of 5.0 mm^{-1} and an energy of 20 keV. [Color figure can be viewed at wileyonlinelibrary.com]

are grateful to David Higginbotham for providing constructive feedback. Support was provided by the following grants: PDF14302589 and IIR13264610 from Susan G. Komen®; 1R01CA154444 and 1R01CA196528 from the National Institute of Health; IRSA 1016451 from the Burroughs Wellcome Fund; and W81XWH-18-1-0082 from the Department of Defense Breast Cancer Research Program. In addition, equipment support was provided by Analogic Inc., Barco NV, and Real Time Tomography (RTT), LLC (Villanova, PA). The content is solely the responsibility of the authors and does not necessarily represent the official views of the funding agencies.

CONFLICTS OF INTEREST

Andrew D. A. Maidment is a scientific advisor to RTT, and his spouse is an employee and shareholder of RTT.

APPENDIX: NOMENCLATURE

Symbol	Meaning
$*_2$	2D convolution operator
$\mathcal{F}_2$	2D Fourier operator
α	Polar angle (defined in Part 1[10])
Γ	Azimuthal angle of ray (defined in Part 1[10])
δ	Delta function
θ	Incidence angle (defined in Part 1[10])
μ	Linear attenuation coefficient of selenium
ξ_1, ξ_2	Coordinates of entrance point of ray in x-ray converter (defined in Part 1[10])
A_Q	Abbreviation for QDE
A_S	Swank factor
a_x, a_y	Del dimensions; if $a_x = a_y$, the dimension is abbreviated a
C_I	Normalization term for P_I (defined in Part 1[10])
d	Distance between source and exit surface of x-ray converter (defined in Part 1[10])
DBT	Digital breast tomosynthesis
Del	Detector element
DM	Digital mammography
DQE	Detective quantum efficiency
DQE_{Net}	DQE of digital system
DQE_{Se}	DQE of x-ray converter
f_g	Frequency span of MTF [Eq. (33)], as shown by Que and Rowlands[1]
f_r	Radial frequency
f_x, f_y	Frequency along x and y directions
FS	Focal spot
G_{Net}	OTF of digital system
G_{Se}	OTF of x-ray converter
l	Selenium thickness
MTF	Modulation transfer function
MTF_{Net}	MTF of digital system
MTF_{Se}	MTF of x-ray converter
N	Relative number of x-ray quanta (defined in Part 1[10])
NNPS	Normalized NPS
NPS	Noise power spectra
OTF	Optical transfer function
P_I	PSF associated with arbitrary ionization point in x-ray converter
P_{TFT}	PSF of TFT array
P_z	Depth-dependent PSF (combined effect of P_I and P_{TFT})
PA	Posteroanterior
PSF	Point spread function
QDE	Quantum detection efficiency
r	$\sqrt{\xi_1^2 + \xi_2^2}$ as defined in Part 1[10]
R_C	Lubberts fraction
R_N	Ratio of quantum noise power to total noise power
TFT	Thin-film transistor
v'_1	Position along ray incidence direction (defined in Part 1[10])
v'_2	Position perpendicular to ray incidence direction (defined in Part 1[10])
W_{Net}	NNPS of digital system
W_{Pre}	Presampled NNPS
W_{Se}	NNPS of x-ray converter

[a]Author to whom correspondence should be addressed. Electronic mail: raymond.acciavatti@uphs.upenn.edu; Telephone: +1-215-746-8759; Fax: +1-215-746-8764.

REFERENCES

1. Que W, Rowlands JA. X-ray imaging using amorphous selenium: inherent spatial resolution. *Med Phys*. 1995;22:365–374.
2. Hajdok G, Cunningham IA. Penalty on the detective quantum efficiency from off-axis incident x rays. In: Yaffe MJ, Flynn MJ, eds. *Physics of Medical Imaging*. San Diego, CA: SPIE; 2004:109–118.
3. Hu Y-H, Scaduto DA, Zhao W. The effect of amorphous selenium thickness on imaging performance of contrast enhanced digital breast tomosynthesis. *Lect Notes Comput Sci*. 2012;7361:9–16.
4. Scaduto DA, Tousignant O, Zhao W. Experimental characterization of a direct conversion amorphous selenium detector with thicker conversion layer for dual-energy contrast-enhanced breast imaging. *Med Phys*. 2017;44:3965–3977.
5. Hu Y-H, Zhao W. The effect of amorphous selenium detector thickness on dual-energy digital breast imaging. *Med Phys*. 2014;41:111904-1–111904-10.
6. Fujita H, Tsai D-Y, Itoh T, et al. A simple method for determining the modulation transfer function in digital radiography. *IEEE Trans Med Imaging*. 1992;11:34–39.
7. Maidment ADA, Albert M. Conditioning data for calculation of the modulation transfer function. *Med Phys*. 2003;30:248–253.
8. Carton A-K, Vandenbroucke D, Struye L, et al. Validation of MTF measurement for digital mammography quality control. *Med Phys*. 2005;32:1684–1695.
9. Mainprize JG, Bloomquist AK, Kempston MP, Yaffe MJ. Resolution at oblique incidence angles of a flat panel imager for breast tomosynthesis. *Med Phys*. 2006;33:3159–3164.
10. Acciavatti RJ, Maidment ADA. Non-stationary model of oblique X-ray incidence in amorphous-selenium detectors: I. point spread function. *Med Phys*. (in press).
11. Maidment AD, Acciavatti R, Vent T, et al. SSC14-03: Construction of a prototype digital breast tomosynthesis system with superior spatial resolution. Radiological Society of North America (RSNA) Conference, 2016; Chicago, IL.
12. Ferris WS, Vent TL, Maidment TD, Acciavatti RJ, Wurtele DE, Maidment ADA. Geometric calibration for a next-generation digital breast tomosynthesis system. In: Flohr TG, Lo JY, Schmidt TG, eds. *Physics of Medical Imaging*. Orlando, FL: SPIE; 2017:101324C-1–101324C-10.
13. Maidment TD, Vent TL, Ferris WS, Wurtele DE, Acciavatti RJ, Maidment ADA. Comparing the imaging performance of computed super resolution and magnification tomosynthesis. In: Flohr TG, Lo JY, Schmidt TG, eds. *Physics of Medical Imaging*. Orlando, FL: SPIE; 2017:1013222-1–1013222-10.
14. Acciavatti RJ, Rodríguez-Ruiz A, Vent TL, et al. Analysis of volume overestimation artifacts in the breast outline segmentation in tomosynthesis. In: Lo JY, Schmidt TG, Chen G-H, eds. *Physics of Medical Imaging*. Houston, TX: SPIE; 2018:1057359-1–1057359-8.
15. Choi CJ, Vent TL, Acciavatti RJ, Maidment ADA. Geometric calibration for a next-generation digital breast tomosynthesis system using virtual line segments. In: Lo JY, Schmidt TG, Chen G-H, eds. *Physics of Medical Imaging*. Houston, TX: SPIE; 2018:105730D-1–105730D-10.
16. Eben JE, Vent TL, Choi CJ, et al. Development of a next generation tomosynthesis system. In: Lo JY, Schmidt TG, Chen G-H, eds. *Physics of Medical Imaging*. Houston, TX: SPIE; 2018:105735Q-1–105735Q-8.
17. Swank RK. Calculation of modulation transfer functions of x-ray fluorescent screens. *Appl Opt*. 1973;12:1865–1870.
18. Giger ML, Doi K, Metz CE. Investigation of basic imaging properties in digital radiography. 2. Noise Wiener spectrum. *Med Phys*. 1984;11:797–805.
19. Albert M, Maidment ADA. Linear response theory for detectors consisting of discrete arrays. *Med Phys*. 2000;27:2417–2434.

20. Acciavatti RJ, Maidment ADA. A comparative analysis of OTF, NPS, and DQE in energy integrating and photon counting digital x-ray detectors. *Med Phys*. 2010;37:6480–6495.
21. Nishikawa RM, Yaffe MJ. Model of the spatial-frequency-dependent detective quantum efficiency of phosphor screens. *Med Phys*. 1990;17:894–904.
22. Swank RK. Absorption and noise in x-ray phosphors. *J Appl Phys*. 1973;44:4199–4203.
23. Barrett HH, Myers KJ. Chapter 3: fourier analysis. In: Saleh BEA, ed. *Foundations of Image Science*. New York, NY: John Wiley & Sons; 2004:95–174.
24. Acciavatti RJ, Maidment ADA. An analytical model of NPS and DQE comparing photon counting and energy integrating detectors. In: Samei E, Pelc NJ, eds. *Physics of Medical Imaging*. San Diego, CA: SPIE; 2010:76220I-1–76220I-12.
25. Acciavatti RJ, Maidment ADA. Calculation of OTF, NPS, and DQE for oblique x-ray incidence on turbid granular phosphors. *Lect Notes Comput Sci*. 2010;6136:436–443.
26. Acciavatti RJ, Maidment ADA. Optimization of phosphor-based detector design for oblique x-ray incidence in digital breast tomosynthesis. *Med Phys*. 2011;38:6188–6202.
27. Zhao B, Zhao W. Three-dimensional linear system analysis for breast tomosynthesis. *Med Phys*. 2008;35:5219–5232.
28. Zhao B, Zhou J, Hu Y-H, Mertelmeier T, Ludwig J, Zhao W. Experimental validation of a three-dimensional linear system model for breast tomosynthesis. *Med Phys*. 2009;36:240–251.
29. Barrett HH, Myers KJ. Chapter 12: noise in detectors. In: Saleh BEA, ed. *Foundations of Image Science*. New York, NY: John Wiley & Sons; 2004:701–800.

W81XWH-18-1-0082 (BC170226): Design of a 3D Mammography System in the Age of Personalized Medicine

PI: Raymond J. Acciavatti, University of Pennsylvania

Budget: $603,749.00 **Topic Area:** Breast Cancer Research Program **Mechanism:** Breakthrough Award-Level 1

Research Area: X-Ray Imaging (708) Digital Imaging (704) **Award Status: Open** March 15, 2018 to March 14, 2021

Study Goals:

Even with the latest "3D" digital breast tomosynthesis systems, most women that are recalled for follow-up testing after a suspicious mammogram are ultimately found to be cancer-free. To improve the sensitivity and specificity of breast imaging for cancer detection, we are proposing to re-design mammography systems around the principle of "personalized medicine", so that the orbits of the detector and x-ray tube are customized to the size, shape, and composition of each breast. The new designs for both screening and diagnostic mammography will be validated with a virtual clinical trial using realistic simulations of breast anatomy and a highly-validated observer model.

Specific Aims:

SA1. Design a personalized image acquisition technique for screening mammography.
SA2. Design a 3D magnification mammography call-back exam.
SA3. Evaluate the new designs for screening and call-back imaging with a virtual clinical trial.

Key Accomplishments:

Publications:

1. Acciavatti RJ, Barufaldi B, Vent TL, Wileyto EP, Maidment ADA. Personalization of x-ray tube motion in digital breast tomosynthesis using virtual Defrise phantoms. In: Schmidt TG, Chen G-H, Bosmans H, editors; Physics of Medical Imaging; 2019; San Diego, CA: SPIE; 2019. p. 109480B-1 – 109480B-9. The PI (Raymond J. Acciavatti, Ph.D.) presented this work at the SPIE Medical Imaging conference on 2/17/19 in San Diego, CA. This work includes an acknowledgement of funding support from DoD grant W81XWH-18-1-0082.
2. Acciavatti RJ, Maidment ADA. Non-stationary model of oblique x-ray incidence in amorphous selenium detectors: I. Point spread function. Medical Physics. 2019; 46(2):494-504. This publication includes an acknowledgement of funding support from DoD grant W81XWH-18-1-0082.
3. Acciavatti RJ, Maidment ADA. Nonstationary model of oblique x-ray incidence in amorphous selenium detectors: II. Transfer Functions. Medical Physics. 2019; 46(2); 505-16. This publication includes an acknowledgement of funding support from DoD grant W81XWH-18-1-0082.

Patents: None as of the end of Year 1 of this grant.

Funding Obtained: The PI (Raymond J. Acciavatti, Ph.D.) was accepted as a mentor for the summer undergraduate fellowship program through the American Association of Physicists in Medicine (AAPM). Stipend funding will be provided directly to the undergraduate student. It is projected that the student will expand upon research involving virtual clinical trials. The student will perform this research at the University of Pennsylvania in the summer of 2019.